JEOL NEWS

P (No. of CuO$_2$ plane)

La: ● ● Cu: ● ● O: ● ●

5 Å

Out of plane

Contents

JEOL NEWS

Cover micrograph

Superimposition of simultaneously acquired high-resolution HAADF- and ABF-STEM images from a periodic 2D Sr-doped multilayer structure showing all atomic columns. The inset (yellow rectangle) shows the simulated STEM image (see Fig. 7 in page 15).

Fast Pixelated Detectors: A New Era for STEM

Peter D Nellist and Gerardo T Martinez   Department of Materials, University of Oxford

Conventional detectors for the scanning transmission electron microscope (STEM), such as the annular dark-field or annular bright-field detectors, integrate the intensity in the detector plane of the STEM over a range of scattering angles. In doing so, they neglect the rich information present in the intensity variations in the detector plane. Here we demonstrate that a recently developed fast pixelated detector, the JEOL 4DCanvas™ system, now allows the routine recording of the full four-dimensional STEM imaging data set. The four dimensions consist of the two real-space coordinates corresponding to the illuminating probe position, and the two reciprocal-space coordinates corresponding to position in the detector plane. Because the STEM probe pixel dwell time is now limited by the frame speed of the camera, one of the key developments is high frame rates of greater than 1000 frames per second. A second key development is direct electron detection with single electron sensitivity. We show that the 4D data set can be used to synthesize a range of STEM imaging modes from a single scan. We go on to use ptychography to retrieve the phase shift of the transmitted beam, showing how efficient phase imaging can now be achieved in STEM. It is shown that aberration correction is possible post-acquisition, and we explore the effects of dynamical scattering from heavier samples.

Introduction

Over the past two decades, the scanning transmission electron microscope (STEM) has become the instrument of choice for atomic resolution imaging and spectroscopy studies of materials, especially where quantitative information is required. There are two main reasons for this: (i) STEM allows for simultaneous imaging and spectroscopy revealing structure, composition and bonding at atomic resolution. (ii) The commonly-used imaging STEM modes are incoherent which leads to easier interpretation of the data [1]. The most commonly-used imaging mode makes use of an annular dark-field (ADF) detector to detect the intensity of the scattering to relatively high angles. The resulting ADF images show both an incoherent nature and compositional sensitivity and are therefore are a very powerful way of imaging materials [2]. In ADF STEM imaging, the total intensity incident upon the entire ADF detector is summed to give a value for the image pixel corresponding to the probe position. Any detail or variation of intensity in the STEM detector plane within the collection area of the detector is therefore lost. In this paper we explore how such intensity variations can be used in STEM, in particular through the use of ptychography to provide phase imaging.

Before the widespread availability of high-resolution STEM instruments, atomic resolution imaging was performed using phase contrast imaging in a conventional TEM (CTEM), a technique which became referred to as high-resolution TEM (HRTEM) [3]. In such images, dynamical scattering of electrons in the sample and changes in the precise imaging parameters can strongly affect the image, including leading to contrast reversals where it is not immediately clear whether the atoms or atomic columns appear as dark or bright contrast (see for example [4]).

In contrast, the incoherent nature of ADF STEM always leads to bright peaks for atoms or atomic columns.

Samples, such as graphene, that are thin and contain light elements are much more efficiently imaged in HRTEM compared to ADF STEM because the electron scattering from such samples can be regarded as only producing a small phase shift in the transmitted electron wave. It can be shown that weak phase objects produce very little signal in ADF STEM [5], whereas in the CTEM aberrations can be used to form a virtual phase plate that allow weak phase contrast imaging. The importance of phase contrast imaging in the CTEM has been highlighted in the biological imaging field by the award of the 2017 Nobel Prize in Chemistry for the development of cryo-EM. The imaging used for single particle analysis in biological imaging is phase contrast imaging, and indeed this has been the driver for the development of phase plates to enhance the phase contrast [6].

By the principle of reciprocity [7, 8], the configuration of the STEM detector plays the same role as the illumination configuration in a CTEM. As shown in **Fig. 1**, a small, axial bright-field (BF) detector in STEM is equivalent to highly parallel, axial illumination in the CTEM. A larger STEM detector is equivalent to a more highly convergent incoherent beam in the CTEM. The ADF detector in STEM is somewhat similar to hollow-cone illumination in CTEM. For HRTEM phase contrast imaging, a highly parallel, high-coherence beam is required, which is equivalent to the small axial STEM detector. It is now clear why the CTEM is more efficient than the STEM for HRTEM work: in the CTEM, a parallel beam illuminates the sample, and the scattering up to some angle corresponding to the numerical aperture of the lens is collected and imaged with the majority of the scattered electrons being detected. In the STEM,

〉〉 16 Parks Road, Oxford, OX1 3PH, UK | Email: peter.nellist@materials.ox.ac.uk

a highly convergent beam illuminates the sample but only electrons transmitted to a small axial detector are collected, so only a small minority of the transmitted electrons are detected. For radiation-sensitive materials where the efficiency of the imaging process is crucial, BF STEM imaging is not optimal.

In this paper we consider a fast pixelated detector (FPD) that records a two-dimensional intensity map of the STEM detector plane for each probe position in a two-dimensional scan, resulting in a four-dimensional (4D) data-set that can be regarded as the universal STEM imaging data set. We show that the 4D data set allows quantitative phase imaging, and because all the transmitted electrons are detected is very electron-efficient allowing relatively low-dose imaging.

Experimental Details

When recording the 4D STEM data set, the probe pixel dwell time in the scan is limited by the frame-speed of the detector. Typical STEM dwell times are less than 100 µs, and so detectors with extremely high frame rates are required. The detector should also offer single electron sensitivity with a high detector quantum efficiency. The work presented here was all recorded using a JEOL 4DCanvas™ system [9] mounted on a JEOL JEM-ARM200F cold field emission STEM system fitted with a probe optics aberration corrector. The 4DCanvas™ is a highly sensitive multi-channel STEM detector with channels of dimension 264 × 264. It can be read out at a speed of 1,000 frames per second (fps), or commensurately faster with binning (for example 4 by 1 binning gives 4,000 fps). The sensor of this pixelated detector is a direct electron detection charge coupled device. The Oxford system is shown in **Fig. 2**.

Results

Synthesis of conventional STEM images

We start by considering the imaging of the edge of a sample of Pt prepared by focused ion-beam lift-out and oriented along the <110> direction. A 4D data set was recorded at a beam energy of 200 keV from a 512 by 512 probe scan area with the detector operating without binning at 1,000 fps. **Figure 3**a shows a single detector image frame. The single electron detection is clear in the image. Summing over all probe positions to give a position-averaged convergent beam electron diffraction pattern (PACBED) (Figures 3b and 3c) shows the usual form of a convergent beam electron diffraction pattern.
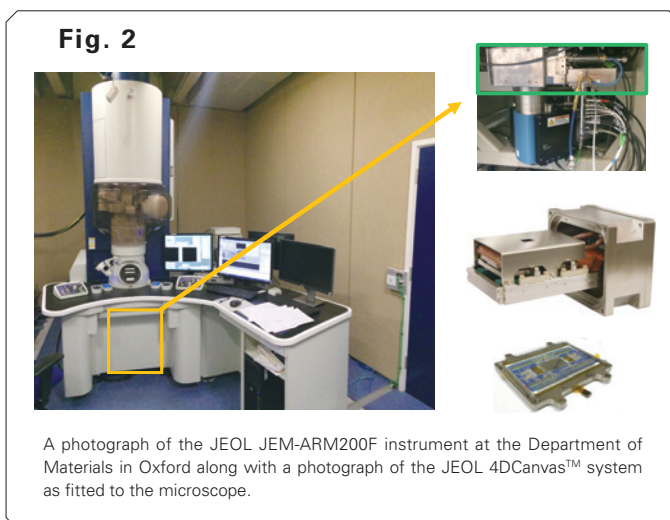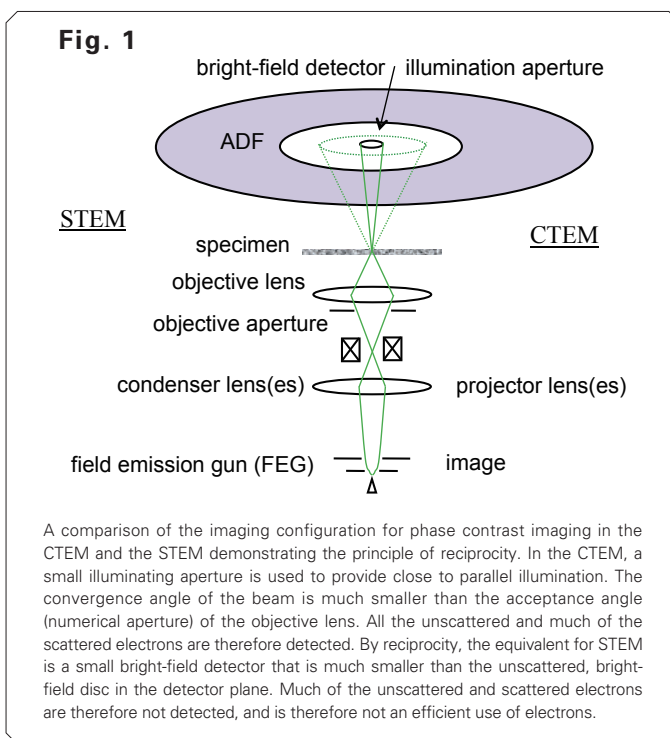
From this data set, images from a range of different STEM detectors can be synthesized. This is achieved by integrating the 4D data set over the desired detector geometry in the detector plane of the data, resulting in a 2D image. **Figure 4** shows the images from the incoherent bright field (IBF), annular bright-field (ABF), annular dark-field (ADF) and low-angle annular dark-field (LAADF) geometries with their integration regions displayed using the PACBED intensities. In particular it can be seen how the LAADF image shows a "halo" type contrast. This can be explained by considering that the LAADF intensity will maximize when the BF disc is at its maximum deflection, which will occur when the probe is slightly displaced from the centre of an atomic column and the illuminating electrons are experiencing the maximum net electric field, similar to the effect seen for differential phase contrast imaging [10] and similar to the effect seen for first-moment imaging [11].

Phase imaging through ptychography

In addition to allowing a flexible choice of imaging detector geometries that can be selected post-acquisition, the 4D data set creates a range of opportunities for new imaging modes that are only just starting to be explored. One such new mode is phase imaging through electron ptychography. Ptychography was proposed by Hoppe [12] as a method to solve the phase problem in electron diffraction, and was demonstrated experimentally in the early 1990s in the context of focused-probe STEM by Rodenburg and co-workers [13, 14]. At that time, camera and computing technical capabilities severely limited the technique, and images with typically only 32 by 32 pixels were achieved. The development of FPDs has enabled ptychography to become a viable and powerful technique in STEM. The 4DCanvas™ system installed on a JEM-ARM200F STEM at Oxford was the instrumentation on which ptychography was first used to solve the previously unknown structure of a recently synthesized material [15].

As described in [15], ptychography makes use of overlapping discs in a coherent convergent beam electron diffraction pattern. In the STEM configuration, the sample is illuminated by a highly convergent beam that is focused to form the probe. For a crystalline sample, the diffracted beams will form discs in the

Fig. 1

A comparison of the imaging configuration for phase contrast imaging in the CTEM and the STEM demonstrating the principle of reciprocity. In the CTEM, a small illuminating aperture is used to provide close to parallel illumination. The convergence angle of the beam is much smaller than the acceptance angle (numerical aperture) of the objective lens. All the unscattered and much of the scattered electrons are therefore detected. By reciprocity, the equivalent for STEM is a small bright-field detector that is much smaller than the unscattered, bright-field disc in the detector plane. Much of the unscattered and scattered electrons are therefore not detected, and is therefore not an efficient use of electrons.

Fig. 2

A photograph of the JEOL JEM-ARM200F instrument at the Department of Materials in Oxford along with a photograph of the JEOL 4DCanvas™ system as fitted to the microscope.

STEM detector plane, and in the overlap between these discs, coherent interference will occur. The resulting intensity will depend on the phase of the diffracted beams, any aberrations in the probe-forming optics, and the probe position. As the probe is scanned, the intensity in the disc overlap regions will fluctuate. Indeed, it is this fluctuation that is the origin of lattice contrast in any STEM image. Assuming the aberrations are corrected to zero, the phase of this fluctuation with respect to probe position is the phase difference between the interfering diffracted beams. From this information, the phases of all the beams can be determined. Once the phase problem is solved, it no longer makes sense to describe a method as being imaging or diffraction since the data can be readily converted from one to the other through a Fourier transform. Ptychography is thus a combination of diffraction and imaging.

It should be noted that the ptychography method implemented here for focused-probe STEM is not limited to perfect crystals, but is general to any object as long as the transmission by the sample can be modelled as a multiplicative transmission function. The mathematical approach used is described in more detail in [16] and modified for the current work as described in [15], but for completeness we describe it briefly here. The 4D measured data set is denoted $\left|M\left(K_f, R_0\right)\right|^2$ where the position in the detector plane is given by the reciprocal space vector K_f and

the illuminating probe position by R_0. Taking the Fourier transform of the data set with respect to the R_0 coordinate, but not the K_f coordinate gives

$$G\left(K_f, Q_p\right) = A\left(K_f\right)A^*\left(K_f + Q_p\right) \otimes_{K_f} \Psi\left(K_f\right)\Psi^*\left(K_f - Q_p\right)$$

where Q_p is the image spatial frequency variable conjugate to R_0, $A(K)$ is the aperture function for the illumination with a modulus controlled by the size and position of the objective aperture and phase reflecting any aberrations present, $\Psi(K)$ is the Fourier transform of the specimen transmission function, and $\otimes_{K_f}$ denotes a convolution with respect to the detector plane position variable. If $A(K)$ is known, then the product to the left of the convolution can be deconvolved, and the specimen transmission function determined from the product on the right. Thus the amplitude and phase of the specimen transmission function are determined, and both can be plotted fully quantitatively. Given the discussion in the introduction, it is important to note that the phase can be determined quantitatively even if there are no aberrations present. Efficient quantitative phase imaging is possible without the need for a phase plate using STEM ptychography. **Figure 5** shows a comparison of images from the same sample taken using a JEOL JEM-3000F instrument running as an HRTEM and a ptychography image from a STEM

Fig. 3
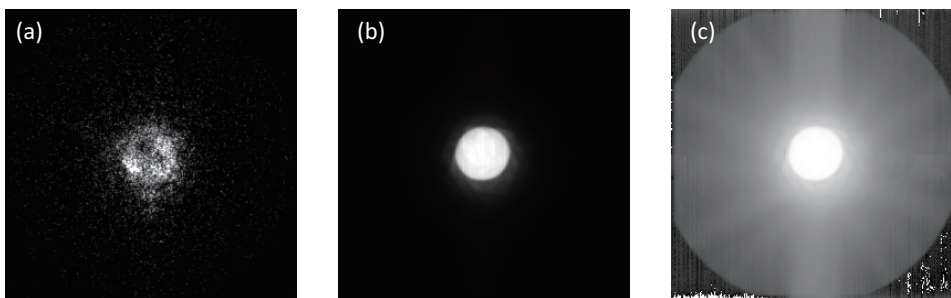
Data recorded from the 4DCanvas™ system during a 512 by 512 probe position scan over a sample of Pt <110> with the camera operating in full-frame mode at 1,000 fps. (a) A single frame where the bright points of intensity represent single electrons being detected. (b) The sum of diffraction patterns from the entire scanned area to form a position averaged CBED (PACBED) pattern. (c) The logarithm of the intensity of the PACBED pattern so that the Kikuchi lines are visible. The shadow of the JEOL ADF1 detector is also visible.

Fig. 4
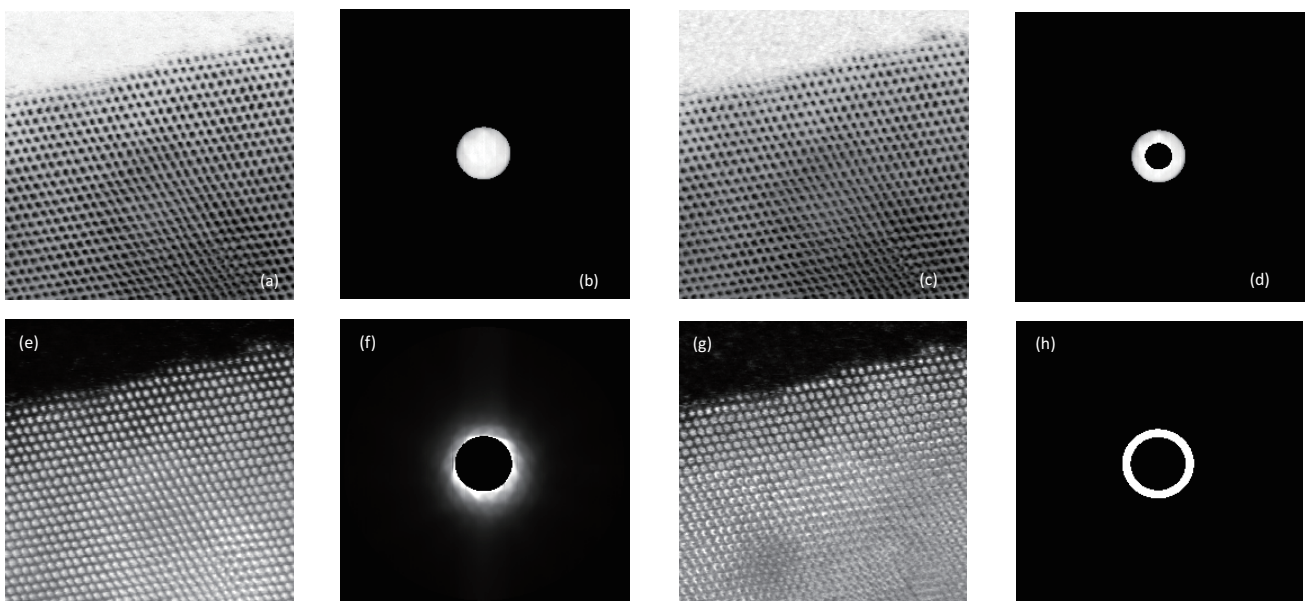
Synthesised STEM images from the data recorded in Fig. 3. (a), (c), (e) and (g) show images for IBF, ABF, ADF and LAADF respectively, with the integration regions over the detector illustrated in (b)(d)(f)(h) respectively.

showing that HRTEM-like imaging is now fully available in STEM.

Enabling low-dose imaging

Because all the transmitted electrons are detected when using an FPD, we might expect to form images with much lower noise that was possible with non-segmented detectors, and thus to be able to lower the electron dose while still maintaining sufficient signal to noise in the image. Equation (1) also allows us to know exactly where in the detector plane the information is arising for each spatial frequency in the image, and therefore by just using those regions, the noise (which is distributed across the entire detector plane) is somewhat rejected. It is like having a STEM detector that is adapting itself to be optimal for each different spatial frequency in the image. **Figure 6** shows a comparison of imaging using ADF and ptychographic STEM recorded simultaneously of a monolayer of hexagonal boron nitride. In the ptychographic image the noise is very low, and the location of a boron vacancy can be readily identified.

Aberration correction

Prior to the development of hardware to correct for the aberrations in the electron microscope, it was envisaged that ptychography would offer a solution to the problem of spherical aberration. Once the complex transmission function is known, the effects of aberrations can be deconvolved. This aim for ptychography was overtaken by the successful development of aberration correctors. Nonetheless, it remains the case that often, perhaps because of small aberration drift or imperfect corrector tuning, some residual aberrations remain. The more recently developed iterative methods for ptychography make no initial assumptions about the aperture which is then solved during the iterative process [17]. The direct method used for the results here, does require the aperture function to be known, but it has also been shown that in the case of a weak-phase object the residual aberrations can be directly measured from the function given in Equation (1), and then can be deconvolved [15]. **Figure 7** shows that even for a substantially misaligned instrument the aberration correction offered by ptychography is able to recover an image correctly reflecting the structure of the sample.

An additional benefit arising from the ability to correct aberrations is that a reconstruction can be performed assuming a specific defocus. It has been shown that this approach allows for an optical sectioning effect leading to three-dimensional reconstructions of the object [15]. The 3D information is inherently stored in the 4D data set recorded from the microscope even though the data has been recorded from a single scan at a fixed defocus.

Fig. 5
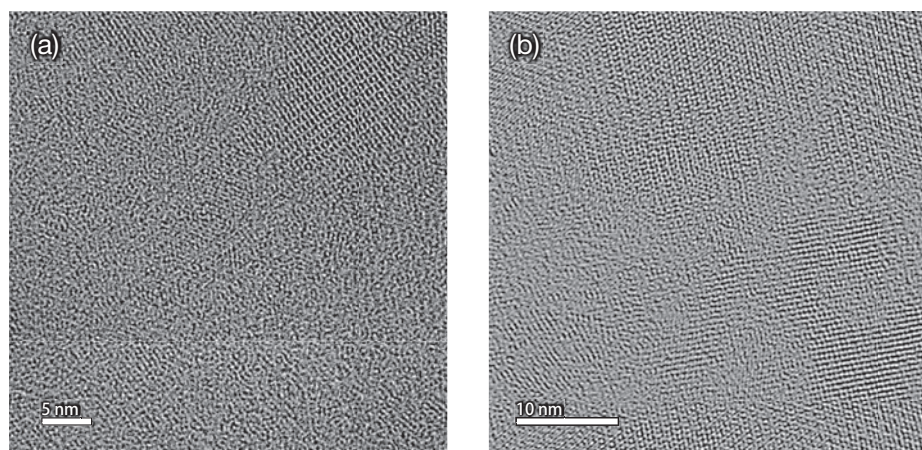
Images of a thin film of a C_{60}/C_{70} mixture: (a) recorded in a JEOL JEM-3000F instrument running in a CTEM configuration at 300 kV accelerating voltage; (b) recorded in a JEOL JEM-ARM200F instrument running at 200 kV using the 4DCanvas™ detector followed by ptychographic reconstruction. Note the similarity in the contrast revealed using the two types of imaging.

Fig. 6
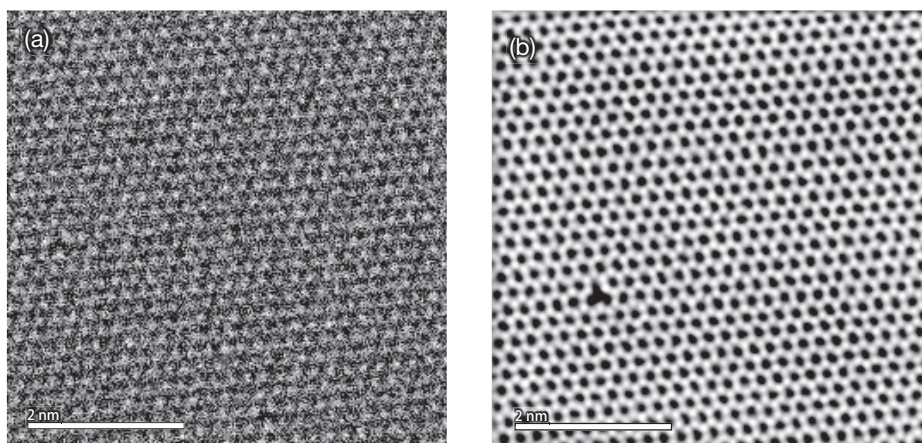
An ADF image and a ptychographic image of hexagonal boron nitride recorded simultaneously at a beam energy of 60 keV. The ptychography image can be seen to be much lower in noise, and a boron vacancy defect can be readily identified.

Dynamical effects

The theoretical basis for ptychography described above assumes that the interaction of the electron beam with the sample can be described by a multiplicative transmission function. For thicker and heavier samples, dynamical electron scattering conditions apply, and in this case the multiplicative approximation cannot be made. In the multiplicative approximation, it is assumed that the amplitude or phase of a diffraction beam is not dependent on the angle of the incoming beam with respect to the sample. In the case of dynamical scattering, there is a dependence.

Nonetheless, there is nothing to stop the 4D data set being recorded, and we can apply the same ptychographic reconstruction method to the data. Returning to the Pt wedge sample used in the data for Fig. 4, we can now perform a ptychographic reconstruction, as shown in **Fig. 8**. The peaks in the phase image can still be seen to be localized to the atomic column positions and there are no contrast reversals visible. At some thicknesses, the peaks show a "halo"-like structure. Similar results have been shown by Yang et al. [18]. Although a more detailed study is required, it appears that the ptychographically reconstructed phase images are more robust to dynamical effects and thickness changes than HRTEM images.

Conclusion

The development of FPDs for STEM has allowed for highly flexible imaging in STEM and has created opportunities for new imaging modes. Here we have explored applications of electron ptychography, and shown how focused probe electron ptychography can be performed alongside conventional STEM modes such as ADF. The resulting phase image bears many similarities to HRTEM, but is also seen to have a very high signal-to-noise ratio and is robust to dynamical effects. Ptychography also allows for the correction of residual aberrations which further improves image contrast and allows for optical sectioning for 3D imaging.

Although STEM has become the preeminent instrument for atomic resolution studies, HRTEM has remained popular for light and thin samples, such as graphene and other layered materials, and of course is the main mode for cryo-EM of biological structures. Given that it has now been demonstrated that ptychography in STEM can deliver low-noise phase images, alongside all the other benefits of STEM, it may be that we are on the cusp of a paradigm shift where STEM becomes regarded as a powerful phase imaging instrument. The development of FPDs for STEM now allow fields of view comparable with

Fig. 7
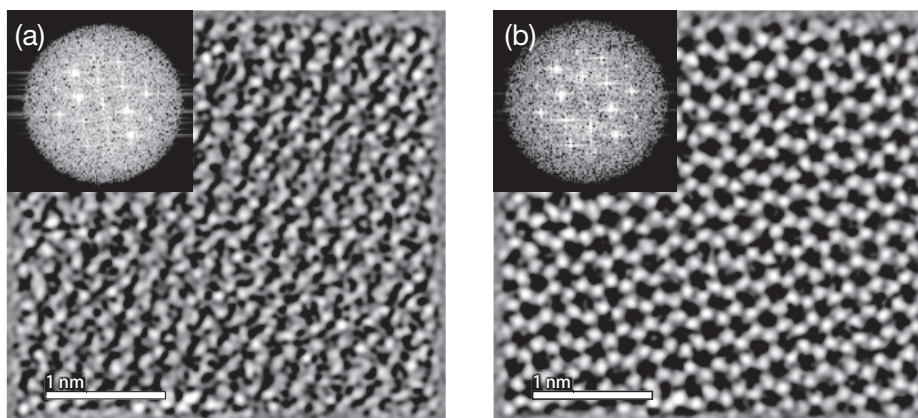
(a) An image of graphene recorded at 80 kV with the microscope misaligned leading to large residual aberrations. (b) From the ptychographic data set, the aberrations have been measured and corrected so that the lattice is now visible. The Fourier transform of the images show that the second ring of spots are all now visible, unlike the Fourier transform of image (a).

Fig. 8
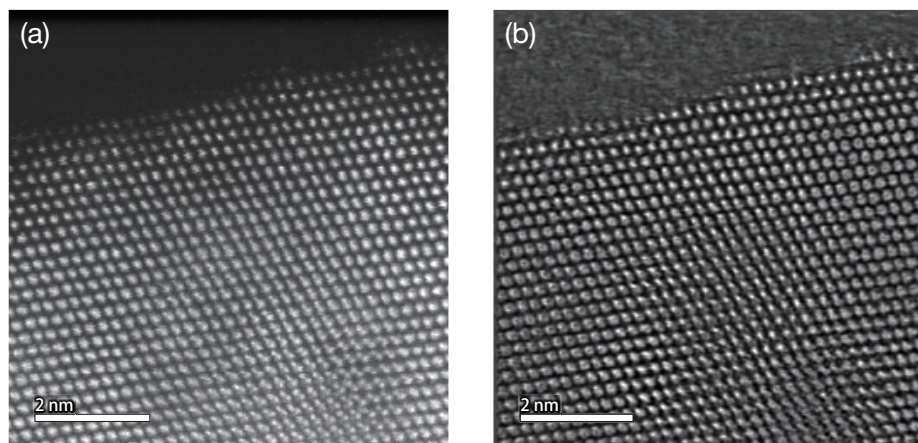
The ADF image (a) and the ptychographic phase image (b) from the Pt wedge sample also used in Fig. 4. As the thickness increases, the phase image starts to form "halo" like contrast, but the peak is still located at the atomic column position and contrast reversals are not seen. Note that there is an inclined stacking fault towards the lower right of the image so additional atomic columns are visible.

HRTEM, and **Figure 9** shows a 1k by 1k scanned image.

Finally, we note that ptychography is just one new mode possible with an FPD detector. Other authors have explored possibilities associated with measuring the angular dependence of the scattering at higher angles. Methods such as transmission Kikuchi diffraction become available, and using lower convergence angles the strength of all available diffraction spots can be measured as a function of probe position to give multiple diffraction contrast images in parallel, giving much greater information for dislocation burgers vector determination through g.b analysis for example.


Acknowledgments

References

[1] P. D. Nellist, Scanning Transmission Electron Microscopy, in: *Science of Microscopy* P.W. Hawkes, J. C. H. Spence (Eds.), Springer, 2007, pp. 65-132.

[2] P. D. Nellist, S. J. Pennycook, The Principles and Interpretation of Annular Dark-Field Z-Contrast Imaging, Advances in Imaging and Electron Physics, **113** (2000) 148-203.

[3] D. J. Smith, The realisation of atomic resolution with the electron microscope, Reports of Progress in Physics, **60** (1997) 1513-1580.

[4] R. W. Glaisher, A. E. C. Spargo, D. J. Smith, A Systematic Analysis of HREM Imaging of Elemental Semiconductors, *Ultramicroscopy*, **27** (1989) 35-52.

[5] T. J. Pennycook, A. R. Lupini, H. Yang, M. F. Murfitt, L. Jones, P. D. Nellist, Efficient phase contrast imaging in STEM using a pixelated detector. Part 1: Experimental demonstration at atomic resolution, *Ultramicroscopy*, **151** (2015) 160-167.

[6] M. Marko, A. Leith, C. Hsieh, R. Danev, Retrofit implementation of Zernike phase plate imaging for cryo-TEM, *Journal of Structural Biology*, **174** (2011) 400-412.

[7] J. M. Cowley, Image Contrast in a Transmission Scanning Electron Microscope, *Applied Physics Letters*, **15** (1969) 58-59.

[8] E. Zeitler, M. G. R. Thomson, Scanning Transmission Electron Microscopy, *Optik*, **31** (1970) 258-280 & 359-366.

[9] https://www.jeol.co.jp/en/news/detail/20170726.2143.html.

[10] N. Shibata, S. D. Findlay, Y. Kohno, H. Sawada, Y. Kondo, Y. Ikuhara, Differential phase-contrast microscopy at atomic resolution, *Nature Physics*, **8** (2012) 611-615.

[11] K. Müller, F. F. Krause, A. Béché, M. Schowalter, V. Galioit, S. Löffler, J. Verbeeck, J. Zweck, P. Schattschneider, A. Rosenauer, Atomic electric fields revealed by a quantum mechanical approach to electron picodiffraction, *Nature Communications*, **5** (2014) 5653.

[12] W. Hoppe, Beugung im Inhomogenen Primärstrahlwellenfeld. I. Prinzip einer Phasenmessung von Elektronenbeugungsinter ferenzen, *Acta Crystalographica* **A, 25** (1969) 495-501.

[13] J. M. Rodenburg, B. C. McCallum, P. D. Nellist, Experimental tests on double-resolution coherent imaging via STEM., *Ultramicroscopy*, **48** (1993) 303-314.

[14] P. D. Nellist, B. C. McCallum, J. M. Rodenburg, Resolution beyond the 'information limit' in transmission electron microscopy, *Nature*, **374** (1995) 630-632.

[15] H. Yang, R. N. Rutte, L. Jones, M. Simson, R. Sagawa, H. Ryll, M. Huth, T. J. Pennycook, M. L. H. Green, H. Soltau, Y. Kondo, B. G. Davis, P. D. Nellist, Simultaneous atomic-resolution electron ptychography and Z-contrast imaging of light and heavy elements in complex nanostructures, *Nature Communications*, **7** (2016) 12532.

[16] J. M. Rodenburg, R. H. T. Bates, The Theory of Super-Resolution Electron Microscopy via Wigner-Distribution Deconvolution, Philosophical Transactions of the Royal Society of London **A, 339** (1992) 521-553.

[17] A. M. Maiden, J. M. Rodenburg, An improved ptychographical phase retrieval algorithm for diffractive imaging, *Ultramicroscopy*, **109** (2009) 1256-1262.

[18] H. Yang, I. MacLaren, L. Jones, G. T. Martinez, M. Simson, M. Huth, H. Ryll, H. Soltau, R. Sagawa, Y. Kondo, C. Ophus, P. Ercius, L. Jin, A. Kovács and P. D. Nellist. Electron ptychographic phase imaging of light elements in crystalline materials using Wigner distribution deconvolution, *Ultramicroscopy* **180** (2017) 173-179.

Fig. 9
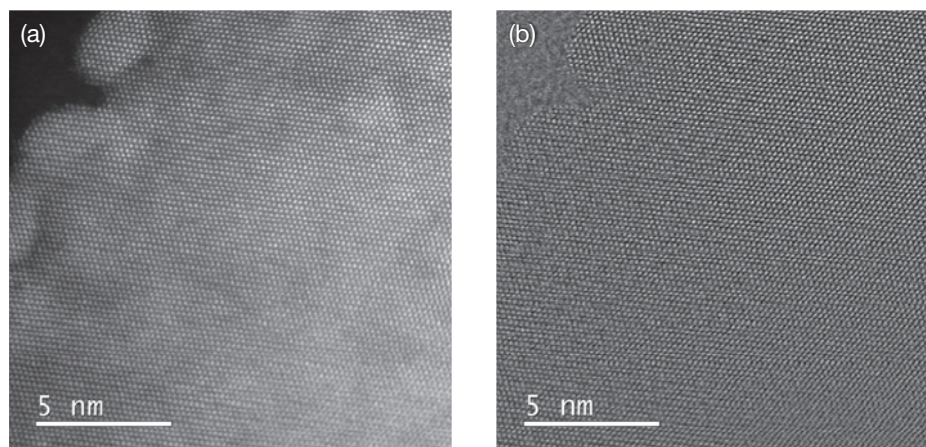
A simultaneously recorded (a) ADF and (b) ptychographic phase image from a Pt <110> wedge sample with 1 k by 1 k probe sampling recorded with a FPD frame speed of 4,000 frames per second demonstrating that large fields of view are possible in focused-probe STEM.

Aberration-Corrected Scanning Transmission Electron Microscopy of La$_2$CuO$_4$-based Superconducting Interfaces at the Stuttgart Center for Electron Microscopy

Y. Eren Suyolcu, Yi Wang, Federico Baiutti, Wilfried Sigle, Georg Cristiani, Giuliano Gregori, Gennady Logvenov, Joachim Maier, Peter A. van Aken

Stuttgart Center for Electron Microscopy, Max Planck Institute for Solid State Research

The discovery of novel phenomena occurring at interfaces in complex oxide heterostructures has stimulated large interest in recent years due to the prominent possibilities of tuning functionalities at the atomic layer scale. It is the complex interactions between atoms at the interfaces of epitaxial oxide systems which contribute to intriguing physical effects. This illustrates the predominant role played by the local structural parameters. Tuning the network of metal–oxygen octahedra is a promising route for achieving new properties and functionalities in perovskite-based oxide hetero-structures. Here we focus on high-temperature interfacial space-charge induced superconductivity which is one of the most exciting interface effects. We report on extensive investigations on the local chemistry and crystal structure including octahedral distortions across La$_2$CuO$_4$-based superconducting interfaces using high-resolution analytical scanning transmission electron microscopy (STEM) techniques.

Introduction

High-quality functional complex oxide heterostructures are excellent systems for studying interface phenomena arising from the interaction between neighboring layers [1,2]. Depending on the choice of the constituents, different microscopic phenomena can occur at the interfaces, including electronic and orbital reconstruction, magnetic exchange interactions, crystal-structure distortions, chemical intermixing or breaking of the crystal symmetry [3].

In this context, one recent exciting finding was the observation of high-temperature interface superconductivity (HT-IS) at the interface between epitaxially grown strontium-over-doped metallic (M) lanthanum cuprate (La$_{1.55}$Sr$_{0.45}$CuO$_4$) and under-doped insulating (I) La$_2$CuO$_4$ (LCO) layers [4], none of which is superconducting if taken alone. The full understanding of HT-IS is a very important step towards the disclosure of mechanisms for high-temperature superconductivity (HTSC) [4,5], being potentially able to shed light on questions related to the formation of superconducting interfaces [4], its dimensionality and locus [6], and the impact of the crystal structure and atom positions on the superconducting properties [7,8]. Numerous studies employing advanced experimental methods as well as innovative approaches have addressed these questions [6,7,9-13].

In order to explain the HT-IS in M–I lanthanum cuprate bilayers, a model based on the electronic charge transfer due to a difference in the hole chemical potentials between the over-doped and under-doped phases has been invoked [6,13]. As a consequence of such a redistribution, a doped region having the optimal hole concentration for HT-IS is formed in the nominally insulating phase (namely, the second CuO$_2$ plane in LCO away from the interface). In such bilayers, the superconducting critical temperature (T_c) was also found to be dependent on the deposition sequence (e.g. M-I or I-M), where the top layer adopts the out-of-plane lattice parameter of the bottom phase as a result from electrostatic interactions ("Madelung strain") and a linear relation between T_c and c was revealed [7]. Such findings open an exciting scenario for the enhancement of the superconducting critical temperature in M–I lanthanum cuprate heterostructures, which could in principle be obtained by appropriately tuning the out-of-plane lattice parameter of the bottom layer.

The development of spherical aberration (C_s) correctors [14] in (scanning) transmission electron microscopy ((S)

TEM) provides sub-Ångstrom spatial resolution. In STEM, the annular bright-field (ABF) imaging technique is capable of imaging light elements [15-17], such as oxygen, which makes ABF especially interesting for the investigation of perovskite oxides [18,19]. ABF images can be simultaneously recorded with high-angle annular dark-field (HAADF) images [20] and correlated with spectroscopic techniques such as electron energy-loss spectroscopy (EELS) and energy-dispersive X-ray (EDX) spectroscopy. Moreover, it is well-known that the properties of complex perovskite-type oxide structures (mostly ABO_3 and A_2BO_4 type structures and their derivatives) are strongly influenced by small structural changes of the BO_6 octahedral network [21,22]. Thus, the understanding how the octahedral distortions are correlated with the dopant distribution and how they modify the functionality of complex oxide heterostructures is of significance. Although octahedral distortions at interfaces of various heterostructures have recently been widely studied via ABF imaging [18,19,22-25], the present understanding of octahedral networks and their distortions in A_2BO_4 systems is still limited.

In this work, we demonstrate the indispensable role played by aberration-corrected STEM for the determination and interpretation of interfacial octahedral distortions in oxide heterostructures, in particular for La_2CuO_4-based superconducting interfaces. We have comprehensively studied $La_{1.6}A_{0.4}CuO_4$–La_2CuO_4 bilayers (with A = Ca, Sr, Ba) and two-dimensionally (2D) doped La_2CuO_4 superlattices (SLs), which were grown via the atomic-layer-by-layer oxide molecular beam epitaxy technique (ALL-oxide MBE) [26], by employing analytical high-resolution STEM techniques. Through atomically-resolved STEM-EELS investigations we demonstrate how the dopant size affects the dopant distribution, and thus the superconducting mechanism of the system. Moreover, by analyzing the cation and anion strain-induced displacements at picometer resolution, we demonstrate that the size mismatch between the dopant and the host La^{3+} cations has a direct influence on the structure and in particular on the out-of-plane strain state [27].

La₂CuO₄ bilayers: Probing dopant size effects on HT-IS

The bilayer structures were grown on $LaSrAlO_4$ (LSAO) (001) substrates, where the growth process starts with an over-doped metallic layer followed by an undoped insulating layer. A structural model of the ALL-oxide MBE grown bilayers is given in **Fig. 1**a. Figure 1b–d show atomically resolved HAADF images which cover the substrate and the nominal metallic and insulating layers demonstrating a high quality of the bilayers as well as perfect coherent interfaces and the absence of extended defects, such as misfit dislocations and/or stacking faults. Initial XRD measurements have revealed that the shortest c-axis lattice constant (13.22 Å) was observed for the LCCO/LCO bilayers, whereas the c-axis lattice parameters are 13.28 Å and 13.37 Å for the LSCO/LCO and LBCO/LCO bilayers, respectively. Such findings nicely correlate with the nominal cationic radii in nine-fold coordination [28], as a consequence of Madelung strain [7]. For the LCCO/LCO, LSCO/LCO and LBCO/LCO systems, the superconducting critical temperatures (T_c) are ~17 K, ~36 K and ~39 K, respectively [29].

In order to gain deeper insight into the interfacial structure and on the present c vs T_c relation in comparison with the literature, atomically resolved imaging and spectroscopy were carried out. **Figure 2**a, b present HAADF images of the LCCO/LCO bilayer. An atomically resolved image at a higher magnification of the highlighted region in Fig. 2a is presented in Fig. 2b. Figure 2c shows the intensity profile of the HAADF image taken from the Ca-doped bilayer presented in Fig. 2a. In the HAADF image, Ca-doped areas exhibit a darker contrast, due to Z-contrast ($Z_{La} = 57$ and $Z_{Ca} = 20$) [20,30], and the HAADF intensity increases in the first 1–2 unit cells (uc) indicating a Ca-depleted region in the LCCO layer. Figures 2d, 2f, and 2h show RGB (the colors red, green and blue represent Cu, La and the dopant, respectively) atomic resolution maps of Ca-, Sr- and Ba-doped bilayers as measured by EELS. The average profiles of the dopant distributions obtained from the EELS maps are shown below each RGB map in Figs 2e, 2g and 2i. The RGB maps and the average profiles of the dopant distributions for each bilayer exhibit characteristic differences. The Sr-doped bilayer shows the most homogeneous distribution among the dopants (Figs 2f and 2g). The abruptness of the LSCO/LCO interface can be estimated from the decay of the Sr distribution from the M layer into the I layer as 1.6 ± 0.4 nm, which is in fairly good agreement with the values for the interfacial width reported in the literature [4]. Conversely, the distribution of the Ca and Ba dopants in the LCCO/LCO and LBCO/LCO bilayers is less homogeneous. The atomically resolved EELS RGB map (Fig. 2h) and the averaged profile of the Ba dopant (Fig. 2i) indicate that the Ba concentration increases towards the nominal LBCO/LCO interface and obviously demonstrates the tendency of Ba to segregate towards the free surface of the film. Most importantly, as a consequence of such Ba migration, the LBCO/LCO interface is quite smeared and considerably wider than for the other dopants, i.e. the interfacial width for LBCO is 2.6 ± 0.6 nm. As far as the LCCO/LCO bilayer is concerned, we observe a tendency that Ca accumulates at the interface between the substrate and the epitaxial layer, followed by a depletion of Ca in the 1st and 2nd uc (Figs 2d and 2e). This behavior is most likely linked with the compressive in-plane strain state in the film. In this case, the extent of cationic intermixing at the M–I interface and the interfacial width is estimated to be ~1.4 ± 0.4 nm. For the determination of the distribution widths for each dopant, several line scans acquired from different regions of the samples are averaged to improve the statistics.

Our investigations highlight the profound influence of the dopant on the final structural properties of the bilayers, and accordingly on the electrical transport properties [29]. We observe a major impact of the dopant size on the in-plane strain state of the films, in a similar way as has already been demonstrated by Lee *et al*. for a related perovskite system [27]. In particular, when Ba^{2+} is the dopant, i.e. in the LBCO/LCO bilayers, a maximum in-plane strain is induced due to the large misfit. As the HAADF images show perfect epitaxial growth of all films without any defects which could relieve strain, the only way to obtain strain relaxation in the case of the Ba-doped system is by the rearrangement of dopants within the film, i.e. the segregation of excess Ba towards the film surface.

Remarkably, we observed a strong deviation from the expected linear dependence of T_c on the c-axis lattice parameter for the M–I bilayers, with T_c of the LBCO/LCO

Fig. 1
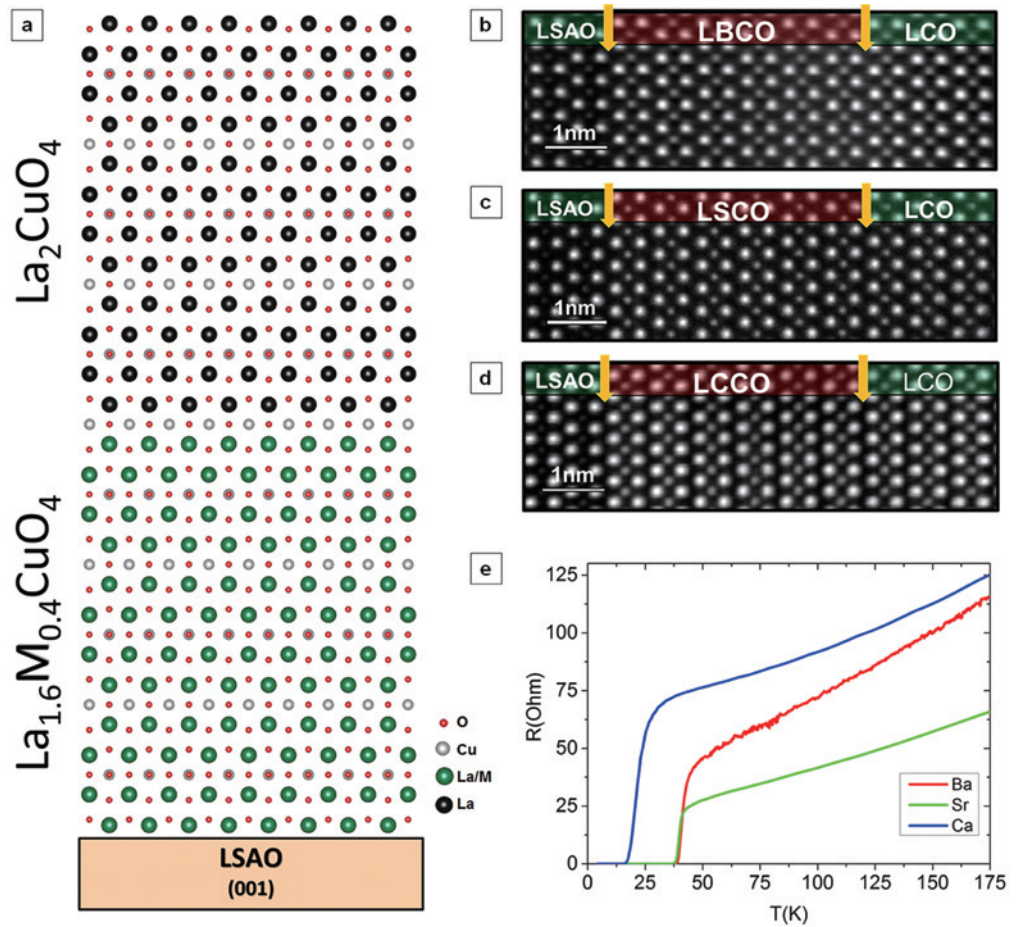
a) Structural model of the bilayers grown on the LSAO substrate and STEM–HAADF images showing coherent interfaces of b) Ba- (LBCO), c) Sr- (LSCO), and d) Ca- (LCCO) doped bilayers. The HAADF images were taken along the [100] direction of the LSAO substrate. e) Transport measurements as resistance versus temperature for differently doped bilayers. Figures reproduced with permission from Ref. [36].

Fig. 2
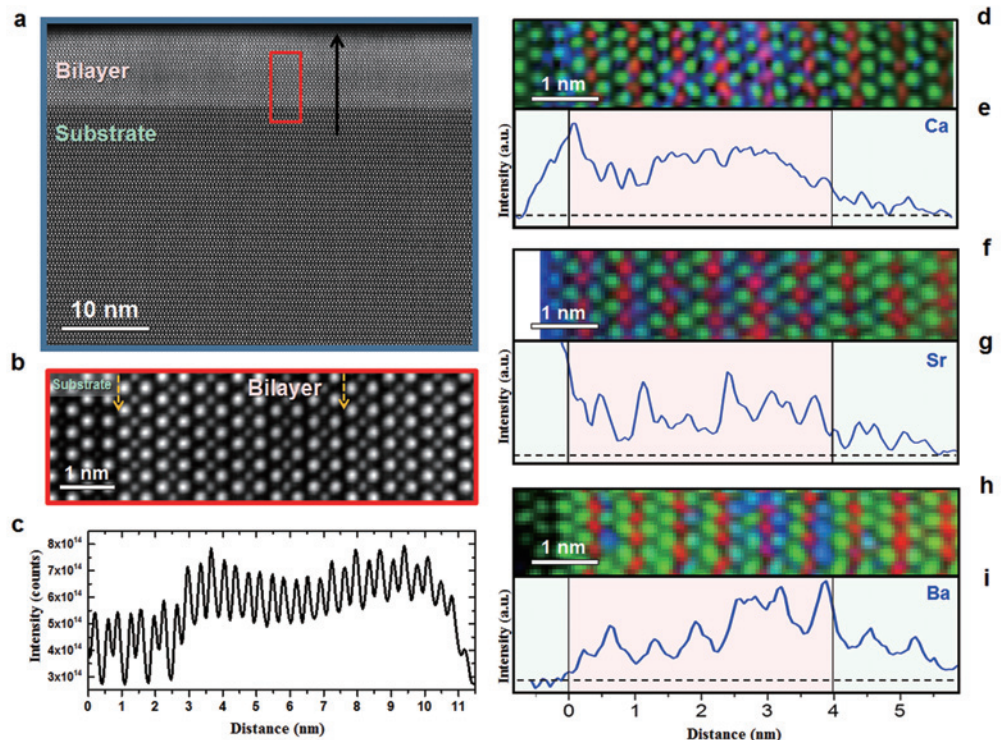
Atomic-column resolved STEM and EELS spectrum imaging. (a) HAADF image showing the growth quality, a defect-free structure and coherent interfaces of LCCO/LCO. (b) High magnification of the area highlighted by the red rectangle in (a). (c) Intensity profile along the black arrow in (a), averaged across the horizontal direction. In (d), (f), and (h), RGB elemental maps (La = green, Cu = red, dopant = blue) are shown. In (e), (g) and (i) the dopant distributions of the Ca-, Sr- and Ba-doped bilayers, as obtained from the maps in (d), (f) and (h), are displayed. Figures reproduced with permission from Ref. [29].

bilayer being lower than expected (over 60 K), while the c-axis lattice parameter is increased [29]. In order to explain this context, we need to consider the dopant distribution at each M–I interface. In particular, the average cationic intermixing extent is as high as 2 uc in the case of the LBCO/LCO bilayers. The anomalous Ba redistribution is a consequence of Ba segregation towards the film surface, which results in a particularly broadened M–I interface. This finding accounts for the reduced T_c of the LBCO/LCO bilayers as demonstrated for a related LCO-based system for which a spread interface leads to a classical doping model, the so-called "homogeneous doping" [31], in which the hole concentration is increased in correspondence to the randomly distributed ionic dopant point defects, rather than to an interface effect, defining the final local physical properties. In such a situation (only homogeneous doping is active), one expects T_c not to exceed the values which are obtained in doped bulk single-phase systems, i.e. the maximum $T_c \sim$ 40 K is obtained for optimally doped LBCO samples which are epitaxially grown on $LaSrAlO_4$ (001) substrates [32]. For both the LCCO/LCO and LSCO/LCO bilayers, despite a certain dopant redistribution is present at the interface; the superconducting and structural properties are consistent with HT-IS. Notably, for the LSCO/LCO interface as investigated by Gozar *et al*. [4], Sr is redistributed into the nominally undoped phase for a depth of about 1 uc, i.e. 1.3 nm, in agreement with our observations on both LCCO/LCO and LSCO/LCO structures.

Visualizing Jahn–Teller effects at interfaces

After having revealed the dopant distributions, we focus on the correlative impact on the structure of the octahedral network. The CuO_6 octahedron in the parent La_2CuO_4 phase is elongated along the *c*-axis by the Jahn–Teller (JT) effect [33] and exhibits two long and four short Cu–O bonds [34]. It is reported that, in such systems the incorporation of dopants determines the compression of the octahedron (i.e. a decrease of the Cu–O apical distances) [35] defined as an anti-Jahn–Teller (AJT) effect [33].

In this context, we simultaneously acquired HAADF (Fig. 1) and ABF images (**Fig. 3**) of the interfaces of all samples, thus imaging all atomic columns in the crystal structure, namely La/Sr–O, Cu–O, and O [36]. To quantitatively analyze and measure the local lattice distortions, we mapped all atomic positions from the images by first locating the center-of-mass and then iteratively refining a 2D Gaussian fitting procedure for each atomic column [37]. Figure 3a–c shows the unambiguously atomic-column resolved ABF images. In Fig. 3d, the measurement of the interatomic distances is defined. The red arrow shows the distance between apical oxygen atoms, the green arrow shows the distance between oxygen atoms in the basal plane.

By averaging the dopant intensity profiles from elemental $Ba-M_{4,5}$, $Sr-L_{2,3}$ and $Ca-L_{2,3}$ EELS analyses, integrating the intensities for each constituting block (i.e. half uc of the A_2BO_4 structure), summing up the values of all the constituting blocks along the growth direction, and scaling the doping concentration profiles in order to preserve the global stoichiometry, we have obtained the dopant concentrations (*x*) for each constituting block. **Figure 4** a–c summarizes the dopant concentrations and gives quantitative information about the composition of each block. It is known from the electronic phase diagram of the hole-doped lanthanum cuprate system, that the superconducting phase in

bulk systems occurs when the doping level of a La_2CuO_4 uc lies between $0.05 \leq x \leq 0.26$ [38]. At lower doping levels an insulating phase is present (under-doped), whereas a metallic (over-doped) phase appears at $x > 0.26$. The measured interatomic distances vs. the number of CuO_2 planes (or LCO blocks) are displayed in Fig. 4d–f. The basal and apical O–O interatomic distances are plotted in green and in red, respectively. Each data point corresponds to one measured LCO block. The O–O interatomic distances were calibrated according to the distances measured in the LSAO substrate.

All measurements of the basal in-plane O–O distances for the three different bilayers exhibit the same value (i.e. ~ 3.75 Å), showing a perfect coherency with the LSAO substrate. These findings demonstrate that all films are under compressive in-plane strain [30]. Conversely, in the LBCO/LCO system, a drastic decrease of the apical oxygen distances with increasing Ba concentration is observed (Fig. 4d). In the first LCO block of the epitaxial layer, the measured spacing is 4.72 ± 0.03 Å, whereas it is 4.51 ± 0.04 Å in the 6th LCO block. In the following column (the one next to the nominal LBCO/LCO interface) the O–O apical distance is assessed as 4.69 ± 0.030 Å. Considering the dopant concentrations from the EELS analyses (Figs 2e, f and 4a), it is evident that the blocks mostly exhibit metallic and superconducting phases. This indicates that, due to ionic intermixing, i.e. to ionic doping, superconductivity in the LBCO/LCO bilayer should not be ascribed to effects arising at the M–I interface; rather it is a bulk phenomenon involving several unit blocks [29]. Moreover, the correlation between the gradient in the Ba distribution and the apical O–O distances on both sides of the M–I interface (e.g. the decrease of the apical O–O distance with increasing Ba doping vice versa) could be ascribed to the AJT effect causing AJT distortions [33], which results in a localization of holes in both d_{x2-y2} and d_{z2} orbitals [39]. Consequently, although a larger *c*-lattice parameter is obtained via Ba doping in both bulk [32] and epitaxially grown heterostructures including single phase films, significant AJT distortions cause shorter Cu–O distances and prevent a T_c enhancement.

In the highly doped region of the LSCO/LCO bilayer, the O–O interatomic distances remain constant (Fig. 4e), while a marked increase by 15 pm from the 8th (4.55 ± 0.03 Å) to the 9th atomic row (4.70 ± 0.05 Å) is detected. Given the homogeneous Sr distribution in the over-doped layer, the AJT effect for the Sr-doped sample is negligibly small, as the O–O distance variations are almost as small as our measurement precision (~ 4 pm) [37]. However, we do observe a considerable increase of the O–O apical distance starting from the 9th block. Notably, such an "anomalous expansion" has been previously reported for similar systems [8,30], in which the relation with the occurrence of HT-IS as a consequence of interface effects (i.e. hole redistribution near the interface) was clearly demonstrated [6]. Therefore, the observed sharp increase of the apical O–O distance starting from the 9th block (JT distortion indicating localized holes in d_{x2-y2} orbitals) can be considered as a fingerprint for a superconducting transition induced by interface phenomena.

In the LCCO/LCO bilayer, large O–O distances were obtained for the first two uc, where the Ca concentration is less than the nominal doping level (Fig. 4f). The value measured for the 2nd epitaxial block was 4.68 ± 0.04 Å and the lowest values of around 4.56 Å are obtained for the 5th and 6th blocks representing a decrease of the O–O interatomic distance. For these samples, we face a combination of both

Fig. 3
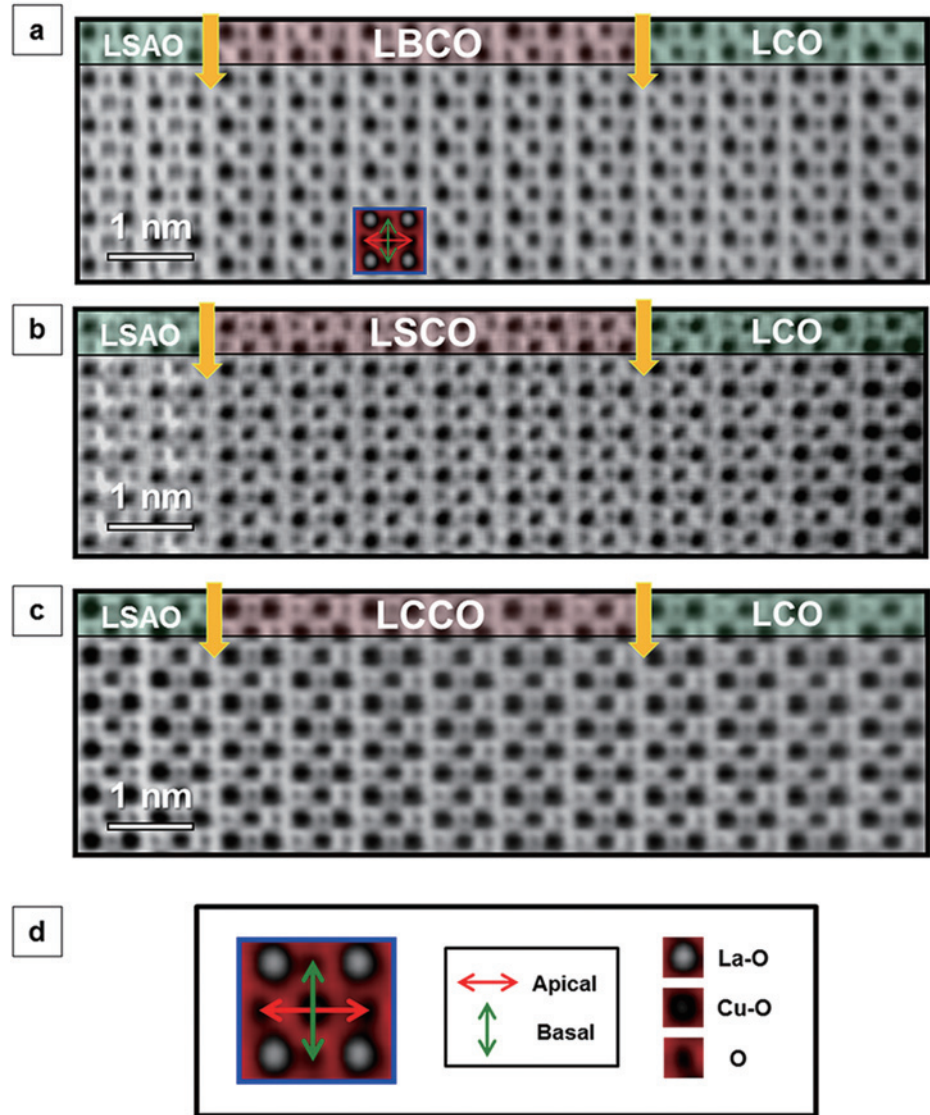
The ABF images show coherent interfaces and all atomic column positions including the O positions for the (a) Ba-, (b) Sr-, and (c) Ca-doped bilayers. The yellow arrows indicate the nominal interface positions. (d) Illustration of the measurement of the apical and basal O-O distances on a magnified (and colored) section obtained from panel (a). Figures reproduced with permission from Ref. [36].

Fig. 4
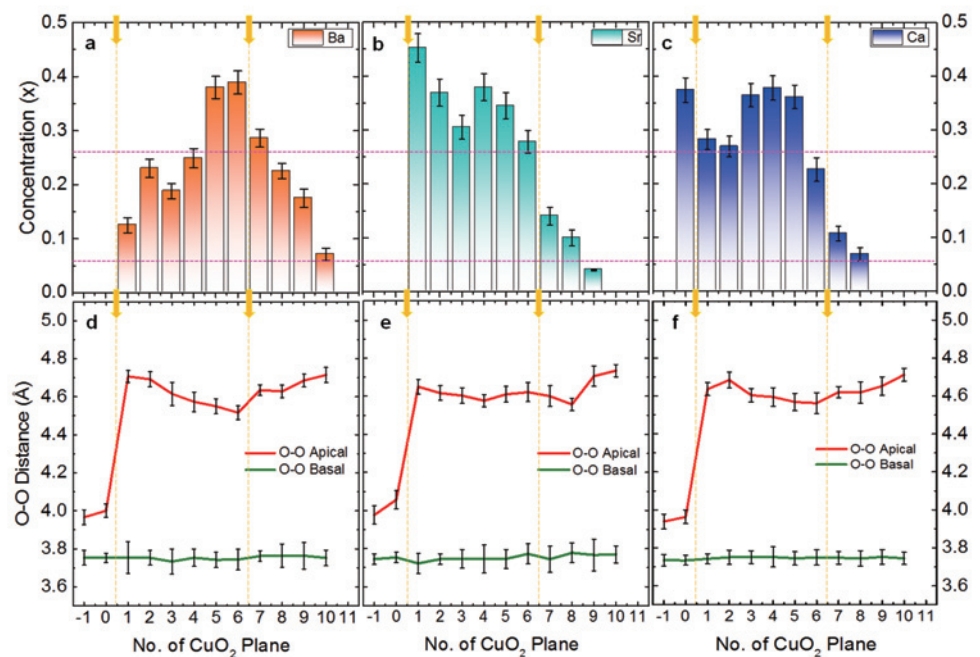
Dopant concentration per CuO$_2$ block for the (a) Ba-, (b) Sr-, and (c) Ca-doped bilayers. The horizontal dashed lines delimitate the region corresponding to the superconducting phase. (d–f) The O-O atomic-column spacing along the apical (red) and basal (green) directions for the LBCO/LCO, LSCO/LCO, and LCCO/LCO bilayers, respectively. The yellow arrows and vertical lines indicate the nominal interface positions. The error bars represent the 95% confidence interval (corresponding to two times the standard error) of the average of 14 uc of LCO along the basal direction. Figures reproduced with permission from Ref. [36].

an AJT (in the metallic phase) and a JT (starting from the interface) distortion. In the Ca-depleted region (i.e. 1st and 2nd blocks), an increase (~ 10 pm) of the apical O–O distances is followed by a decrease starting from block 3, in which a higher dopant concentration is present. This again represents an AJT effect similar to the over-doped layer of the Ba-doped sample. Finally, a gradual increase starting from the 6th block is observed and the difference between 6th (4.56 ± 0.04 Å) and 10th (4.71 ± 0.03 Å) blocks is determined as 15 pm. Remarkably, blocks 9 and 10 do not exhibit the presence of any Ca-dopant, thus we observe here a typical JT distortion which, unlike what was observed for the M phase, cannot be ascribed to the presence of the dopant. Rather, given the superconducting character of the interface, such a JT distortion may be related to 2D interfacial superconductivity in a similar way as discussed for the Sr case.

Our investigations of lattice and octahedral deformations suggest that a JT distortion is present only in the case of Sr- and Ca-doped M–I bilayers. In the case of the Ba-doped bilayer, AJT distortions characterize both sides of the nominal interface of LBCO/LCO. Such a relation between the dopant concentrations and the out-of-plane O–O distances points towards two different superconducting mechanisms, activated by the different dopant distributions leading to different JT distortions. In particular for bulk superconductivity (Ba-doped case) we face a typical AJT distortion (holes located in d_{x2-y2} and d_{z2} orbitals with parallel spins, resulting in shorter O–O distances [40]), whereas for Sr- and Ca-doped bilayers we observe a combination of AJT and JT distortions (in which holes are located only in d_{x2-y2} orbitals and the apical oxygens are shifted away from the La sites resulting in larger O–O (apical) interatomic distances). This may be related to the presence of interface effects characterized by an electronic redistribution.

Two-dimensionally (2D) doped superlattices: Revealing space-charge effects

The possibility of tuning oxide functionalities by the insertion of an interface or active layers has been frequently investigated in recent years [2,3,41]. Tuning of physical properties via local interface effects at grain boundaries, at epitaxial contact between different phases [42,43], and via delta-doping [44,45] has been achieved. This has resulted in the improvement of electrical performance in ionic and mixed conductors and in the emergence of novel effects, ranging from high-temperature superconductivity [4] to electrical conductivity [46] and magnetism [47]. In this section, we present the utilization of unconventional heterogeneous doping [41,48], enhancing the hole concentration and thus triggering superconductivity [31]. Inspired by the so-called delta-doping technique [49,50], we replace single LaO planes with SrO ones with the aim of creating two-dimensional (2D) and atomically confined charged layers within the undoped La_2CuO_4 matrix by using ALL-oxide MBE.

Dopant – hole decoupling

The structural and chemical investigations performed via comprehensive STEM techniques at the interfaces are compiled in **Fig. 5**. The high-angle annular dark-field (HAADF) micrograph (Fig. 5a, e) demonstrates perfect epitaxy. In the intensity profile obtained from the HAADF image (averaged perpendicularly to the growth direction), the intensity drop is connected with the Sr-containing

layers, which involves more than a single atomic plane, indicating a certain Sr redistribution into the La_2CuO_4 matrix. Spectroscopic analyses (Figs 5c, d) reveal a pronouncedly asymmetric character of the Sr profile: Virtually abrupt at the side facing the substrate (downward side) with an extent of 0.9 ± 0.2 nm and redistributed over 2.3 ± 0.4 nm at the upward side. STEM-EELS (Fig. 5d) provides further robust evidence of the asymmetric Sr distribution, ensuring single atomic layer resolution (step size ≈ 2 Å) [51]. By averaging the different EELS Sr-$L_{2,3}$ intensity profiles from several Sr-containing atomic slabs, one can accurately define the Sr level (x) that can be assigned to each 'constituting block' (namely a single CuO_2 plane and the two surrounding (La, Sr)O layers) in proximity of the layer where Sr was initially inserted (Fig. 5f). Obviously, we have realized an abrupt profile, but only at the downward side, while at the other side (upward) there is a pronounced redistribution of the aliovalent cation.

In these 2D-doped La_2CuO_4 multilayers, by appropriately choosing the spacing between the dopant planes, the resulting electrical properties of such heterostructures exhibit HTSC up to ~35 K [31] and is a consequence of the local charge accumulation occurring on both sides of the doped planes as a consequence of different mechanisms of doping: (i) heterogeneous doping at the downward side and (ii) "classical" homogeneous doping at the upward side of the interface. Here "heterogeneous doping" means that hole accumulation occurs to compensate for the spatially confined ionic negative charge stemming from the SrO layer, i.e. a space-charge region is formed as a consequence of 2D doping. In this case, the electronic and dopant distributions are decoupled. "Homogeneous doping" refers to the local compensation of Sr (zero-dimensional) point defects by electron holes. This situation, which is triggered by the highly asymmetric Sr distribution resulting from the growth kinetics, is therefore characterized by the presence of two spatially separated doping modes [31]. (iii) In addition, as highlighted by complimentary Zn-tomography [6] at the downward side, HT-IS is confined in a single CuO_2 plane, namely the second plane far from the interface, while the very first layer is not superconducting [31]. This "overdoping" is most probably due to a high oxygen vacancy concentration, which has to steeply increase in the space-charge electric field created by the SrO layer, owing to a double charge.

Probing octahedral distortions

Now, we turn our attention to the hole distribution across the doped interfaces. The pre-edge feature of the O−K edge is very sensitive to the hole concentration [52,53], enabling the local determination of the hole concentration in the superconducting phase [54]. As shown in **Fig. 6**a, typical O-K edge spectra recorded in the Sr-doped region (red) and in the LCO region (black) can be readily distinguished: a pre-edge feature at around 528 eV (in yellow), which is attributed to transitions from the O 1s core level to hole states with p symmetry in the valence band [55], is clearly seen in the former. The black curve shows no detectable O-K edge prepeak. The intensity of the pre-edge peak has been quantified by multi-Gaussian peak fitting using a nonlinear least-squares (NLLS) routine for all spectra in the line-scan profile across several interfaces (Fig. 6a). To quantify the hole and Sr concentrations per building block of $La_{2-x}Sr_xO_4$, we averaged the EELS intensity profiles for line scans over different Sr-doped regions. Subsequently, the amplitude of

Fig. 5

(a) HAADF–STEM image of two-dimensionally doped La$_2$CuO$_4$ showing the microstructure of a superlattice (R=8, N= 7) grown on a LaSrAlO$_4$ (001) substrate. The alternation of brighter and darker areas reflects the superlattice structure, in which Sr-doped regions (dark) are separated by undoped La$_2$CuO$_4$ (bright). This is demonstrated by the maxima envelope of the image-intensity profile, integrated perpendicular to the growth direction (b, dark blue line). Scale bar, 2 nm. (b) The intensity oscillations of the intensity profile due to the different contrast of each atomic layer (green line). A magnified image of the region highlighted in red in (a) is shown in (e), in which the dotted yellow line corresponds to the layer having maximum Sr content. Scale bar, 1 nm. (c) [Sr]/[La] ratio, extracted from an EDX line scan across the region shown in (a). An asymmetric Sr distribution, extended in growth direction, is detected. Sr-L and La-L lines were used for quantification of the Sr concentration, and the integrated signals of Sr and La were calibrated using the substrate region where concentration ratio [La]/[Sr] is equal to unity. The error bars are the square root of the intensity. A similar Sr asymmetric profile results from the integration of the Sr-L$_{2,3}$ EELS line profiles, as shown in (d), which has been acquired across four Sr-containing layers (blue line in (a)). Here, the error bars (square root of the intensity) are smaller than the symbols. From the EELS analysis, the average Sr number per formula unit (FU, x in La$_{2-x}$Sr$_x$CuO$_4$), for each (La,Sr)O-CuO$_2$-(La,Sr)O 'constituting block' in proximity of the Sr-containing layers, as depicted in (f), was obtained (the standard deviation is represented by the error bars). Figures reproduced with permission from Ref. [31].
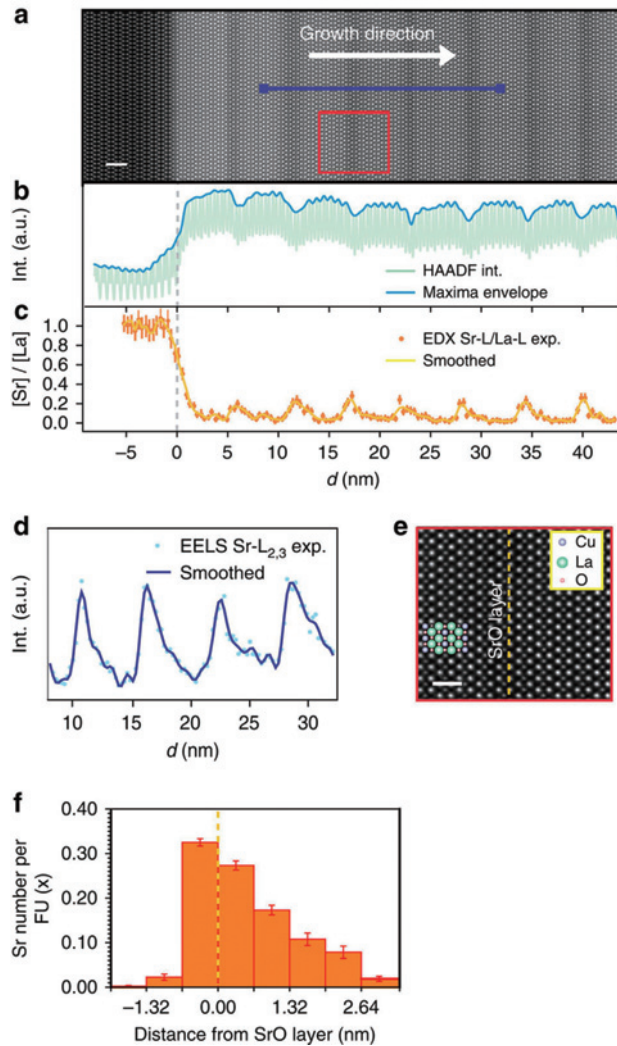
Fig. 6
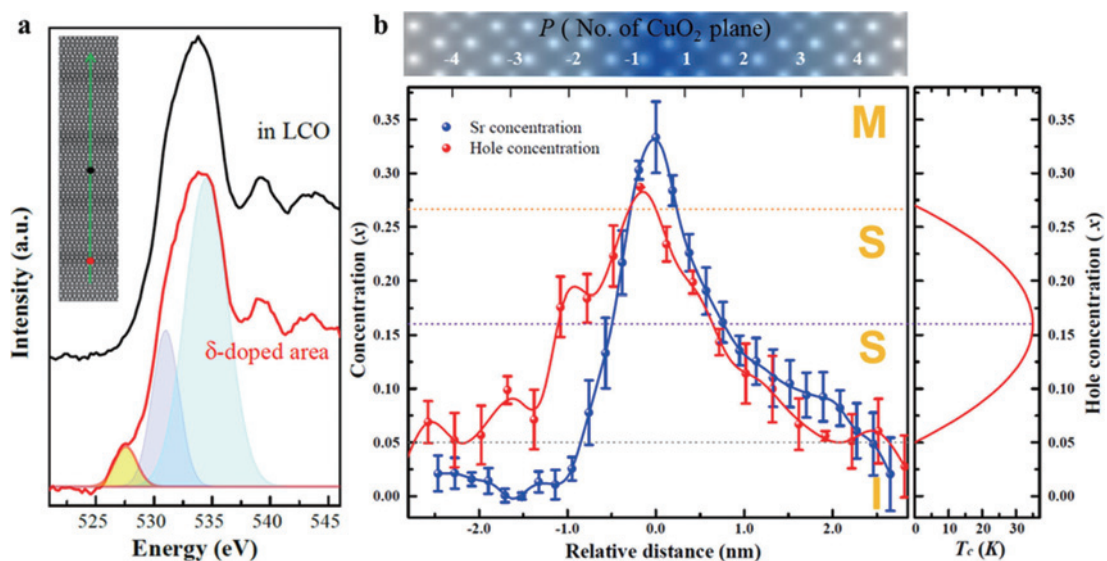
Concentration of holes and Sr^{2+} in the Sr-doped region. (a) EELS O-K edge spectra from a Sr-doped LCO region (red) and from undoped LCO (black). The O-K pre-edge intensity (yellow area) is present in the former. The Gaussian peaks used for NLLS fitting are shown. (b) Overlay of the electron hole and Sr concentration profiles as a function of the distance from the nominal Sr-doped layer position. The holes were quantified by multi-Gaussian peak fitting of the O-K edge in the energy-loss range 525-540 eV. In the top x-axis, P refers to the distance from the nominal position of the doped layer, expressed in number of CuO$_2$ planes (plus and minus signs refer to the upward and downward side of the interface, respectively). The right panel of (b) shows the generic phase diagram of HTSC, i.e. the dependence of T_c on the hole concentration by the empirical formula $T_c = T_c^{max}[1 - 82.6 (p - 0.16)^2]$, where p is the hole concentration [60,61]. From this, one can infer the corresponding T_c of any specific CuO$_2$ plane. Figures reproduced with permission from Ref. [30].

the hole profile was scaled to satisfy the charge neutrality condition and we obtained the Sr and hole concentrations as functions of the distance from the nominal SrO plane position shown in Fig. 6b (red and blue curves for holes and Sr, respectively). In the two profiles one can again observe the pronounced asymmetry of the Sr concentration whereas, most interestingly, the hole profile is symmetric around the nominal position ($x = 0$) of the SrO layer. Such a finding indicates that the distribution of the holes is remarkably different from the distribution of the Sr dopant atoms. This highlights that the region with CuO_2 atomic plane numbers $P = -4, -3$, and -2 is doped via a "nonconventional" mode, i. e., by heterogeneous (2D) doping [31]. The highly confined Sr dopant layer acts as a negatively charged region, which is electrically compensated via the formation of a hole accumulation layer (space-charge effect) on the downward side of the interface. On the upward side of the interface, the formation of a space-charge region is hindered by the broad Sr profile. In this case, the hole concentration follows the Sr^{2+} ion concentration as in conventional homogeneous (one-dimensional) doping.

To evaluate the local atomic distances across the Sr-doped interfaces, we again used simultaneously acquired HAADF and ABF images. **Figure 7**a presents the atomically resolved overlay of HAADF (blue) and ABF (red) images of an area covering four unit cells around the doped plane. The position of the nominal Sr-doped plane (marked by the yellow arrows in Fig. 7a) was obtained from the HAADF intensity profile. Subsequently, the interatomic apical (out-of-plane) and basal (in-plane) oxygen-to-oxygen (O–O) distances were measured by using the O–O picker software [37]. Figure 7 shows the

variations of the La–La spacing (b) and the O–O spacing (c) for each LCO perovskite block as a function of the distance from the nominal position of the SrO layer, which is marked by the dotted line ($x = 0$). The integer values on the top of the plot correspond to the CuO_2 plane belonging to the LCO blocks under consideration. In Fig. 7b, the in-plane (d_1) and out of-plane (d_2) La–La atomic distances are shown. The values of d1 are comparable with the in-plane lattice parameter of the substrate, suggesting that the film is under epitaxial compressive strain. The d_2 values are lower than the d_1 values and exhibit a maximum in correspondence with the highest Sr content (at $P = -1$), indicating that the Sr doping slightly expands the lattice of La_2CuO_4 along the c-axis. This finding is in good agreement with the literature data [35]. In our case, d_2 varies from 3.53 Å (at $P = -4$, where we expect the lowest Sr content) to 3.58 Å (at $P = -1$).

In Fig. 7c, we show the variations of the O–O distances (basal or in-plane (d_B, black line) and apical or out-of-plane (d_A, red line)) for each LCO perovskite block. The basal distance values correspond to those of the substrate as a consequence of epitaxial strain, while the apical distances are systematically larger, meaning that the CuO_6 octahedra are elongated along the c-axis. This can be explained in terms of a JT effect [33,36,56]. The d_A values vary significantly near the Sr-doped region and exhibit a maximum value at the $P = -2$ CuO_2 atomic plane ($d_A \approx 4.86$ Å) and a minimum value for $P = 1$ ($d_A \approx 4.57$ Å). The variation from the values measured two to three building blocks away from the Sr-doped plane (4.72–4.78 Å) is substantial, whereas far from the interface changes in d_A are as small as the measurement accuracy (about 4 pm) [37]. Interestingly, such a variation
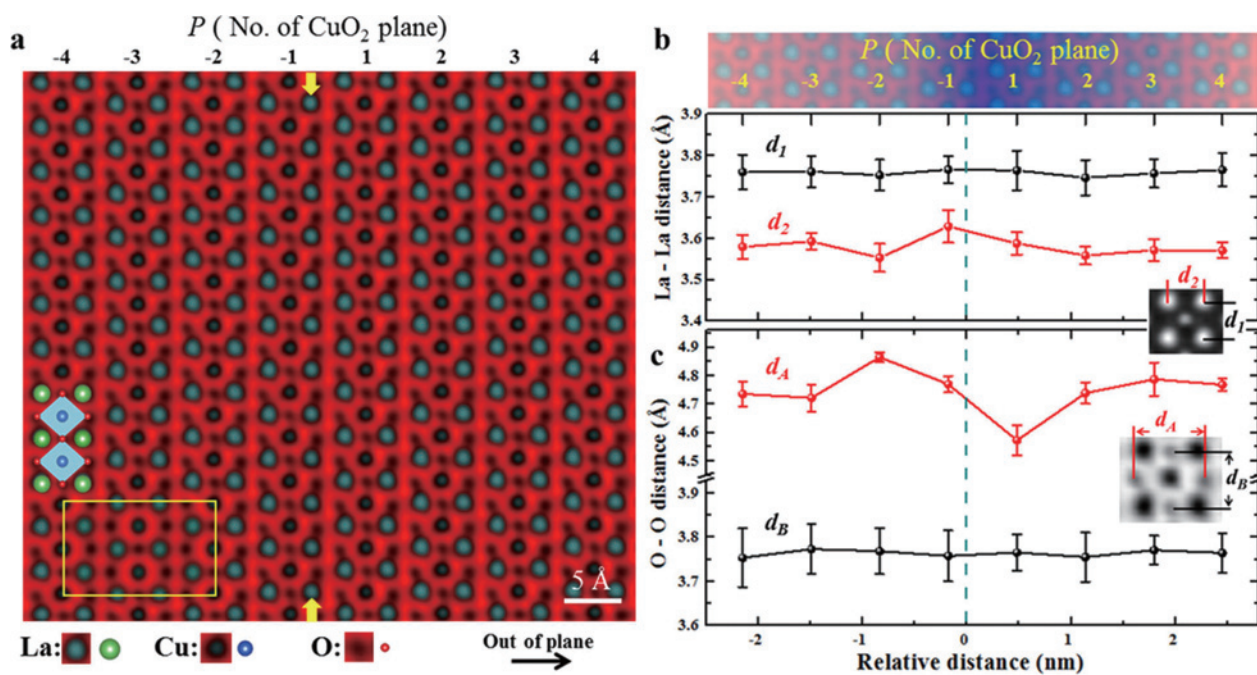
High resolution STEM image and quantitative analyses of structure distortion in the Sr-doped region. (a) Overlay of simultaneously acquired HAADF (blue) and ABF (red) images of one periodic structure of the Sr-doped region showing the cationic and anionic positions. The inset shows the simulated STEM image (marked with a yellow rectangle). The yellow arrows on the image indicate the nominal position of the SrO layer. (b) La-La atomic-column spacing along the in-plane (d_1) and out-of-plane (d_2) directions as a function of distance from the nominal Sr-doped layer. (c) O-O spacing along in-plane (basal, d_B) and out-of-plane (apical, d_A) directions as a function of distance from the nominal Sr-doped layer. The error bars give the 95% confidence interval (corresponding to 2 times the standard error) of the average of 13 unit cells of the pseudotetragonal perovskite lattice along the basal direction. Figures reproduced with permission from Ref. [30].

cannot be attributed to structural modifications stemming from the Sr distribution; if the reported values of the distance between Cu and apical-O are taken as a reference, i.e. half of the O–O distance under consideration (assuming that the Cu atoms are not significantly displaced from the center of the Cu–O octahedron), one expects small variations ($\approx$0.05 Å) upon Sr content change and a monotonic shrinkage of d_A upon Sr increase [17,39,41]. While this argument can be used to explain the measured minimum at $P = 1$, both the extent of the variation (about 0.2 Å from $P = -2$ to $P = 1$) and the presence of a maximum at $P = -2$ (where the Sr concentration is negligible) clearly indicate the occurrence of a structural anomaly on the downward side of the interface, where the heterogeneous doping mode is active. This anomaly occurs at the same position ($P = -2$) at which, according to complementary investigations, the optimal doping level for superconductivity is reached [30]. In a related system, the metal-insulator bilayers, in which the occurrence of interfacial high-temperature superconductivity was attributed to electron transfer, an "anomalous expansion" of the Cu–O distance at the interface was also found [8]. Such an asymmetric apical-oxygen displacement suggests a different JT effect at the two sides of the Sr-doped planes: (i) an anti-JT effect at the upward interface, where holes are located in both d_{x2-y2}, and d_{z2} orbitals, and (ii) an enhanced JT effect at the downward interface, where holes are located mainly in d_{x2-y2} orbitals [40].

Experimental

Scanning transmission electron microscopy

For representative cross-sectional electron transparent samples, a standard sample preparation procedure including mechanical grinding, tripod wedge polishing and argon ion milling with a liquid nitrogen-cooled stage was performed. For argon-ion thinning, a precision ion polishing system (PIPS II, Model 695) was used at low temperature. For all STEM analyses, a probe-aberration-corrected JEOL JEM-ARM200F STEM equipped with a cold field-emission electron source, a probe C_s-corrector (DCOR, CEOS GmbH), a large solid-angle JEOL SDD-type energy-dispersive X-ray (EDX) spectroscopy detector, and a Gatan GIF Quantum ERS spectrometer was used. STEM imaging and both EDXS and electron energy-loss spectroscopy (EELS) analyses were performed at probe semi-convergence angles of 20 mrad and 28 mrad, resulting in probe sizes of 0.8 Å and 1.0 Å, respectively. The collection angle range for high-angle annular dark-field (HAADF) images was 75–310 mrad. A collection semi-angle of 111 mrad was used for EELS investigations. For the ABF and HAADF images, frame series with short dwell times (2 μs/pixel) were used and added after cross-correlation alignment to improve the signal-to-noise ratio. In addition, STEM images and EELS data were processed with a multivariate weighted principal component analysis (PCA) routine (MSA Plugin in Digital Micrograph) to decrease the noise level [57]. Atomic-column positions and interatomic distances were measured from the ABF images with the Digital Micrograph software tool described in Ref [58]. In order to separate overlapping edges in each spectrum, such as La-$M_{5,4}$, Cu-$L_{3,2}$ and Ba-$M_{5,4}$ in our case, multiple linear least square fitting (MLLS) [59] was used. For overlapping signals, MLLS fitting windows of 650–1100 eV for Ba-$M_{5,4}$, La-$M_{5,4}$, Cu-$L_{3,2}$, 305–390 eV for Ca-$L_{3,2}$, and 1750–2100 eV for Sr-$L_{3,2}$ edges were used. The integration windows used for Ca-$L_{3,2}$, Ba-$M_{5,4}$, La-$M_{5,4}$, Cu-$L_{3,2}$, Sr-$L_{3,2}$, and edges are 343–

394 eV, 772–815 eV, 822–868 eV, 935–961 eV, 1935–2066 eV, respectively [29].

ALL-oxide MBE growth

La_2CuO_4 M-I bilayers [29] and 2D-doped La_2CuO_4 multilayers [31] were grown on $LaSrAlO_4$ (001) (LSAO) substrates (Crystec GmbH) using atomic-layer-by-layer (ALL) oxide MBE (DCA Instruments). The deposition conditions used for growing the samples were $T_s = 600$–620°C (pyrometer reading) at a pressure of $\sim 3\times10^{-5}$ Torr (mixed ozone, radical oxygen and molecular oxygen atmosphere). All samples were cooled in vacuum, from $T_s = 210$°C to room temperature, in order to exclude any influence on the electrical properties from interstitial oxygen doping.

Summary

In summary, we demonstrated the feasibility of using spherical aberration corrected STEM to quantitatively describe the elemental distribution, charge distribution and the local atomic distances in LCO-based superconducting interfaces. We found that the different cationic radii of the dopants remarkably affect the superconducting mechanisms (i.e. bulk vs interface) in La_2CuO_4 M–I bilayer systems, as a consequence of dopant distribution near the interface. In the case of the LCCO/LCO and LSCO/LCO systems, the interfaces were found to be sharper. As a consequence of such a different interface structure, distinct phenomena occur for inducing interface superconductivity: in the LCCO/LCO and LSCO/LCO cases, striking interface effects. i.e. electronic redistribution, are predominant, whereas, in the case of LBCO/LCO, HTSC is rather ascribed to "classical" homogeneous doping determined by cationic intermixing. Moreover, the dopant distribution has a significant effect on the O–O distance, in terms of JT and anti-JT distortions which can be related to different mechanisms leading to HTSC.

On the other hand, for 2D-doping we found the cationic dopant profile to be highly asymmetric: abrupt at the downward side of the interface and broadened in growth direction. Conversely, the hole distribution, as measured by EELS, is symmetric across the interface and is decoupled from the dopant profile at the downward interface. This indicates that hole doping is achieved on the two sides of the Sr-doped plane by two distinct mechanisms, heterogeneous doping at the downward side of the interface and homogeneous doping at the upward side.

References

[1] H. Y. Hwang, Y. Iwasa, M. Kawasaki, B. Keimer, N. Nagaosa, Y. Tokura, *Nat. Mater*., **11** (2012) 103.

[2] J. Mannhart, D. G. Schlom, *Science*, **327** (2010) 1607.

[3] P. Zubko, S. Gariglio, M. Gabay, P. Ghosez, J. -M. Triscone, *Annu. Rev. Condens. Matter Phys*., **2** (2011) 141.

[4] A. Gozar, G. Logvenov, L. F. Kourkoutis, A. T. Bollinger, L. A. Giannuzzi, D. A. Muller, I. Bozovic, *Nature*, **455** (2008) 782.

[5] G. Logvenov, V. V. Butko, C. DevilleCavellin, J. Seo, A. Gozar, I. Bozovic, *Phys. B Condens. Matter*, **403** (2008) 1149.

[6] G. Logvenov, A. Gozar, I. Bozovic, *Science*, **326** (2009) 699.

[7] V. Y. Butko, G. Logvenov, N. Božović, Z. Radović, I. Božović, *Adv. Mater*., **21** (2009) 3644.

[8] H. Zhou, Y. Yacoby, V. Y. Butko, G. Logvenov, I. Božović, R. Pindak, *Proc. Natl. Acad. Sci*., **107** (2010) 8103.

[9] S. Smadici, J. C. T. Lee, S. Wang, P. Abbamonte, G. Logvenov, A. Gozar, C. D. Cavellin, I. Bozovic, *Phys. Rev. Lett*., **102** (2009) 107004.

[10] A. Suter, E. Morenzoni, T. Prokscha, B. M. Wojek, H. Luetkens, G. Nieuwenhuys, A. Gozar, G. Logvenov, I. Božović, *Phys. Rev. Lett*., **106** (2011) 237003.

[11] E. Stilp, A. Suter, T. Prokscha, E. Morenzoni, H. Keller, B. M. Wojek, H. Luetkens, A. Gozar, G. Logvenov, I. Božović, *Phys. Rev. B*, **88** (2013) 064419.

[12] Y. Yacoby, H. Zhou, R. Pindak, I. Božović, *Phys. Rev. B*, **87** (2013) 014108.

[13] J. Wu, O. Pelleg, G. Logvenov, A. T. Bollinger, Y. -J. Sun, G. S. Boebinger, M. Vanević, Z. Radović, I. Božović, *Nat. Mater*., **12** (2013) 877.

[14] M. Haider, S. Uhlemann, E. Schwan, H. Rose, B. Kabius, K. Urban, *Nature*, **392** (1998) 768.

[15] E. Okunishi, I. Ishikawa, H. Sawada, F. Hosokawa, M. Hori, Y. Kondo, *Microsc. Microanal*., **15** (2009) 164.

[16] S. D. Findlay, N. Shibata, H. Sawada, E. Okunishi, Y. Kondo, Y. Ikuhara, *Ultramicroscopy*, **110** (2010) 903.

[17] S. D. Findlay, Y. Kohno, L. A. Cardamone, Y. Ikuhara, N. Shibata, *Ultramicroscopy*, **136** (2014) 31.

[18] Z. Liao, M. Huijben, Z. Zhong, N. Gauquelin, S. Macke, R. J. Green, S. Van Aert, J. Verbeeck, G. Van Tendeloo, K. Held, G. A. Sawatzky, G. Koster, G. Rijnders, *Nat. Mater*., **15** (2016) 425.

[19] D. Kan, R. Aso, R. Sato, M. Haruta, H. Kurata, Y. Shimakawa, *Nat. Mater*., **15** (2016) 432.

[20] S. J. Pennycook, D. E. Jesson, *Phys. Rev. Lett*., **64** (1990) 938.

[21] Y.-M. Kim, A. Kumar, A. Hatt, A. N. Morozovska, A. Tselev, M. D. Biegalski, I. Ivanov, E. A. Eliseev, S. J. Pennycook, J. M. Rondinelli, S. V. Kalinin, A. Y. Borisevich, *Adv. Mater*., **25** (2013) 2497.

[22] R. Aso, D. Kan, Y. Shimakawa, H. Kurata, *Adv. Funct. Mater*., **24** (2014) 5177.

[23] R. Aso, D. Kan, Y. Fujiyoshi, Y. Shimakawa, H. Kurata, *Cryst. Growth Des*., **14** (2014) 6478.

[24] D. Kan, R. Aso, H. Kurata, Y. Shimakawa, *Dalton Trans*., **44** (2015) 10594.

[25] Z. Liao, Z. Li, J. Zhu, *J. Am. Ceram. Soc*., (2016) n/a.

[26] F. Baiutti, G. Cristiani, G. Logvenov, *Beilstein J Nanotechnol*., **5** (2014) 596.

[27] W. Lee, J. W. Han, Y. Chen, Z. Cai, B. Yildiz, *J. Am. Chem. Soc*., **135** (2013) 7909.

[28] R. D. Shannon, *Acta Crystallogr. Sect. A*, **32** (1976) 751.

[29] Y. E. Suyolcu, Y. Wang, F. Baiutti, A. Al-Temimy, G. Gregori, G. Cristiani, W. Sigle, J. Maier, P. A. van Aken, G. Logvenov, *Sci. Rep*., **7** (2017) 453.

[30] Y. Wang, F. Baiutti, G. Gregori, G. Cristiani, U. Salzberger, G. Logvenov, J. Maier, P. A. van Aken, *ACS Appl. Mater. Interfaces*, **8** (2016) 6763.

[31] F. Baiutti, G. Logvenov, G. Gregori, G. Cristiani, Y. Wang, W. Sigle, P. A. van Aken, J. Maier, *Nat. Commun*., **6** (2015) 8586.

[32] H. Sato, A. Tsukada, M. Naito, A. Matsuda, *Phys. Rev. B*, **62** (2000) R799.

[33] Kamimura, H., *Theory of Copper Oxide superconductors*;

[34] J. B. Boyce, F. Bridges, T. Claeson, T. H. Geballe, C. W. Chu, J. M. Tarascon, *Phys. Rev. B*, **35** (1987) 7203.

[35] P. G. Radaelli, D. G. Hinks, A. W. Mitchell, B. A. Hunter, J. L. Wagner, B. Dabrowski, K. G. Vandervoort, H. K. Viswanathan, J. D. Jorgensen, *Phys. Rev. B*, **49** (1994) 4163.

[36] Y. E. Suyolcu, Y. Wang, W. Sigle, F. Baiutti, G. Cristiani, G. Logvenov, J. Maier, P. A. van Aken, *Adv. Mater. Interfaces*, **4** (2017) 1700737.

[37] Y. Wang, U. Salzberger, W. Sigle, Y. Eren Suyolcu, P. A. van Aken, *Ultramicroscopy*, **168** (2016) 46.

[38] L. Taillefer, *Annu. Rev. Condens. Matter Phys*., **1** (2010) 51.

[39] D. Haskel, E. A. Stern, F. Dogan, In *Phase Transitions and Self-Organization in Electronic and Molecular Networks*; Thorpe, M. F.; Phillips, J. C., Eds.; Fundamental Materials Research; Springer US, 2002; pp. 323–330.

[40] D. Haskel, V. Polinger, E. A. Stern, In *AIP Conference Proceedings*; AIP Publishing, 1999; Vol. 483, pp. 241–246.

[41] J. Maier, *Prog. Solid State Chem*., **23** (1995) 171.

[42] A. Ohtomo, D. A. Muller, J. L. Grazul, H. Y. Hwang, *Nature*, **419** (2002) 378.

[43] A. Bhattacharya, S. J. May, S. G. E. te Velthuis, M. Warusawithana, X. Zhai, B. Jiang, J.-M. Zuo, M. R. Fitzsimmons, S. D. Bader, J. N. Eckstein, *Phys. Rev. Lett*., **100** (2008) 257203.

[44] B. Jalan, S. Stemmer, S. Mack, S. J. Allen, *Phys. Rev. B*, **82** (2010) 081103.

[45] K. Nishio, M. Matvejeff, R. Takahashi, M. Lippmaa, M. Sumiya, H. Yoshikawa, K. Kobayashi, Y. Yamashita, *Appl. Phys. Lett*., **98** (2011) 242113.

[46] S. A. Pauli, P. R. Willmott, *J. Phys. Condens. Matter*, **20** (2008) 264012.

[47] K. S. Takahashi, M. Kawasaki, Y. Tokura, *Appl. Phys. Lett*., **79** (2001) 132.

[48] P. Lupetin, G. Gregori, J. Maier, *Angew. Chem. Int. Ed*., **49** (2010) 10123.

[49] E. F. Schubert, *J. Vac. Sci. Technol. Vac. Surf. Films*, **8** (1990) 2980.

[50] R. Dingle, H. L. Störmer, A. C. Gossard, W. Wiegmann, *Appl. Phys. Lett*., **33** (1978) 665.

[51] D. A. Muller, L. F. Kourkoutis, M. Murfitt, J. H. Song, H. Y. Hwang, J. Silcox, N. Dellby, O. L. Krivanek, *Science*, **319** (2008) 1073.

[52] N. Nücker, J. Fink, J. C. Fuggle, P. J. Durham, W. M. Temmerman, *Phys. Rev. B*, **37** (1988) 5158.

[53] N. Nücker, H. Romberg, X. X. Xi, J. Fink, B. Gegenheimer, Z. X. Zhao, *Phys. Rev. B*, **39** (1989) 6619.

[54] N. D. Browning, J. Yuan, L. M. Brown, *Phys. C Supercond*., **202** (1992) 12.

[55] H. Romberg, M. Alexander, N. Nücker, P. Adelmann, J. Fink, *Phys. Rev. B*, **42** (1990) 8768.

[56] H. A. Jahn, E. Teller, *Proc. R. Soc. Lond. Math. Phys. Eng. Sci*., **161** (1937) 220.

[57] M. Bosman, M. Watanabe, D. T. L. Alexander, V. J. Keast, *Ultramicroscopy*, **106** (2006) 1024.

[58] Y. Wang, U. Salzberger, W. Sigle, Y. E. Suyolcu, P. A. van Aken, *Microsc. Microanal*., **22** (2016) 930.

[59] The use of MLLS fitting approach to resolve overlapping edges in the EELS spectrum at the atomic level | Gatan, Inc.

[60] J. B. Torrance, A. Bezinge, A. I. Nazzal, T. C. Huang, S. S. P. Parkin, D. T. Keane, S. J. LaPlaca, P. M. Horn, G. A. Held, *Phys. Rev. B*, **40** (1989) 8872.

[61] H. Takagi, T. Ido, S. Ishibashi, M. Uota, S. Uchida, Y. Tokura, *Phys. Rev. B*, **40** (1989) 2254.

Springer: New York, 2005.

Technical Development of Electron Cryomicroscopy and Contributions to Life Sciences

Keiichi Namba and Takayuki Kato   Graduate School of Frontier Biosciences, Osaka University

The three-dimensional structure of biological macromolecules and their complexes is the fundamental information not only for life sciences but also for medical sciences and drug design. Electron cryomicroscopy is now attracting much attention as a powerful tool for high-resolution structural analysis in addition to X-ray crystallography and NMR that have been used as the basic techniques. How can the structures of biomolecules be imaged and analyzed at atomic level resolution in their native states despite that they are easily damaged by a relatively low level of electron irradiation? This paper describes the history and present state of our own technological development in electron cryomicroscopy and also future expectations and prospects by further development.

Introduction

The 2017 Nobel Prize in Chemistry was awarded to Jacques Dubochet (University of Lausanne, Switzerland), Joachim Frank (Columbia University, USA), and Richard Henderson (MRC Laboratory of Molecular Biology, UK), for their pioneering works in the development of electron cryomicroscopy and image analysis for the structural analysis of biological macromolecules, such as proteins and nucleic acids. The three-dimensional (3D) structure of biomolecules is the basic and important information not only for life sciences but also for medical sciences and drug design, and electron cryomicroscopy (cryoEM) has become a powerful tool for high-resolution structural analysis over the past several years and now established its position as one of the essential techniques for structural analysis in addition to conventional X-ray crystallography and NMR. Electron cryomicroscopy receives much attention because it can achieve near-atomic resolution in structural analysis only with a very small amount of solution samples, as small as a few tens of μgs, without the need of crystallization. The Nobel Prize was awarded to recognize the contributions of the above three researchers as the founders of this technology. Here, we describe the concept of electron cryomicroscopy and image analysis as a technique for structural biology, the history and present state of our own technological development, and the future potential of this technique for life and medical sciences through further development.

Structural analysis of biological macromolecules by electron cryomicroscopy

The basic mechanisms that drive and support biological activities are highly shared by diverse organisms, from microorganisms, such as bacteria and yeast, to multicellular organisms, such as

animals and plants as well as humans with higher-order brain functions. All of these functions are determined based on the structures of proteins and nucleic acids with 3D arrangements of so many atoms, from a few thousands to tens of thousands. Moreover, their structures are not solid like bulk materials of metals and ceramics but are very dynamic and flexible and are designed to function by actively utilizing thermal fluctuations. One of the major challenges in life science is the elucidation of mechanisms that determine and express these functions, and it is necessary to look at the 3D structures of so many biological macromolecules in various states that are involved in various biological functions. The number of 3D structures we need to solve would range from a few hundreds of thousands to a few million.

The powerful feature of cryoEM, especially single particle image analysis, is that there is no need for sample crystallization that is essential for X-ray crystallography and that there is virtually no upper limit in the size of molecular complexes unlike NMR. However, since the majority of the interatomic bonds that maintain their 3D structures are non-covalent bonds, such as hydrogen bonds, salt bridges and van der Waals contacts, the structures are very sensitive to electron beam irradiation damage, a few orders of magnitude worse than that of metals, ceramics and semiconductors. Therefore, to record high-resolution images of biological macromolecules in their native state without much damage, it is necessary to embed them in an amorphous ice thin film by rapidly freezing their aqueous solutions and record their images by a transmission electron cryomicroscope (cryoTEM) with a specimen stage cooled by liquid helium or liquid nitrogen to a low enough temperature to prevent the vitreous ice from converting to crystalline states. Even at such low temperatures, the electron dose that can be irradiated without much damage to the atomic-level structures is limited to 20 to 30 e⁻/Å², and so cryoEM images tend to be extremely poor due to the intrinsic statistical noise, which is

〉〉 1-3 Yamadaoka, Suita, Osaka, 565-0871, Japan | E-mail: keiichi@fbs.osaka-u.ac.jp

due to a relatively small number of electrons detected in each pixel of an image detector, and the Landau noise, which is due to a large distribution of signal levels of individual electron detection. Since individual molecular images recorded by a cryoTEM are the 2D projection images of molecules embedded in the amorphous ice film in various orientations, it is also necessary to collect a large number of images that are sufficient to cover different orientations with even distributions in order to reconstruct the 3D image at high resolution. So, it is essential to efficiently collect as many molecular images as possible, classify them into each orientation of projection, and obtain an averaged image for each orientation by aligning the position and orientation of the molecular images to increase the signal level while reducing the noise. This procedure is called 2D class average. Then, the relative relationships between the 2D class averaged images in the orientation of projection are determined, and finally the 3D image of the molecule can be reconstructed (**Fig. 1**). To achieve high-resolution structural analysis, it is important to use a cryoTEM and an image detector both capable of efficiently collecting high-quality, high-resolution cryoEM images. High-precision image-analysis programs and high-speed computers are also required. We will describe the history of our own development of cryoTEM systems to solve such problems and some of the achievements by using them.

Fig. 1 Schematic diagram explaining the process of single particle image analysis.
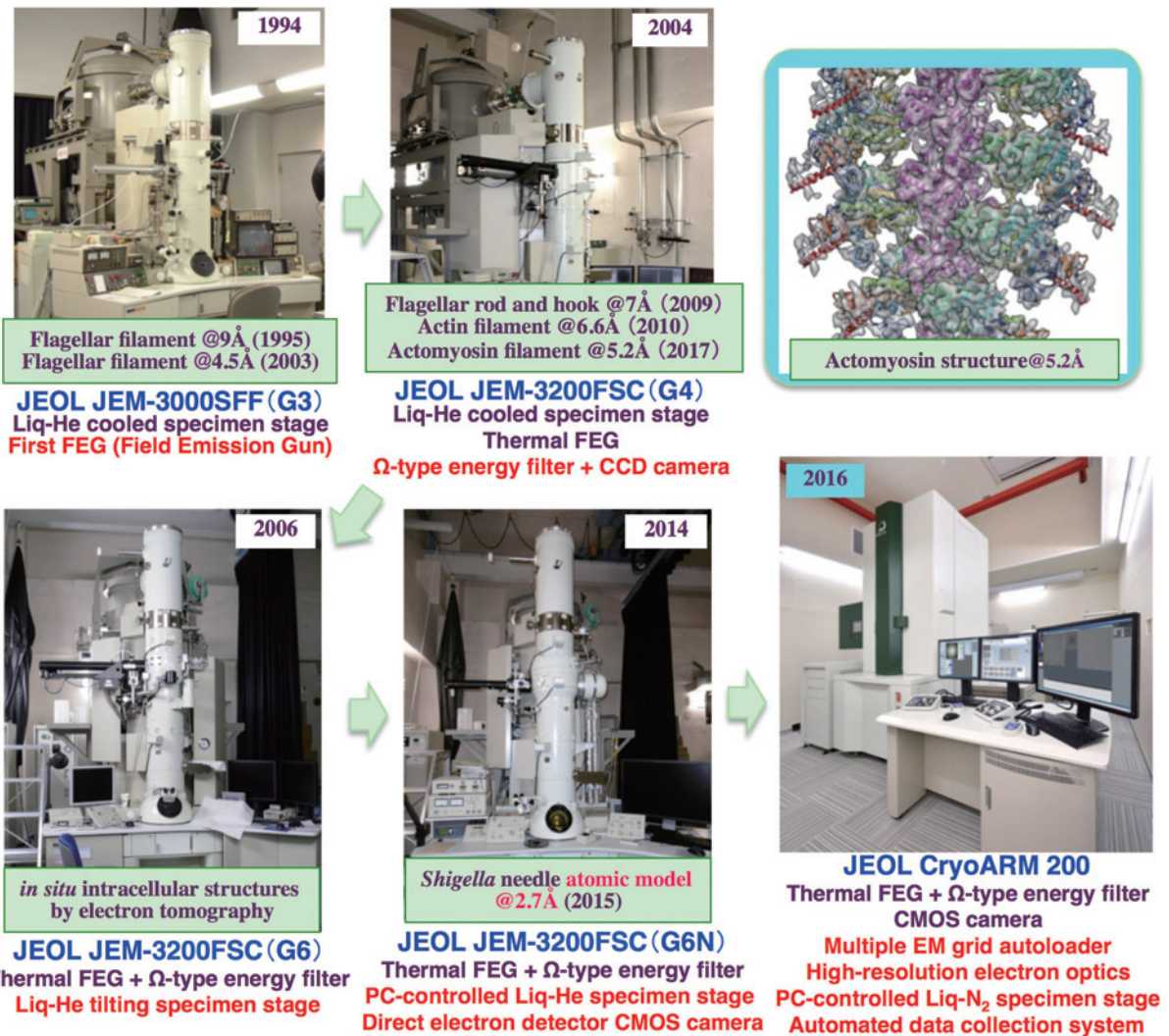
Dolphins represent biomolecules embedded in a thin film of vitreous ice in various orientations. CryoEM images correspond to their 2D projections with high noise levels. After the S/N is greatly increased by going through 2D classification and average of many 2D projections, a 3D image can be reconstructed.

Advances in cryoTEM, image detector and methods of data collection and analysis

Field emission electron gun

The pioneer of the cryoEM field in Japan is Yoshinori Fujiyoshi (Visiting Professor, Nagoya University). In collaboration with JEOL, he designed and developed a cryoTEM with a very stable, liquid helium-cooled specimen stage for the first time in the world to minimize the electron beam irradiation damage to the limit to enable recording of high-quality cryoEM images of biological macromolecules [1]. I started collaborating with him from around 1990 to start using electron cryomicroscopy for the structural analysis of the bacterial flagellar filament to understand its assembly and supercoiling mechanism. We had been using X-ray fiber diffraction and X-ray crystallography to those days because the achievable resolution by electron cryomicroscopy was rather limited then, but I recognized the potential of the cryoTEM with the liquid helium-cooled specimen stage for high-resolution structural analysis. He taught us the basics of cryoEM techniques from cryoEM grid preparation to minimum-dose imaging of frozen-hydrated ice-embedded protein complexes. Then, a year or so later, I was offered a job from Tsuneharu Nitta, Director of the Central Research Laboratories of Panasonic (Matsushita Electric Industrial Co., Ltd. at the time), to start my own laboratory in a subdivision of the Advanced Technology Research Laboratory, which Panasonic was planning to establish in KeiHanNa Science City as its new basic-research oriented R&D center. The subdivision was called the International Institute for Advanced Research (IIAR), and I was promised to have a generous funding for the development of new equipments for X-ray structural analysis and electron cryomicroscopy. So I asked Yoshinori Fujiyoshi to join this new Panasonic institute to start the IIAR together as an advanced structural biophysics research center. We asked JEOL to introduce a newly developed device, a Schottky-type field emission electron gun (Thermal FEG), to the above-mentioned cryoTEM with the liquid helium-cooled specimen stage. This was the very first cryoTEM with an FEG and was named JEM-3000SFF (Generation 3: G3) (**Fig. 2**) [1]. Panasonic established the new KeiHanNa institute in 1994, and we moved into the new building and set up our laboratories with
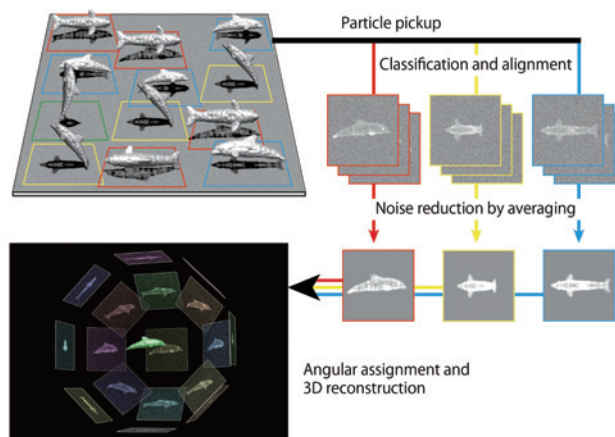
this new cryoTEM. We expected a significant improvement in the quality and resolution of EM images by the high coherence of its electron beam by field emission. The improvement was actually remarkable, showing up much higher resolution signals in every cryoEM image we collected. The Fujiyoshi group aimed to solve the structures of membrane proteins, such as bacteriorhodopsin and aquaporin, in two-dimensional crystals, and our group aimed at analyzing the structure of large helical assemblies of macromolecules, such as the bacterial flagellar filaments. Because only photographic films were available as the image detector in those days, the efficiency and throughput of high-quality image data collection were very poor. So it took more then several years for the structural analyses to reach near-atomic resolution, but we were able to obtain many impactful results by the mid-2000s, with atomic-resolution structures of membrane protein 2D crystals and macromolecular complexes [2-6]. Our structural analysis of the bacterial flagellar filament attained a resolution close to 4 Å by careful image analysis of highly-selected high-quality cryoEM images of the filaments corresponding to only 40,000 flagellin molecules, and the polypeptide backbone folding and large side chains were clearly resolved (**Fig. 3**) [6].

CCD camera and Ω-type energy filter

The Graduate School of Frontier Biosciences was established in Osaka University in 2002, and we moved our laboratory to the Nanobiology building in 2004. Just before that, we obtained a government funding from the MEXT as part of its supplementary budget and asked JEOL to introduce a couple of newly developed devices to the cryoTEM with the liquid helium-cooled specimen stage. This was JEM-3200FSC (Fig. 2) and was an improved version of Fujiyoshi's fourth generation cryoTEM (G4) [1] that was introduced to the Riken Harima Research Institute at the SPring-8 site. One of the new devices was an improved version of the in-column Ω-type energy filter, and this was introduced to improve the signal to noise ratio (S/N) of cryoEM images by removing the majority of inelastically scattered electrons, which lost the coherence due to energy loss and therefore contribute only to the high background noise and not to the high-resolution EM image. We found nearly two-fold improvement in the image S/N just by this energy filter [7]. Another device was a 4K × 4K CCD image detector (TVIPS F415MP), which was already used

Fig. 2 Development history of cryoTEMs in our group.

1994

Flagellar filament @9Å (1995)
Flagellar filament @4.5Å (2003)

JEOL JEM-3000SFF(G3)
Liq-He cooled specimen stage
First FEG (Field Emission Gun)

2004

Flagellar rod and hook @7Å (2009)
Actin filament @6.6Å (2010)
Actomyosin filament @5.2Å (2017)

JEOL JEM-3200FSC(G4)
Liq-He cooled specimen stage
Thermal FEG
Ω-type energy filter + CCD camera

Actomyosin structure@5.2Å

2006

in situ intracellular structures
by electron tomography

JEOL JEM-3200FSC(G6)
Thermal FEG + Ω-type energy filter
Liq-He tilting specimen stage

2014

Shigella needle atomic model
@2.7Å (2015)

JEOL JEM-3200FSC(G6N)
Thermal FEG + Ω-type energy filter
PC-controlled Liq-He specimen stage
Direct electron detector CMOS camera

2016

JEOL CryoARM 200
Thermal FEG + Ω-type energy filter
CMOS camera
Multiple EM grid autoloader
High-resolution electron optics
PC-controlled Liq-N₂ specimen stage
Automated data collection system

Newly incorporated elemental technologies and equipments are indicated in red characters.

Fig. 3 Molecular structure of the flagellar filament revealed by cryoEM image analysis.

Filament

Flagellar motor

The bacterial flagellum is a motility organelle with a rotary motor and a helical filamentous propeller. The flagellar filament is a large helical assembly of tens of thousands of flagellin molecules. By using the JEM-3000SFF cryoTEM and photographic films as the image detector, we collected cryoEM images and solved the structure of the flagellar filament at around 4 Å resolution. The main chain folding and many large side chains were clearly visualized for the first time by cryoEM image analysis of biomolecules, and this allowed us to build a complete atomic model of this huge protein assembly.

for electron diffraction recording but not for imaging due to its lower resolving power than photographic films. Its resolving power is lower because each electron forming an EM image has to be converted to photons by a thin layer of scintillator on top of the glass-fiber coupling block and the image of each electron becomes blurred by the electron scattering within the scintillator. Even with this disadvantage, the CCD markedly improved the efficiency and throughput of high-quality image data collection because we can see the EM image and its Fourier transform immediately after exposure, and this allows us to make a quick and reliable judgement on the quality and resolution of individual cryoEM images during data collection [7]. We were also able to dramatically improve the efficiency of high-quality image data collection further by increasing the specimen temperature from 4 K to around 50 K by stopping the supply of liquid helium from the in-column tank to the top-entry specimen pod. Although the radiation damage can be minimized at 4 K, most of the cryoEM images suffered from local, directionally biased image blurring due to the charge up upon electron beam irradiation because of the extremely poor electrical conductivity of the thin specimen ice film at the extremely low temperature. It was less than a few % of collected images that could be used for image analysis. We solved this difficult problem by increasing the specimen temperature to about 50 K, and almost all of the collected images became sufficiently high quality to be used for image analysis [7].

These technological improvements and advances made previously multi-year projects completed within a couple of weeks from data collection to 3D image reconstruction and allowed us to solve the structures of many different, interesting biomolecular assemblies, such as the bacterial flagellar hook, muscle actin filament, the ParM filament that segregates plasmids for bacterial cell division, the thin needle tube of the virulence type-III secretion system of pathogenic bacteria and the actomyosin rigor complex, all at 5 - 7 Å resolutions. We were able to build reliable atomic models to gain insights into the mechanisms of their functions by docking and refining the available crystal structures to the 3D maps [7-12]. The structure of the stacked disk formed by the tobacco mosaic virus coat protein was solved at 3.8 Å resolution also within a couple of weeks to allow many of the side chains to be visualized (Takashi Fujii, unpublished).

Side entry liquid helium-cooled stage

The liquid helium-cooled specimen stage developed by Fujiyoshi in the 1980's was the top entry type. It was mechanically very stable, but electron cryotomography could not be done because the stage had no tilting mechanism. Special contrivance was made for imaging 2D crystals in many different tilt angles to cover much of the 3D Fourier space for high-resolution 3D image reconstruction, but it was still time consuming. So Fujiyoshi decided to redesign his top entry stage to implement a tilting mechanism and applied for a MEXT budget called Special Coordination Funds for the Promotion of Science and Technology for its development by JEOL, and I joined this project as a co-proposer. The one developed in this project is the cryoTEM of Generation 6 (G6) (Fig. 2). JEOL built two of them and delivered to Kyoto University and Osaka University in 2006 [1]. One of our main research subjects is the bacterial flagellar motor, which rotates the supercoiled flagellar filament as a helical propeller to produce thrust for bacterial swimming motility. We need detailed structural information of the flagellar basal body spanning the cell membranes to understand the mechanism of motor rotation, but the important components of the motor, such as the stator units, are dissociated from the basal body during its isolation and

purification by detergent solubilization because of their weak binding, and therefore the structure of the flagellar motor cannot be observed in its functional states when isolated from the cell. So what we aimed to do with this new cryoTEM was to establish the method of electron cryotomography (ECT) to observe the *in situ* structures of biomolecular complexes inside the cells. We tried to establish the ECT method with this new cryoTEM with a tilt mechanism to visualize the functional motor structure in the cell membranes by quickly freezing the entire bacterial cells on a specimen grid and record many of their tilt images to reconstruct 3D images of the cells with the flagellar basal bodies. However, since the diameter of the *Salmonella* cells are nearly 1 µm thick and the specimen thickness for the electron beam to pass through becomes twice thicker at 60° tilt, which is too thick even for 300 keV electrons to pass through and scatter elastically to form EM images of good quality, we had to wait for several years to visualize the *in situ* structure of the basal body until we have introduced a genetic engineering technique to produce "mini-cell" to make *Salmonella* cells much smaller than the wild-type [13].

In order to further improve the efficiency and throughput of image data collection for single-particle image analysis, we decided in 2011 to change the specimen stage to the side entry type of JEOL's original design with a potential to make automated data collection possible by computer control. This modified version of cryoTEM is G6N (Generation 6 with New Modification) (Fig. 2).

The introduction of this specimen stage together with a different type of objective lens pole piece has resulted in improved usability and image resolution beyond our expectations. One of the standard methods to examine the highest possible image resolution of a cryoTEM is to take an EM image of a test specimen, such as an amorphous platinum-iridium (Pt/Ir) alloy thin film, under a relatively large defocus condition of about 1 µm and look at its Fourier transform to see how far the Thon ring extends (see Fig. 4). This is what we routinely do to examine the resolution of cryoEM images of frozen-hydrated ice-embedded specimens, and such a large defocus is necessary to enhance the image contrast of low resolution to make ice-embedded biomolecules visible for image analysis. By using a thin film of alloy, we are not limited by a low electron dose that we must use to avoid radiation damage to see the weak Thon ring signal at the highest possible resolution. By such a test of image resolution performed on the installation completion date of the cryoTEM G6N, we were able to see the Thon ring extending beyond 2.0 Å resolution. In order to make the Thon ring extend to the highest possible resolution under such defocus conditions, the electron optical system of the cryoTEM must be set to produce a parallel illumination beam on the specimen. It was fortunate that the objective lens pole piece of this cryoTEM was designed to fulfill such requirement under almost any imaging conditions that users set up to collect images even being unconscious of parallel illumination condition.

However, there were some other problems. Although the specimen stage was liquid helium-cooled, the specimen temperature was slightly higher than that of the G4 top-entry type, and the temperature could not be elevated to 50 K as we did with the G4 top-entry type. In addition, the supply of helium was limited around the world and prices were rising. Our microscope facility was connected with a helium recovery pipe to the Low Temperature Center of Osaka University in the same campus, but our helium recovery line frequently caused trouble on the Low Temperature Center operation by contaminating air. So we decided to stop using liquid helium around 2012. We filled liquid nitrogen in both the liquid nitrogen tank and

the liquid helium tank of the cryoTEM G6N and found that the specimen temperature can be kept stably at 77 K, exactly at the liquid nitrogen temperature for 7 to 8 hours. By fully utilizing the CCD camera-controlling software provided by TVIPS, nearly automated data acquisition became possible, and this made cryoEM image data collection very efficient.

CMOS-based direct electron detector camera

And finally, the bright time of the cryoEM field had come along in 2013 by the arrival of a CMOS-based direct electron detector camera. David Agard and his colleagues at the University of California, San Francisco, had been developing an EM image detector in collaboration with Gatan, one of the major EM camera manufacturers by repurposing a CMOS device for X-ray image detectors developed by a group at the University of California, Berkeley. Gatan completed the development of this camera system and made it commercially available in 2013 as K2 Summit. The CMOS imaging chip had wonderful specifications, having 4K by 4K pixels, being robust against direct irradiation of high-energy electrons accelerated to 300 keV or even higher, and showing a minimal image blur due to electron scattering within the very thin electron-detecting semiconductor layer, and best of all, the data acquisition rate of 16 million pixel image was 400 frames per second, which made it possible to carry out single electron counting. Because the total electron dose typically used for cryoEM image recording is 20 to 30 e⁻/Å over one second exposure, the number of electrons coming onto the detector plane per each frame becomes limited and countable if the dose rate is lowered by about 10 fold by making the exposure time 10 fold longer. Single electron counting gives us a great advantage in reducing the image noise level. One of the major noise sources in cryoEM image recording is the statistical noise, which is large relative to the signal because the number of electrons forming individual cryoEM images is small due to the low-dose imaging to avoid radiation damages. There is no way to escape from it. However, single electron counting can minimize the Landau noise, which is an intrinsic noise of detector caused by a large distribution in the signal amplitude that any type of energy-accumulating image detector, such as CCD, produces for individual electron detection.

Yifan Cheng at the University of California, San Francisco, made the most of the performance of this CMOS camera system and devised a way to collect sharp high-quality cryoEM images of proteins by movie-mode imaging and motion correction. He and his colleagues successfully analyzed the 3D structure of a membrane protein, the TRPV1 receptor ion channel, which senses heat and spiciness, from a small amount of solution sample that eluded crystallization over many years in spite of much effort by a group of his colleagues, and published two papers in *Nature* at the end of 2013 [14, 15]. The structure was solved at 3.4 Å resolution by analyzing about 100,000 single-particle images of the protein picked up from about 1,000 cryoEM images obtained from a small amount of sample solution containing the detergent-solubilized protein. After individual frame processing for single electron counting, they added up every 80 frames to make a cryoEM movie of 5 frames/sec and then added up these movie frames with motion correction to minimize the image blur caused by a mechanical drift of the specimen stage and the distortion of ice film caused by electron irradiation to make the final cryoEM image very sharp [16].

We were able to introduce Gatan K2 Summit to our cryoTEM G6N (Fig. 2) in 2015 and tried to utilize its high performance as an image detector. The movie mode image recording allowed us to capture the structures of various biomolecules including membrane proteins at near-atomic resolution, and the highest resolution we attained was 2.7 Å for the structure of the thin needle tube of the *Shigella* type III virulence-factor secretion system (Takashi Fujii & Yurika Yamada, unpublished). Since the attainable resolution depends largely on the structural stability of the sample molecule and the thickness of the ice thin film on the cryoEM grid, it should be possible to achieve resolution exceeding 2.0 Å with a better specimen and grid.

Development of CRYO ARM™

The FEI company (Thermo Fisher Scientific since 2017), one of the major manufacturers of electron microscopes, started developing high-performance user-friendly cryoTEMs for researchers in life sciences around the end of the 1990's and produced cryoTEMs called Polara in 2004 and Titan Krios in 2008. Titan Krios is in particular a user-friendly system, capable of storing 12 cryoEM grids in a magazine, allowing users to load each grid onto the specimen stage cooled by liquid nitrogen to around 90 K by automatic loading device (autoloader), and allows automated image data collection by specifying areas for image recording after users judged the quality of grid. Titan Krios has been highly evaluated by many users in the cryoEM field over the world because of its high performance in attaining high resolution and user-friendliness both in the 3D observation of cellular structures by ECT and single particle image analysis because both techniques require many cryoEM image data to be collected.

JEOL developed JEM-ARM200F (ARM: Atomic Resolution Microscope) in 2009 as a high resolution TEM for material research and received high evaluation in the world. So we thought JEOL should develop an ARM-based cryoTEM utilizing its ultra-high resolution electron optics by developing necessary devices, such as a highly-stable computer-controlled liquid nitrogen-cooled specimen stage that can maximize the performance of high-resolution electron optics, a cryoEM grid autoloader that is more user-friendly and convenient to use than that of Titan Krios, and a liquid nitrogen automatic filling system, and also by adding the Ω-type in-column energy filter to minimize the inelastically-scattered electrons to increase the S/N of the recorded images. The Ω-filter is also useful for quickly measuring the thickness of ice film for the evaluation and judgement of the quality of the EM grid. Just at the right timing, a large funding named State-of-Art Research Infrastructure Establishment Program was announced by JSPS, and the proposal and application for the funding by Toshio Yanagida as Director of Riken Quantitative Biology Center (QBiC) (also, Specially Appointed Professor and Professor Emeritus of Osaka University; Director of the Center for Information and Neural Networks) was approved in 2010 for the preparation for the establishment of Riken QBiC. This budget was allocated to Riken and Osaka University for their collaborative research activities. We proposed to use part of the budget to develop a user-friendly high-resolution cryoTEM and obtained an approval to ask JEOL to develop it. We conveyed our idea, vision and required specifications to the technical team of JEOL, and they agreed to start the development. JEOL planned to complete a prototype cryoTEM by the spring of 2014, and we had many discussions repeatedly over many meetings. The nickname we came up for this new cryoTEM was CryoARM, and JEOL named it CRYO ARM™ (Fig. 2). One of the goals we set was to exceed 2.0 Å as the attainable resolution in the structural analysis of biomolecular complexes.

Although the development was delayed due to various circumstances and reasons, a prototype cryoTEM was finally installed in May 2016 in the Nanobiology building. According to the initial design plan made at the time when a Cold FEG

was not yet available, this prototype CRYO ARM was installed with a Thermal FEG with an acceleration voltage of 200 kV. We examined the Thon ring in the Fourier transform of the Pt/Ir thin film images recorded under 1 μm defocus and confirmed that the Thon ring extended beyond 1.8 Å resolution (**Fig. 4**). Our important mission started from this point. We prepared cryoEM grids of many different biomolecular specimens and collected cryoEM images to analyze their structures by single particle image analyses to evaluate the performance of the cryoTEM for the resolution. We also carefully examined and evaluated various aspects of the cryoTEM, such as the user-friendliness of cryoTEM operation and controlling software, quickness and smoothness of the manual operation with the cryo-workstation for cryoEM grid transfer as well as autoloader operation, the efficiency of data collection by automated image recording, and the points to be improved in the automated data acquisition software JADAS towards completely-automated data collection, to feed them back to JEOL engineers. As sort of we predicted, so many mechanical troubles frequently occurred with the autoloader and cryo-workstation, and JEOL engineers had to redesign the systems and parts, sometimes with new materials, and bring them from Akishima, Tokyo, to replace with the old ones and make adjustments of sensors and actuators to fix those troubles. It was almost every other week for about half a year from the installation. The specimen stage was largely redesigned for higher stability, and the TEM system controlling software was also improved including the introduction of one-click buttons on display to achieve parallel illumination and coma-free optics alignment. The cryoEM method holds up with so much knowledge accumulated over the years of its development, and a cryoTEM system can work well only by implementing and realizing all those essential know-how and specifications. JEOL engineers worked really hard to make this cryoTEM system work as we desired. It was February 2017 when every function of this prototype CRYO ARM™ finally started working stably, and we never had any serious troubles since then.

We used β-galactosidase as a test sample to see the reachable resolution of structural analysis with image data collected with CRYO ARM™. We also continued our evaluation of the operation stability of the hardware and software for further improvement and especially focused on JADAS, an automated data acquisition software program that JEOL has been developing over the years, to make it something that every cryoEM user can use comfortably for efficient data collection. JADAS became practically usable after several updates, and in the summer of 2017 we were able to collect 2,500 images from a cryoEM grid of β-galactosidase over 3 days. We picked up about 350,000 single particle images from them, selected about 88,000 good ones by going through 2D and 3D classifications by Relion 2.0 [17] and obtained a 3D reconstruction at 2.6 Å resolution (**Fig. 5**) (Takayuki Kato, EMDB ID: 6840).

JEOL announced CRYO ARM™ 200 and CRYO ARM™ 300 in June 2017 as the commercial products, for which the numbers represent the accelerating voltage. The good news was that JEOL was able to equip these cryoTEMs with its own stable Cold FEG and Hole-Free Phase Plate. The phase plate should manifest its power for relatively small biomolecules with their molecular mass below 150 kDa. The coherence of the electron beam from the Cold FEG is significantly higher than that of the Thermal FEG because of its small energy dispersion by about two fold, and therefore this should greatly enhance the image signal of high resolution. In fact, when the defocused images of the Pt/Ir thin film were compared between Cold FEG and Thermal FEG, the difference was clear. While the resolution

limit indicated by the Thon ring remained at about 1.8 Å with the 200 kV Thermal FEG, the Thon ring extended to about 1.5 Å with the 200 kV Cold FEG and to 1.1 Å with the 300 kV Cold FEG (**Fig. 6**). This implies that our dream of 1 Å resolution would come true with the structural analysis of biomolecules in the aqueous solution sample if we could develop and incorporate a super-stable cryo-specimen stage (Fig. 6). It would also be possible to greatly improve the throughput of cryoEM structural

---

Fig. 4 Thon ring of the Pt/Ir thin film image recorded with the prototype CRYO ARM™.
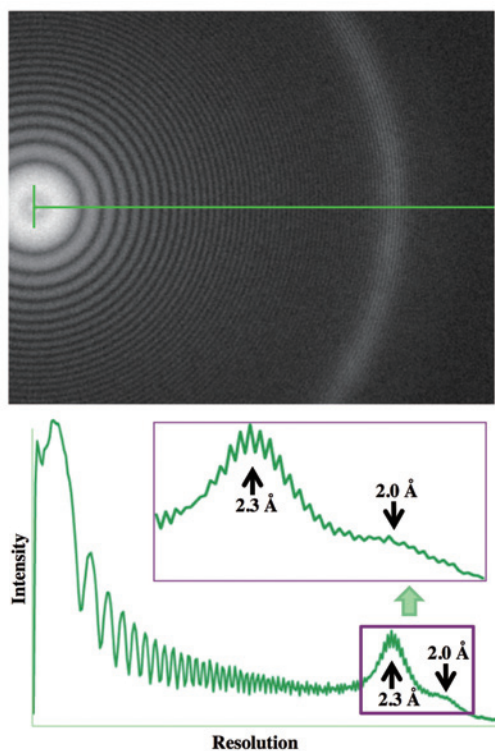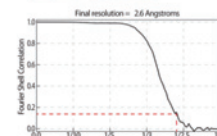

A cryoEM image of the Pt/Ir thin film was taken under 1 μm defocus with the prototype CRYO ARM™ operated at 200 kV. The Thon ring in its Fourier transform extended to 1.8 Å resolution.

**Fig. 5 Structure of β-galactosidase at 2.6 Å resolution by CRYO ARM™.**
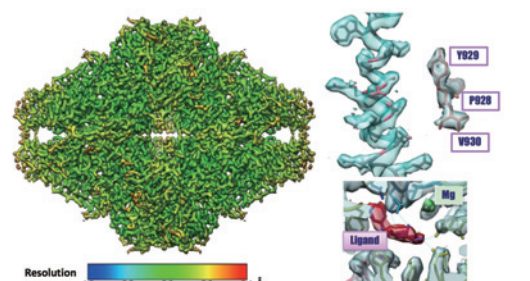
While the overall resolution of the entire molecule is 2.6 Å resolution, the local resolutions are not homogeneous as indicated in rainbow colors. Some parts of the molecule show a resolution close to 2.0 Å, and Thr 929, for example, shows a hole at the center of its six-membered ring.

Fig. 6 Effect of Cold FEG in high-resolution signal enhancement and 3D maps of various resolutions.
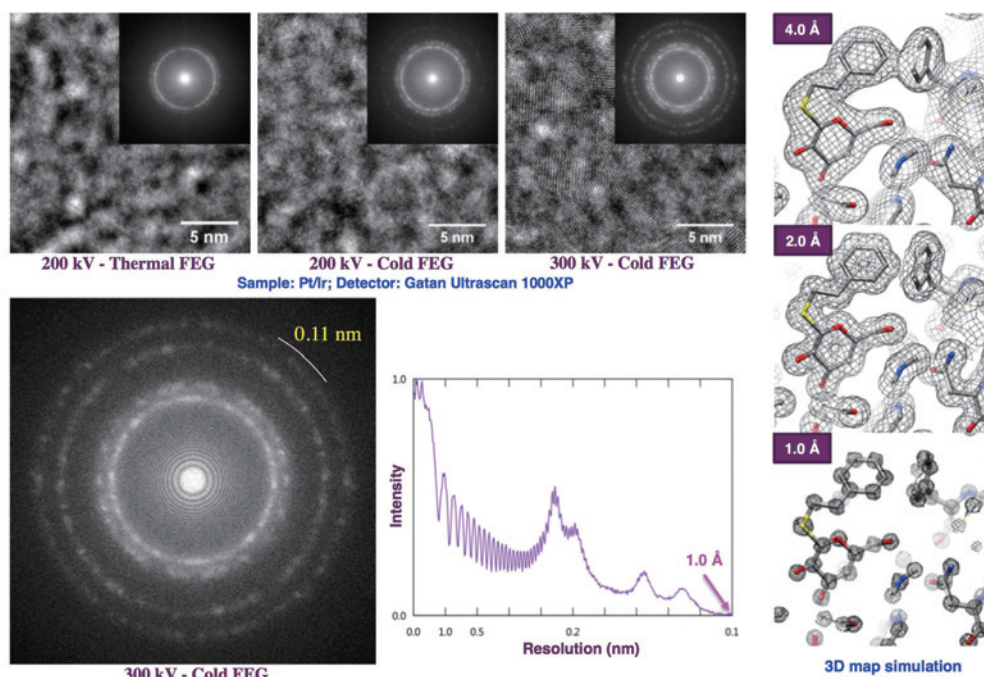
EM images of the Pt/Ir thin film were recorded under 1 μm defocus either with Thermal FEG or Cold FEG, and the insets are their Fourier transforms. The 3D maps are calculated from the superimposed atomic model at different resolutions to demonstrate the visible features at each resolution. The map at 4.0 Å shows a typical feature visualized by recent cryoEM image analyses, with the overall shape of side chains being resolved, but the one at 1.0 Å clearly resolves individual atoms. The EM images were collected and analyzed by Hirofumi Iijima, Takeshi Kaneko, Sohei Motoki, Isamu Ishikawa and Yoshihiro Ohkura at JEOL.

analysis by developing and advancing pipeline software programs that carry out image analysis in real time with data collection and AI software programs that judge the quality of images being collected to make appropriate decisions without human intervention to select better imaging areas on the grid or change the grid to the next one in the autoloader storage to find a better one. In order to tackle these technical challenges, our joint effort in technological development with JEOL is still underway.

Concluding remarks

Since all the functions and mechanisms that support life activities in living organisms are determined by the dynamic networks of biomolecules through their interactions, it is essential to elucidate the structures of the biomolecular complexes going through association and dissociation in atomic detail. Now, by recent advances in cryoEM techniques, the structures and intermolecular interactions have become increasingly visible for countless biomolecules that had previously been beyond our approach due to technical limitations, such as difficulty in crystallization or too large molecular size. The roles of cryoEM for the advancement of life sciences, medical sciences and drug design are immense. It is no exaggeration to say that the promotion of technological development in the cryoEM field to maximize its power is one of the most important issues for the future of human society.

Acknowledgment

References

[1] Fujiyoshi, Y: *JEOL News* **44**, 23-31 (2009).

[2] Kimura Y, Vassylyev DG, Miyazawa A, Kidera A, Matsushima M, Mitsuoka K, Murata K, Hirai T, Fujiyoshi Y: *Nature* **389**, 206-211 (1997).

[3] Murata K, Mitsuoka K, Hirai T, Walz T, Agre P, Heymann JB, Engel A, Fujiyoshi Y: *Nature* **407**, 599-605 (2000).

[4] Miyazawa A, Fujiyoshi Y, Unwin N: *Nature* **423**, 949-955 (2003).

[5] Gonen T, Cheng Y, Sliz P, Hiroaki Y, Fujiyoshi Y, Harrison SC, Walz T: *Nature* **438**, 633-638 (2005).

[6] Yonekura K, Maki-Yonekura S, Namba K: *Nature* **424**, 643-650 (2003).

[7] Fujii T, Kato T, Namba K: *Structure* **17**, 1485-1493 (2009).

[8] Fujii T, Iwane AH, Yanagida T, Namba K: *Nature* **46**, 724-8 (2010).

[9] Gayathri P, Fujii T, Møller-Jensen J, van den Ent F, Namba K, Löwe J: *Science* **338**, 1334-1337 (2012).

[10] Fujii T, Cheung M, Blanco A, Kato T, Blocker AJ, Namba K: *Proc. Natl. Acad. Sci. USA* **109**, 4461-4466 (2012).

[11] Fujii T, Namba K: *Nature Commun*. **8**, 13969 (2017).

[12] Fujii T, Kato T, Hiraoka KD, Miyata T, Minamino T, Chevance FF, Hughes KT, Namba K: *Nature Commun*. **8**, 14276 (2017).

[13] Kawamoto A, Morimoto YV, Miyata T, Minamino T, Hughes KT, Kato T, Namba K: *Sci. Rep*. **3**, 3369 (2013).

[14] Liao M, Cao E, Julius D, Cheng Y: *Nature* **504**, 107-112 (2013).

[15] Cao E, Liao M, Cheng Y, Julius D: *Nature* **504**, 113-118 (2013).

[16] Li X, Mooney P, Zheng S, Booth CR, Braunfeld MB, Gubbens S, Agard DA, Cheng Y: *Nature Methods* **10**, 584-590 (2013).

[17] Kimanius D, Forsberg BO, Scheres SH, Lindahl E. *Elife* **15**, e18722 (2016).

Electronic State Analysis by Monochromated STEM-EELS

Hiroki Kurata   Institute for Chemical Research, Kyoto University

High energy resolution electron energy-loss spectra can be measured over a wide energy range from infrared to soft X-ray region by using a monochromated transmission electron microscope. In this report, as an example of spectra in visible light region, the study on the dielectric substrate effects on localized surface plasmons in metallic nanoparticles is presented. Moreover, carbon K-edge spectra measured from organic crystals, which are expected to benefit from high energy resolution in the measurement of near-edge fine structures, are also shown. Especially, the spectral changes due to the chlorination of copper-phthalocyanine molecules are discussed.

Introduction

Many efforts to improve the energy resolution of electron energy-loss spectroscopy (EELS) incorporated in a transmission electron microscope (TEM) have been made so far. Recently, the development of a new generation monochromator has made it possible to characterize materials with high energy and spatial resolution by using it together with a spherical aberration corrected scanning transmission electron microscope (STEM). In this report, after briefly introducing the performances of a (scanning) transmission electron microscope equipped with a monochromator installed at Institute for Chemistry Research of Kyoto University, the author will show two examples of high energy resolution EELS experiments. One is the study of localized surface plasmon (LSP) excited in silver nanoparticles (NPs) supported on MgO crystal. It will be shown that the excitation probability of LSP depends on the trajectory of an incident electron probe. The other is the application of energy-loss near-edge structure (ELNES) appearing in carbon K-edge excitation spectra to organic crystal. Owing to the small lifetime broadening of the initial and final states, the fine structures inherent to the molecule are observe in carbon K-edge ELNES, leading to apply to molecular analysis.

Monochromated STEM-EELS (JEM-ARM200F)

Figure 1 shows an appearance of a monochromated (scanning) transmission electron microscope (JEOL; JEM-ARM200F). The monochromator consisted of double Wien filters and deflection coils is incorporated between the Schottky type electron gun and the accelerating tube [1]. An energy dispersed focused beam is formed in the lower part of the first Wien filter, and monochromatization of electrons is performed by inserting an energy selection slit at the dispersion plane. The second filter plays a role of focusing the monochromated beam into an achromatic beam. For this reason, the electrons emitted from the electron source and the electrons focused at the exit plane of monochromator have a 1: 1 relationship. The energy dispersion of the Wien filter is 12.3 μm/eV, and the energy width of electrons is able to be selected by changing the width of the slit. There are seven types of slit widths between 0.1 μm and 4 μm in this device. When inserting a slit, the energy resolution estimated from the full width at half maximum of zero-loss peak can be chosen from 30 meV to 250 meV. The spherical aberration correctors (CEOS; CESCOR and CETCOR) for illumination and imaging lens systems are installed in a column, which makes it possible to perform the high spatial resolution STEM and TEM observations. As analytical apparatuses, an imaging filter (Gatan; Quantum ESR) and an energy dispersed X-ray spectrometer (JEOL; JED-2300T SDD100GV) are equipped with this microscope. The accelerating voltage of 200 kV or 60 kV can be selected, so measurement with low accelerating is also possible. **Figure 2** shows the zero-loss peak when an energy selection slit of 0.1 μm is inserted at an accelerating voltage of 200 kV. For comparison, the spectrum measured by a cold field emission gun (Cold-FEG) is also shown. The full width at half maximum of the peak is 33 meV, which is one order of magnitude narrower than that of Cold-FEG, and the tail intensity of the zero-loss peak in the near infrared region of 1 eV or less is greatly reduced. In this way, since the measurable region of the spectrum has extended to low energy side, it has become possible not only to demonstrate its power in the study of surface plasmons as described below but also to detect vibrational excitations [2, 3].

Dielectric substrate effects on localized surface plasmons

When light or electron is irradiated onto metal NPs, surface modes called localized surface plasmons (LSPs) are excited. This is due to collective oscillation of valence electrons on the surface, and the nano-particle surface is accompanied by strong near-field

light. Since the resonance condition of LSP is sensitive to the size of the particle and the surrounding environment, its application to biosensors or photocatalysts has been extensively studied. In order to investigate the physical properties of LSP in more detail, it is necessary to analyze single NPs with high spatial resolution. High energy resolution EELS combined with STEM is a powerful tool for research on LSP, because EEL spectra in the near infrared region can be measured efficiently with sub nm spatial resolution. Many studies on LSP have been reported using this method [4]. In the following, the author will introduce the study of dielectric substrate effect on LSP excited in a silver NP.

Figure 3 shows the results of high energy resolution STEM-EELS measured from a silver NP supported on MgO substrate [5]. The feature of this measurement is that the electron probe is incident on the interface between the substrate and the NP in parallel, allowing us to directly investigate substrate effects on LSP excitations as a function of the distance from the substrate. Spectrum-image (SI) data were obtained with an energy resolution of 70 meV, a collection semi-angle of 29.2 mrad and a spatial sampling of 0.4 nm per pixel. The high-angle annular dark-field (HAADF) image in Fig. 3(a) demonstrates that the silver NP has an almost spherical shape with a diameter of 14 nm. Figure 3(b)

shows the spectra extracted from top (indicated by A), side (B) and gap (C) regions around the NP, at a distance of 1 nm from the surface of the particle, as shown in Fig. 3(a). The LSP resonance energy is slightly different depending on the position of the incident probe, and the resonance energy at the top position (A) of the particle is shifted by 80 meV lower energy than the side position (B). The EELS map using the intensity of 3.40 ± 0.20 eV near the resonance energy is shown in Fig. 3(c). Due to the presence of the MgO substrate, the LSP excitation distribution excited in the spherical silver NP is asymmetric; the highest intensity is observed at the top position apart from the interface, while the intensity at the gap position is very weak. Such peak shift and asymmetric intensity distribution are considered to be the effects of the dielectric substrate on the LSP. In order to understand this, we performed simulations by discrete dipole approximation (DDA) for a silver NP on an MgO substrate.

Figure 4(a) presents the EEL spectra calculated for three different electron trajectories, as shown in the model (inset), consisting of a silver nanosphere with a diameter of 14 nm and an MgO substrate with a semi-infinite size. These results are compared with the spectrum calculated for an isolated silver NP in a vacuum, indicated by the black line. The calculation was performed using

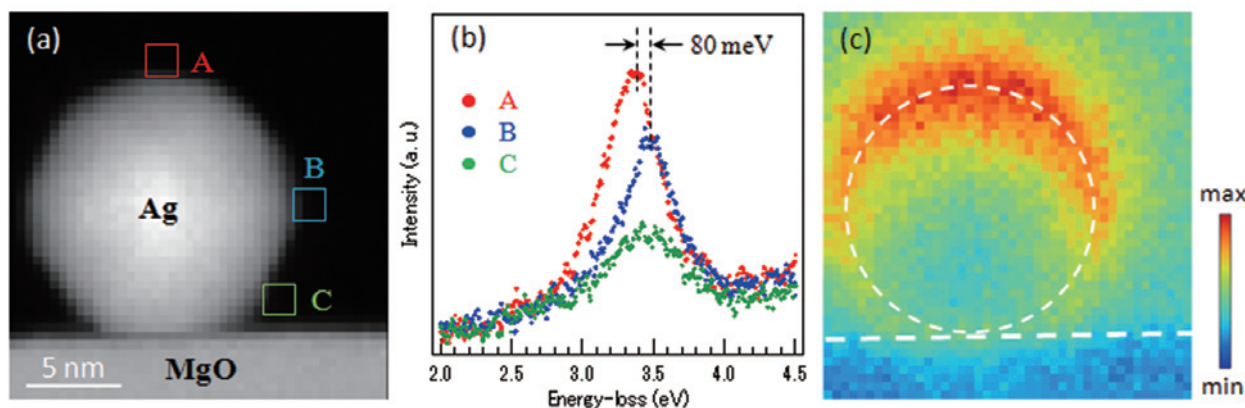**Fig. 1 Appearance of JEM-ARM200F equipped with a monochromator**

Fig. 2 Zero-loss spectra acquired with a monochromated gun (red) and cold-FEG (blue)
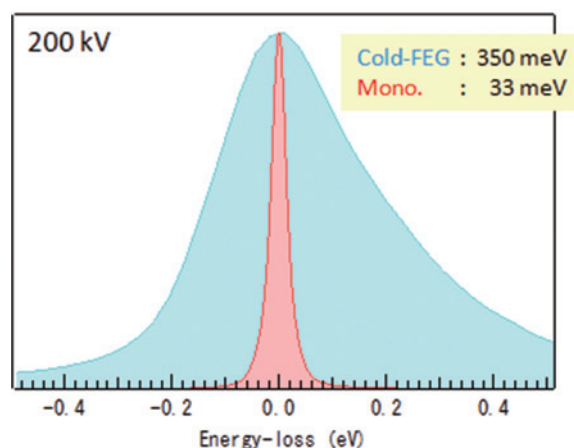
An energy selection slit of 0.1 mm is inserted. An accelerating voltage is 200 kV.

Fig. 3 Localized surface plasmon excited in a silver NP supported on MgO crystal

(a) HAADF image. (b) EEL spectra extracted from three different positions. (c) EELS map using the intensity of LSP resonance peak.

a DDEELS code [6] and the dielectric function of silver reported by Palik [7]. The dielectric function of MgO was assumed to be a constant value of 3.13 [8]. The LSP resonance energy and the peak intensity depending on the electron trajectories well reproduce the experimental results of Fig. 3(b). The LSP peaks of the NP on the substrate appear at slightly lower energy values than that of the isolated NP. This red shift of LSP peaks represents the substrate effect. On the other hand, the difference in resonance energy at the electron trajectory A and B is related to the polarization direction of the dipole mode of the LSP excited in the silver NP. The LSP dipole modes for which the polarization is perpendicular or parallel to the substrate are excited by electrons having trajectories A and B, respectively. The resonance energy shift depending on the direction of polarization of the LSP with respect to the substrate has also been observed in experiments using linearly polarized light [9]. It should be emphasized that the results equivalent to the experiment of polarized light can be obtained with high spatial resolution by selecting the electron trajectory in the STEM-EELS experiment. The intensity of the LSP peak measured at trajectory A is strong compared to that for an isolated NP, while that for trajectory C is considerably weaker. This characteristic intensity distribution is also noticeable in the EELS map shown in Fig. 4(b), which is calculated from the intensity at 3.40 eV. The LSP excitation probability for the NP is enhanced at the top surface, far from the dielectric substrate, and is suppressed in the gap region. The simulated map reproduces well the experimental EELS map of Fig. 3(c).

Next, the reason why the spatial distribution of the LSP excitation probability becomes asymmetric is considered. In the DDEELS code, the metallic NP is considered as an aggregate of discrete dipoles. The excitation probability of EELS is calculated by summing the product of the dipole moment $\mathbf{P}_j$ at position $\mathbf{r}_j$ and the electric field $\mathbf{E}_j^{app}$ applied by an incident electron. The dipole moment is proportional to the local electric field, which is the superposition of the applied field and the fields resulting from other dipoles. To a first approximation, therefore, the energy-loss probability is expected to be strongly affected by the distribution of the applied electric field depending on the location of the incident electron. In the case of NPs supported on a substrate, not only the structural symmetry is reduced, but also the intensity distribution of the applied electric field is modified by the polarization of the dielectric substrate compared to the case of an isolated NP. The effect of the substrate on the applied

electric field can be assessed based on the image charge model. The polarization field of the substrate due to an incident electron at (x_e, y_e, z_e) can be described by an image charge, q, located at $(-x_e, y_e, z_e)$ in the substrate when the substrate surface is at x=0. The total electric field applied to the dipole is equal to the sum of the fields generated by the electron and its image charge $q=(1-\varepsilon_{MgO})e(1+\varepsilon_{MgO})$, where ε_{MgO} is the dielectric function of MgO and e is the electron charge. Since ε_{MgO} is greater than 1 in the visible light region, q is positive, such that the polarization field of the substrate acts to enhance the applied field of the incident electron in the region between the electron and its image charge. **Figure 5** shows the calculated applied field, including the substrate effect, for a silver NP with a diameter of 14 nm supported on an MgO crystal. When the incident electron is located at the top surface of the NP, the applied electric field covers the majority of the NP as in Fig. 5(a), meaning that many dipoles are excited in the NP, leading to a high energy-loss probability. In contrast, when the electron is incident in the vicinity of the interface between the NP and the substrate (Fig. 5(c)), the applied field in the NP is weak and its distribution is limited to the region near the interface. This is attributed to the strong cancellation of field in the NP region by the polarization of the substrate, because the NP is located in the opposite direction to the image charge with respect to the position of the incident electron. Therefore, the energy-loss probability becomes low in the vicinity of the interface. In the case of an electron travelling near the side of the NP (Fig. 5(b)), the applied field distribution in the NP is similar to that in an isolated NP (Fig. 5(d)). Therefore, the substrate effect is weak and limited to the region between the incident electron and the interface, which is essentially a vacuum, leading to a similar LSP peak intensity (Fig. 4(a)). The above modifications of the applied field due to the substrate cause the asymmetric distribution observed in the EELS map shown in Fig. 3(c).

The presence of a dielectric substrate under the NP can affect the spatial distribution of the LSP excitation probability as well as its resonance energy. The dipole mode of the LSP excited in a spherical NP splits into two modes corresponding to oscillations parallel or perpendicular to the substrate surface. These modes could be probed separately using different electron trajectories, providing results identical to those obtained from polarized light analyses.

Fig. 4 Simulated results by DDEELS
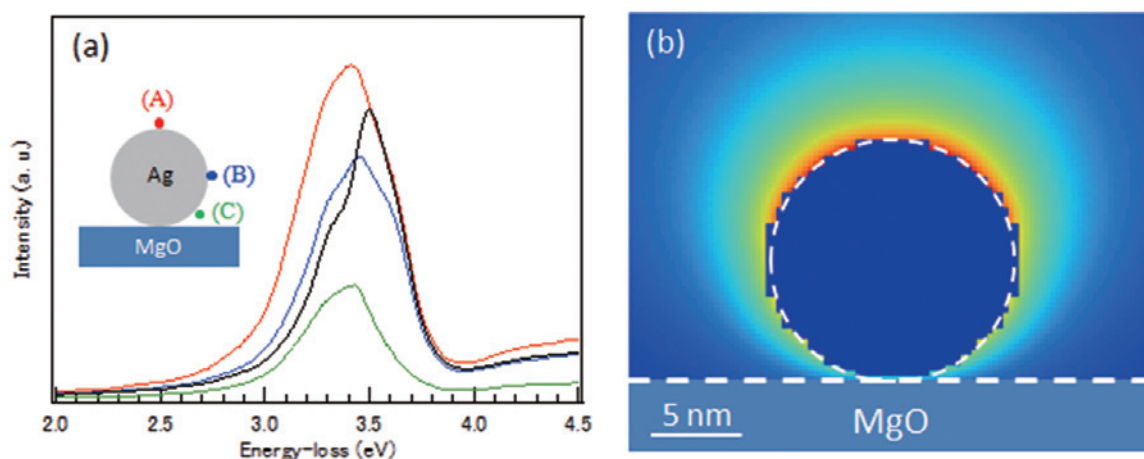
(a) Calculated spectra at three different electron positions shown in the inset and the spectrum for an isolated silver NP (black).
(b) Calculated EELS map using the intensity of LSP resonance peak.

High resolution EELS of organic thin films

In the measurement of energy-loss near-edge structure (ELNES) appearing in inner-shell electron excitation spectrum, the energy resolution is limited by the lifetimes of initial and final states and the density of states in conduction band as well as the energy spread of the primary beam and the resolution of spectrometer. When an inner-shell electron excited into unoccupied electronic band, a hole is left in the core level. The lifetime of the core hole determines the energy width of the initial state, which is related to the generation of characteristic X-ray and Auger electrons due to decay of electrons existing at shallow levels than the core hole. The energy widths of core levels calculated theoretically show a tendency that it is broader at the core level having larger binding energy [10], indicating that ELNES of shallow core level benefits from improved energy resolution. On the other hand, the energy broadening due to the lifetime of final state depends on the kinetic energy of excited electron. It has been shown that the final state broadening calculated by using the inelastic mean free path of excited electron has very narrow near the threshold region, and becomes broad with increasing the kinetic energy [11]. Considering the lifetime broadening of initial and final states, therefore, it can be said that the effect of high energy resolution appears in the spectral structure near the absorption edge excited from a relatively shallow core level. Furthermore, ELNES reflects the partial density of states of unoccupied band, the band dispersion also affects the broadening of spectrum. Actually, it has been reported that the oxygen K-edge ELNES measured from some transition metal oxides does not improve even with monochromated EELS, which is mainly due to the effect of band dispersion (solid-sate effects) [12]. In the case of organic thin film crystals described below, however, the interaction between molecules is weak and the band dispersion is small, so it is expected that monochromated EELS will be of benefit for ELNES appearing just above the threshold of carbon K-edge with a relatively small binding energy. The spectral features specific to conjugated molecules will appear as sharp π^*-resonance peaks.

Figure 6(a) shows the carbon K-edge ELNES measured from copper-phthalocyanine (CuPc) and chlorinated copper-phthalocyanine (CuPcCl$_{16}$) thin films. CuPc is a four-fold symmetric planar molecule in which copper atom is coordinated

at the center of the porphyrin ring as shown in Fig. 6(b). CuPcCl$_{16}$ is produced by substituting the peripheral hydrogen atoms with chlorine atoms. CuPcCl$_{16}$ is known as one of the most intense molecules against electron beam irradiation among organic molecules, and its critical electron dose is about 30 C/cm^2, while since the critical electron dose of CuPc is about 1 C/cm^2, one should pay attention to the electron irradiation damage of the sample. Spectra shown in Fig. 6(a) were measured with a probe current of 0.05 pA and 1 pA for CuPc and CuPcCl$_{16}$, respectively. Spectrum image data were acquired below the critical electron dose of each molecule, and then the spatial information was averaged to improve the signal-to-noise ratio of spectra. The fine structures in both spectra show clear differences within 4 eV from the threshold; peaks (A) and (B) appear in both spectra, but in the ELNES of CuPcCl$_{16}$, an extra peak (C) is observed around 287 eV. These peaks are attributed to the 1s → π^* transitions, and the final state may be the lowest unoccupied molecular orbital (LUMO). There are three independent carbon atoms with different bonding in each molecule. As shown in Fig. 3(b), it can be classified into

Fig. 5 Distributions of applied electric field calculated by DDELS
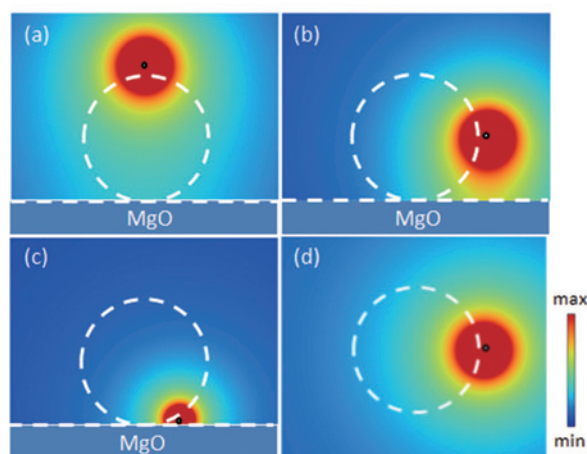
(a) to (c) MgO substrate is included. (d) Isolated silver NP.

Fig. 6 Carbon K-edge ELNES of copper-phthalocyanine and its chlorinated thin films (a) and molecular structure model (b)

X = H ; CuPc
X = Cl ; CuPcCl$_{16}$
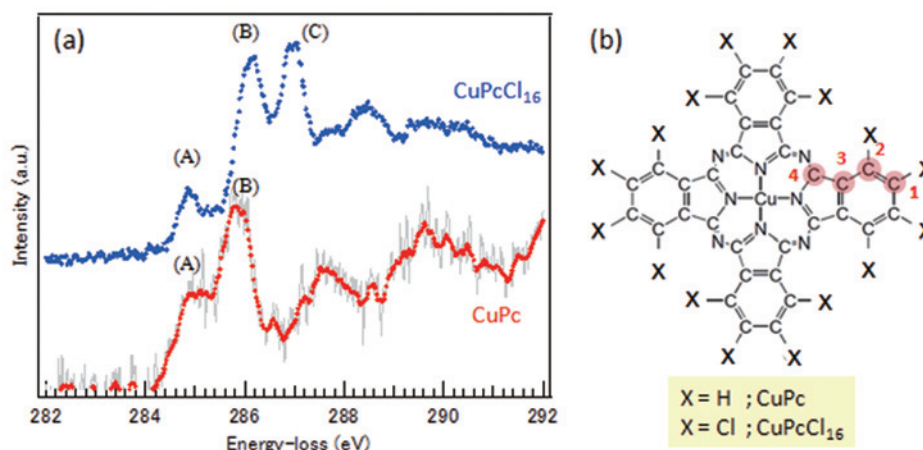
the C1 and C2 atoms bonded to peripheral atoms (hydrogen or chlorine) and a carbon atom, the C3 atoms bonded to three carbon atoms, and C4 atom bonded to two nitrogen atoms and a carbon atom. It has been observed from XPS measurement of CuPc molecule that the 1s level of these carbon atoms has a slight different binding energy [14]. Such chemical shifts of 1s level lead to the different $\pi*$ peak energy in the ELNES. In the case of CuPc molecule, the binding energies of 1s level at C1, C2 and C3 sites are almost same, while that at C4 site is large. This is because the electronegativity of the nitrogen bonded to the C4 site is large, and the valence electron density on the C4 site becomes lower than that at the other carbon sites, so the Coulomb repulsion energy between the valence electron and the 1s electron decreases. Therefore, the peak (A) in the ELNES of CuPc is due to the excitation of C1, C2 and C3 sites, while the peak (B) corresponds to that of the C4 site [15]. In the case of $CuPcCl_{16}$, since the electronegativity of the chlorine bonded to the C1 and C2 sites is larger than that of nitrogen, the 1s level of C1 and C2 sites is stabilized more than that of C4 site. Therefore, the extra peak (C) in the ELNES of $CuPcCl_{16}$ can be attributed to the $\pi*$-resonance excited at C1 and C2 sites. In order to make a quantitative interpretation of these ELNESs including the relative intensity of each peak, it is necessary to calculate spectrum taking into account the effect of the core hole on the independent carbon sites. As shown in the above example, the improvement of energy resolution appears effectively in the fine structures just above the threshold. Although the separation between the peaks (B) and (C) of $CuPcCl_{16}$ is narrow, 0.7 eV, it has been clearly observed. This suggests that the chemical shifts of inner-shell level can be detected in ELNES. It is expected that the analysis of functional groups bonded to organic molecules becomes possible by taking advantage of the features of such high resolution carbon K-edge ELNES.

Finally, the result of vibrational spectrum is shown briefly. Excitations of various vibrational modes are observed in the infrared absorption spectra of organic molecules, but most of them appear below 200 meV. In the case of CuPc molecule, the C-H stretch vibration mode of benzene ring is excited at around 380 meV. As shown in **Fig. 7**, the broad peak assigned to the C-H vibration is observed, but its intensity is considerably weak compared to the optical phonon peak measured from h-BN. Although this spectrum was measured with an irradiation dose of 0.5 C/cm² which was smaller than the critical dose of this molecule, the effect of electron irradiation may not be neglected. Actually, when the spectrum was measured at 1.25 C/cm² slightly above the critical dose, the C-H vibrational peak disappeared, which suggests that the dissociation of hydrogen atoms contributes greatly in the early stage of irradiation damage. This is also confirmed from the fact that the intensity of peak (A) in the ELNES of CuPc decreased with the increasing irradiation dose, indicating the change of bonding state of C1 and C2 sites by the dissociation of hydrogen atoms.

Summary

The monochromated STEM-EELS is a powerful tool to investigate the properties of surface plasmons and vibrational excitation appearing in visible to near infrared region with high spatial resolution. It was also demonstrated that when the low dose measurement is applied to organic crystals, the carbon K-edge ELNES with high energy resolution provides useful information for molecular analysis.
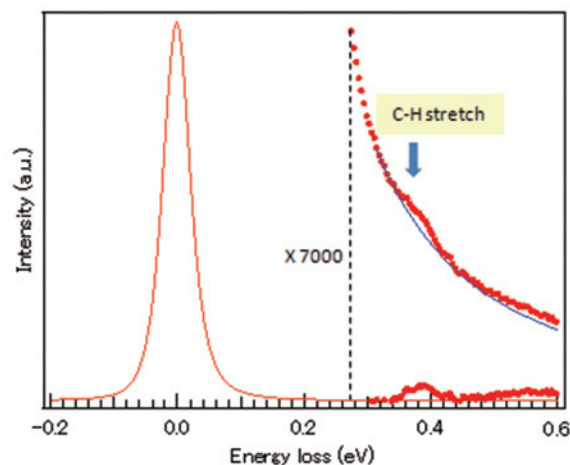
Acknowledgments

Fig. 7 **Vibrational EEL spectrum measured from copper-phthalocyanine thin film**

References

[1] M. Mukai, E. Okunishi, M. Ashino, K. Omoto, T. Fukuda, A. Ikeda, K. Somehara, T. Kaneyama, T. Saitoh, T. Hirayama, Y. Ikuhara, *Microscopy*, **64**, 151 (2015).

[2] T. Miyata, M. Fukuyama, A. Hibata, E. Okunishi, M. Mukai, T. Mizoguchi, *Microscopy* **63**, 377 (2014).

[3] O. L. Krivanek, T. C. Lovejoy, N. Dellby, T. Aoki, R. W. Carpenter, P. Rez, E. Soignard, J. Zhu, P. E. Batson, M. J. Lagos, R. F. Egerton, P. A. Crozier, *Nature*, **514**, 209 (2014).

[4] C. Colliex, M. Kociak, O. Stéphan, *Ultramicroscopy* **162**, A1 (2016).

[5] Y. Fujiyoshi, T. Nemoto, H. Kurata, *Ultramicroscopy* **175**, 116 (2017).

[6] N. Geuquet, L. Henrard, *Ultramicroscopy* **110**, 1075 (2010).

[7] E. D. Palik, Handbook of Optical Constants of Solids 1, Academic Press, New York, (1985).

[8] E. D. Palik, Handbook of Optical Constants of Solids 2, Academic Press, New York, (1991).

[9] M. W. Knight, Y. Wu, J. B. Lassiter, P. Nordlander, N. J. Halas, *Nano Lett*. **9**, 2188 (2009).

[10] M. O. Krause, J. H. Oliver, *J. Phys. Chem. Ref. Data* **8**, 329 (1979).

[11] R. F. Egerton, *Ultramicroscopy* **107**, 575 (2007).

[12] C. Mitterbauera, G. Kothleitnera, W. Groggera, H. Zandbergenb, B. Freitagc, P. Tiemeijerc, F. Hofer, *Ultramicroscopy* **96**, 469 (2003).

[13] H. Kurata, Y. Fujiyoshi, Y. Tomisaki, T. Nemoto, M. Haruta, The 16th EMC Proc., Lyon, France, 863 (2016).

[14] F. Evangelista, V. Carravetta, G. Stefani, B. Jansik, M. Alagia, S. Stranges, A. Ruocco, *J. Chem. Phys*. **126**, 124709 (2007).

[15] R. De Francesco, M. Stener, G. Fronzoni, *J. Phys. Chem.* **A116,** 2885 (2012).

Chemical State Analyses by Soft X-ray Emission Spectroscopy

Masami Terauchi and Yohei Sato

Center for Advanced Microscopy and Spectroscopy, Institute of Multidisciplinary Research for Advanced Materials, Tohoku University

A metallization of Si-sp^3 network of Na_8Si_{46} and a chemical state distribution in Na-doped CaB_6, were observed by using a commercial EPMA-SXES instrument. Information observed in L-emission of $3d$ transition metal elements obtained by an original SEM-SXES instrument is discussed.

Introduction

For developing functional nano-scale materials and nano-scale devices, microscopic analysis and its feedback to manufacturing process is a key issue for those developments. For that purpose, analysis methods based on electron microscopy are crucial. Especially, spectroscopy methods give us fruitful information related to material's functions. X-ray spectroscopy for elemental analysis may be the most widely used one. There are two types of energy-dispersive spectroscopy (EDS) and wavelength-dispersive spectroscopy (WDS). Electron energy-loss spectroscopy (EELS) and cathodoluminescence (CL, related to transition **a** in **Fig. 1**) are also widely used. Recently, a new face of soft X-ray emission spectroscopy (SXES), which can give electronic structure information, comes into a group of commercial methods [1, 2].

For investigating electronic structures related to material's functions, EELS based on transmission electron microscopy (TEM) is widely used because of its better energy resolution than those of EDS and WDS and a wide energy range of 1-1000 eV. EELS can examine a dielectric property from a valence electron excitation spectrum (excitation **b** in Fig. 1). Especially, recent commercialization of a monochromator instrument realized one nanometer probe with an energy resolution of 0.1 eV or better. It enables us to analyze near-infrared property of industrial nano-particles [3] and also thermal lattice-vibrations [4]. Analysis of inner-shell excitation spectrum (excitation **c** in Fig. 1) combined with theoretical simulations becomes familiar for evaluating a relation between an electronic structure and a local crystal structure. Although EELS gives many information on electronic structure from a nm-scale specimen area, it cannot gives information of bonding electrons (valence bands). It can be realized by SXES, which analyzes X-ray emission energies of electronic transitions **d** in Fig. 1 with an energy-resolution better than 1 eV. SXES instruments for electron microscopy had been developed for TEM [5]. Because of a low detection efficiency of the method, it was commercialized as an instrument for electron probe microanalyzer (EPMA) and scanning electron microscope (SEM) which can use a larger probe current than that of TEM.

As X-ray emissions for elemental analysis (EDS, WDS) are dominantly due to electronic transitions between inner-shell levels (transition **e** in Fig. 1), those spectra do not include information on valence electrons.

A SXES instrument was first developed for a TEM [6]. The main bottle neck for application was a low detection efficiency. In high spacial resolution analysis of thin specimen by TEM,

Fig. 1
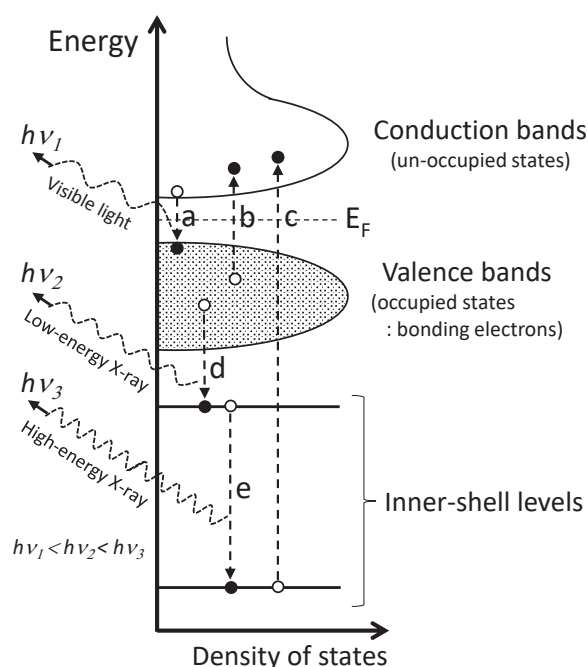
Schematic diagram of electronic transitions related to cathodoluminescence (a), valence electron excitation of EELS (b), inner-shell excitation spectrum of EELS (c), X-ray emission including valence electron information (d) and X-ray emission mainly used for elemental analysis (e).

〉〉 2-1-1 Katahira, Aoba-ku, Sendai 980-8577, Japan. ｜ Email: terauchi@m.tohoku.ac.jp

a specimen volume examined is small and an acquisition time of some tens of minutes or more is necessary for obtaining a reasonable signal to noise ratio. When applying this method to EPMA and SEM, an acquisition time of one or a few minutes is usual due to a larger beam current and a larger examination volume. This SXES method may be useful as a spectroscopy method for bulk materials as TEM-EELS method for thin specimens. Then, this EPMA/SEM-SXES can make a quick feedback to material processing.

When combining an inner-shell excitation EELS spectrum (probing unoccupied states) and a soft X-ray emission spectrum (probing occupied states), a whole electronic states can be figured out. Furthermore, an electronic excitation spectrum can be derived from a valence electron excitation EELS spectrum by using Kramers-Kronig analysis. Therefore, electron microscopy can analyze not only crystal structure and constituent elements but also a whole electronic structure of identified small specimen areas [5, 7].

In this manuscript, SXES observations on a metallization of Si-sp^3 network of Na_8Si_{46}, a chemical state distribution in Na-doped CaB_6, and information on L-emission of $3d$ transition metal elements are described.
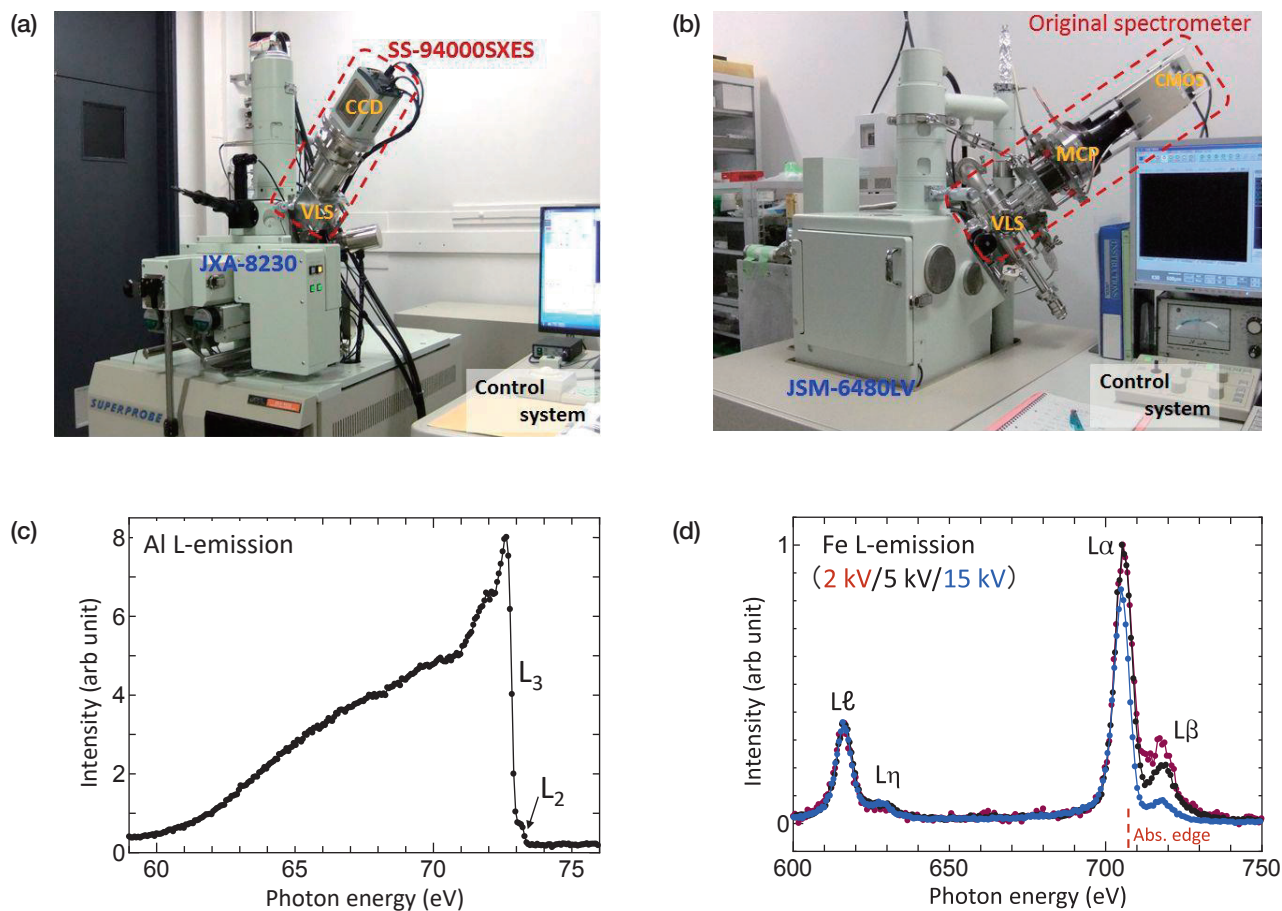
Instruments and experimental condition

SXES instruments used in this report are shown in **Fig. 2**(a) EPMA (JEOL JXA-8230) attached with a commercial SXES spectrometer system (SS-94000SXES) and (b) SEM (JEOL JSM-6480LV) attached with our original spectrometer. Both SXES instruments are WDS type spectrometers based on flat-field grazing incidence optics by using aberration corrected gratings.

The commercial SXES instrument with two gratings can detect from 50 eV to 210 eV for 1st order spectrum, up to 420 eV for 2nd order spectrum, and much further for higher order spectrum. Actually, this spectrometer can detect soft X-ray emission signals of more than 70 elements [8]. Present data was measured by using a grating of JS200N with an averaged groove density of 1200 lines/mm. Detector is a back-thin type CCD. Energy resolution evaluated for a sharp Fermi edge structure observed for Al L-emission at 72 eV was about 0.2 eV. This high energy resolution enables us to conduct a mapping of chemical bonding states.

The original SXES spectrometer of Fig. 2(b) performs a wide energy range of 50-3800 eV for 1st order spectrum by using four gratings. In this report, a grating of JS2000 with an averaged groove density of 2400 lines/mm was used. A

Fig. 2

(a) SS-94000SXES, CCD, VLS, JXA-8230, Control system, SUPERPROBE

(b) Original spectrometer, CMOS, MCP, VLS, JSM-6480LV, Control system

(c) Al L-emission — L$_3$, L$_2$ — Intensity (arb unit) vs Photon energy (eV)

(d) Fe L-emission (2 kV/5 kV/15 kV) — Lℓ, Lη, Lα, Lβ, Abs. edge — Intensity (arb unit) vs Photon energy (eV)

SXES instruments used in this report. (a) EPMA (JEOL JXA-8230) attached with a commercial SXES spectrometer system (SS-94000SXES) and (b) SEM (JEOL JSM-6480LV) attached with our original spectrometer. (c) Al L-emission spectrum obtained by (a). A fine structure due to a spin-orbit splitting of L$_3$ and L$_2$ levels of 0.4 eV is seen. (d) Fe L-emission spectra obtained by our original spectrometer (b) at accelerating voltages of 2, 5 and 10 kV. Spectrum intensities were normalized by Lℓ emission.

multi-channel plate detector optically coupled with a CMOS camera was used as a detector. This instrument performs an energy resolution of 0.08 eV in photon counting mode for Al L-emission [9].

SXES measurements were done at an accelerating voltage of 5 kV. Figure 2(c) shows Al L-emission spectrum, which originates electronic transitions from valence bands to the inner L-shell levels, obtained by the commercial spectrometer. The spectrum shows a sharp Fermi edge structure at 72 eV expected for aluminum, even though the specimen surface is oxidized. A fine structure due to a spin-orbit splitting of L_3 and L_2 levels of 0.4 eV is clearly seen. Electrons of 5 keV impinged on aluminum surface spread out inside the material via inelastic scattering of about 0.32 μm in diameter, which was evaluated by Reed's equation of $d = 0.077 (Eo^{1.5} - Ec^{1.5})/\rho$ (d : size of spreading (μm), Eo : incident energy (keV), Ec : critical excitation energy for a desired X-ray (keV), ρ : mass density of material (g/cm³)) [10]. As a thickness of surface oxidized layer is less than 10 nm, the spectrum of Fig. 2(c) is reasonably assigned to a pure aluminum. Emission intensity of the surface oxidized layer becomes apparent for an accelerating voltage lower than 1 kV. Figure 2(d) shows Fe L-emission spectra obtained by our original spectrometer (Fig. 2(b)) at accelerating voltages of 2, 5 and 10 kV. Spectrum intensities were normalized by Lℓ emission intensity, which suffers little absorption effect. It is apparently seen that the intensity distribution of Lα,β emission depends on accelerating voltage. For a higher accelerating voltage, incident electrons reach in a deeper region from the specimen surface and generate X-ray emissions, which suffer a larger absorption before going out from the surface. In Fe L-emission energy region, there is L absorption edge at 707 eV (red dotted line) between Lα and Lβ emission. This is the cause of a much intensity decrease of Lβ intensity for a larger accelerating voltage. The absorption effect is smaller for a lower accelerating voltage, but an effect of surface oxidized layer becomes apparent. By using the Reed's equation, spreads of electron beams in Fe at accelerating voltages of 15 kV, 5 kV and 2 kV are evaluated to be 0.56 μm, 0.10 μm and 0.02 μm, respectively. Based on the above experimental results and experiences, an accelerating voltage of 5 kV was adopted as an experimental condition of surface insensitive and less absorption effect. Spectroscopy method at a low accelerating voltage is useful for easily damaged materials. Recently, amorphous carbon nitride films were successfully analyzed by using SXES at 5 kV [11].

Metallization of Si sp^3 network in Na_8Si_{46}

Figure 3(a) shows a crystal structure of Type-I Na-Si clathrate of Na_8Si_{46}. This material based on a three dimensional Si-sp^3 covalent bonding network, which corresponds to a replacement of hydrogen bonds in gas hydrates by Si-Si covalent bonding. This Si-sp^3 bonding network includes Si_{20} (dodecahedron) and Si_{24} (tetra-kaidecahedron) cages. Na atoms locate in those cages. Si-sp^3 bonding network has a semiconductor character. However, Na atoms in the cages transfer it's valence electron to the Si network resulting in a metal character of Na_8Si_{46} [12]. Figure 3(b) shows a SEM image of a bulk crystal used. Si L-emission spectrum obtained from a circled area in (b) by using the instrument of Fig. 2(a) is shown in (c). A Si L-emission spectrum of Si wafer (semiconductor)

Fig. 3
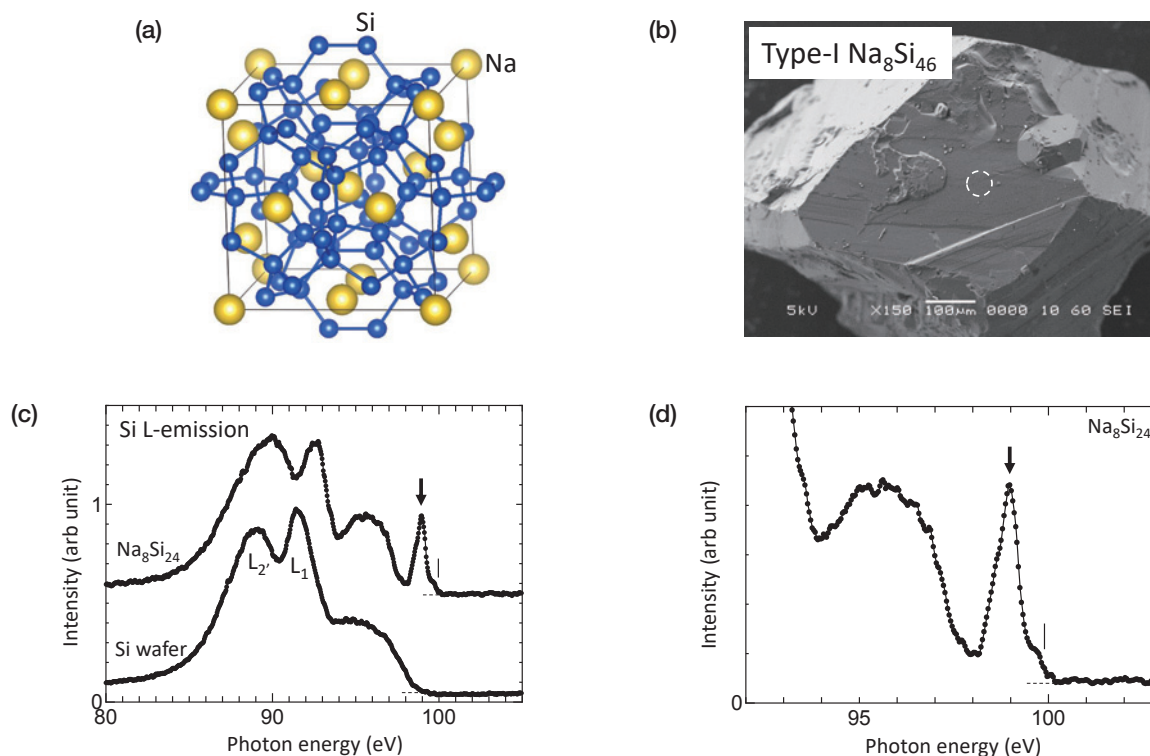
(a) Crystal structure of Type-I Na-Si clathrate of Na_8Si_{46}. (b) SEM image of a bulk crystal used. (c) Si L-emission spectrum obtained from a circled area in (b). (d) Magnified spectrum of Na_8Si_{46} corresponds to the top of the valence bands. A sharp intensity drop with a width of 0.2-0.3 eV, indicated by a vertical line, corresponds to a Fermi edge structure.

is also shown for comparison. Those intensity distributions are due to transitions from valence bands to inner Si-L$_{2,3}$ levels with p symmetry. Due to a dipole selection rule, those intensity distributions reflect density of states of valence band with s and d symmetries. Labels L$_{2'}$ and L$_1$ written in the spectrum of Si wafer indicate special points in the band diagram of cubic Si crystal. This two peak structure seems to be common for the two materials. It may originate from Si-sp^3 bonding network for the both materials. Contrary to this similarity, the right hand side end, where corresponds to the top of the valence band, is different each other. Na$_8$Si$_{46}$ shows a sharp peak. From a comparison with a theoretical calculation, this sharp peak may be assigned to a bonding state between Si cage and Na atoms [13]. For clarifying the difference more clearly, the spectrum of Na$_8$Si$_{46}$ is magnified in Fig. 3(d). At the right-hand side end of the spectrum, a sharp intensity drop with a width of 0.2-0.3 eV is seen as indicated by a vertical line. As the width is comparable to the energy resolution of the measurement, this sharp intensity change can be assigned to a Fermi edge structure, which apparently shows this material is a metal.

Chemical state mapping of Na-doped CaB$_6$

The crystal structure of CaB$_6$ is composed of a network of B$_6$ octagonal clusters, which locate at each corner of a cubic unit cell, and a metal atom at the body-center positon of the cell (**Fig. 4**(a)). Ca atom can transfer two valence electrons to the B$_6$ cluster network. Since B$_6$ cluster network can accept two electrons in valence bands, CaB$_6$ becomes a semiconductor (*n*-type). For realizing a thermo-electric device using B$_6$ cluster network materials [14], *p*-type semiconductor is necessary. As Na atom has only one valence electron, Na substitution to Ca site is a hole doping to B$_6$ cluster network causing a *p*-type semiconductor [15]. From an EDS evaluation, Na content of the material was a few percent. However, the uniformity of the material has not been evaluated. Then, a piece of Na-doped CaB$_6$ material was examined by using a commercial SXES-EPMA instrument of Fig. 2(a).

Figure 4(b) and (c) show a secondary electron (SE) image and a back-scattered electron (BSE) image of an area of Na-

Fig. 4

(a) CaB$_6$

(b) SE image

(c) BSE image

(d) Ca-Lℓ,η (150-154eV)

(e) B-K (170-188eV)
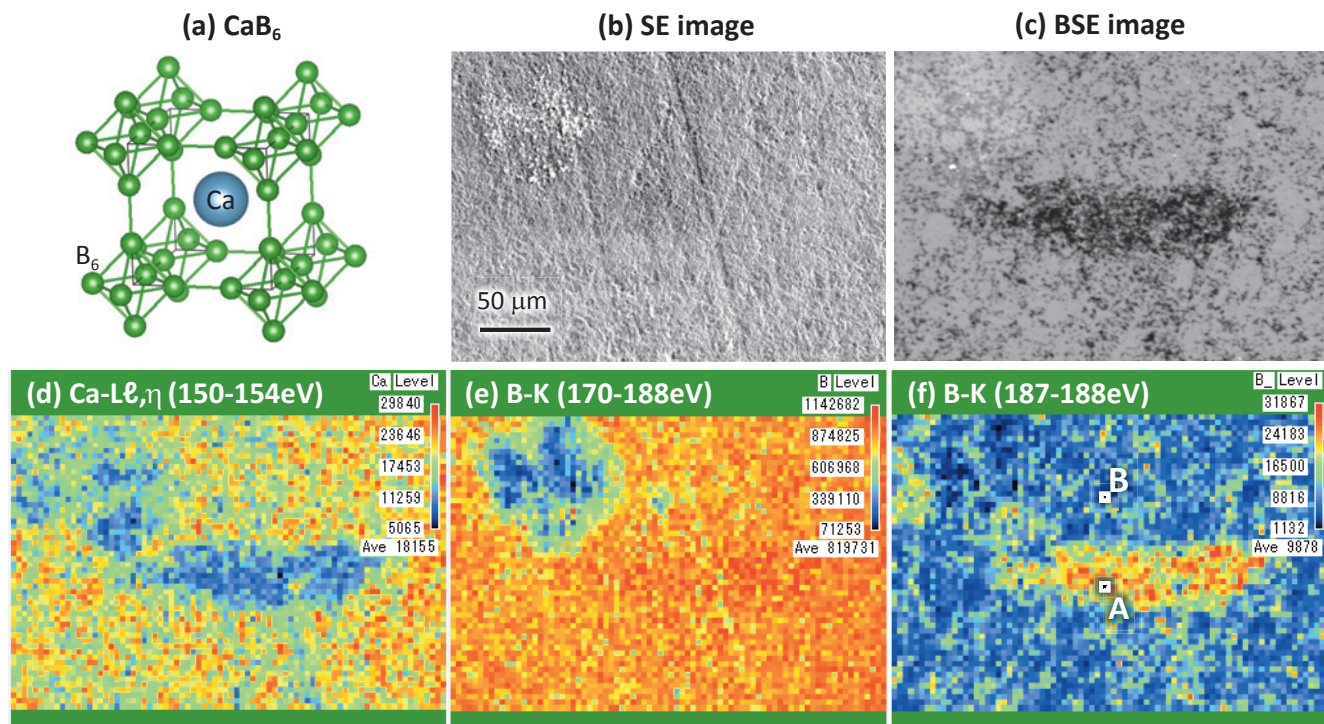
(f) B-K (187-188eV)

(a) Crystal structure of CaB$_6$. (b) Secondary electron (SE) image and (c) back-scattered electron (BSE) image of Na-doped CaB$_6$. Spectral intensity maps of (d) Ca-Lℓ,η intensity (150-154 eV), (e) B-K intensity (170-188 eV), and (f) the top part of the B-K intensity (187-188 eV).

Fig. 5
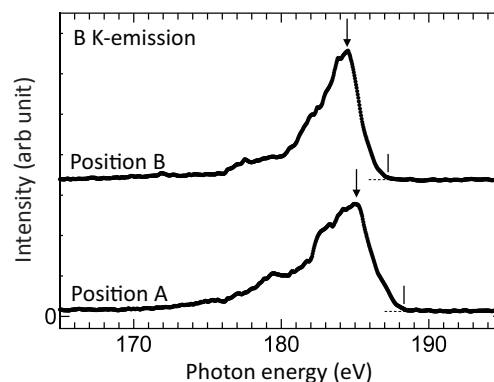
B-K emissions spectra of the points of A and B shown in Fig. 4(f).

doped CaB_6, respectively. The SE image shows a little different surface morphology in the upper left area, where the carbon signal was detected. The BSE image shows a lower intensity region in the center. Then, SXES mapping measurement was conducted. Spectral intensity maps of Ca-Lℓ,η intensity (150-154 eV), B-K intensity (170-188 eV), and the top part of the B-K intensity (187-188 eV) are shown in Fig. 4(d), (e) and (f), respectively. Ca-Lℓ,η emission map shows a low intensity for the dark area of the BSE image. It means a low Ca content for the area. B-K emission map does not show an apparent intensity change for the area. On the other hand, the map of the top part of the B-K emission intensity in Fig. 4(f) shows a larger intensity for the area. For investigating the origin of this intensity increase, B-K emissions spectra of the points of A and B shown in the figure are presented in **Fig. 5**. The spectra show a little difference in those intensity distributions, suggesting some difference of bonding state of B_6-cluster network. It should be noticed that the peak of spectrum A indicated by an arrow locates in higher energy side by about 0.7 eV compared to that of spectrum B. This shift of the spectrum A should be a chemical shift originated from an energy shift of B 1s level to a larger binding energy side. This core-level shift can be due to a decrease of valence charge of B atoms. It is expected for Na-doped CaB_6. Unfortunately, present system cannot detect Na-K emission intensity (coming up soon as a commercial version). Impurity oxygen can be also an origin because O atoms adopt electrons. Actually, a tiny intensity at 175 eV in the spectrum A can be assigned to the 3rd order intensity of O-K emission. In anyway, a high energy resolution soft X-ray mapping can give us a chemical shift mapping reflecting an amount of valence charge.

Information on L-emission of 3d transition metal elements

Bonding state and valency of 3d transition metal (3d-TM) elements is a key for evaluating positive electrode materials of Li-ion battery, because a change of valency of 3d-TM elements is an origin of charge and discharge of the battery. Information on valence electrons of 4s and 3d of 3d-TM elements is included in L-emissions of the elements. As those energies of 1st order spectra are out of the energy range of the commercial SXES spectrometer, the original spectrometer (Fig. 2(b)) was applied to evaluate L-emission spectra of Ti and its oxides [16], and Fe and its oxides. There are four types of L-emissions of Lα, Lβ, Lℓ and Lη. Lα and Lβ emissions are due to transitions of valence electrons to inner L_3-shell and L_2-shell, respectively. Thus, those intensities include information on energy states of 3d electrons. On the other hand, Lℓ and Lη emissions are due to transitions from a shallow inner-shell level M_1 to the deeper L_3 and L_2 levels, respectively. Thus, information included in Lℓ,η is different from that of Lα,β. **Figure 6** shows a schematic diagram of those transitions. Transitions from $M_{2,3}$ to $L_{2,3}$ are forbidden by dipole selection rule.

Figure 7 shows (a) Lα,β emission and (b) Lℓ,η emission spectra of metal-Ti, a recently reported mono-oxide ε-TiO
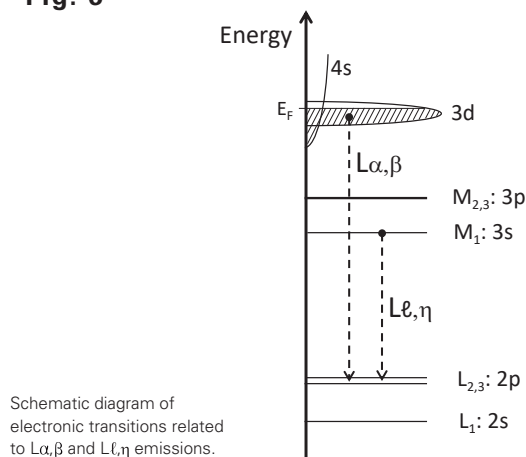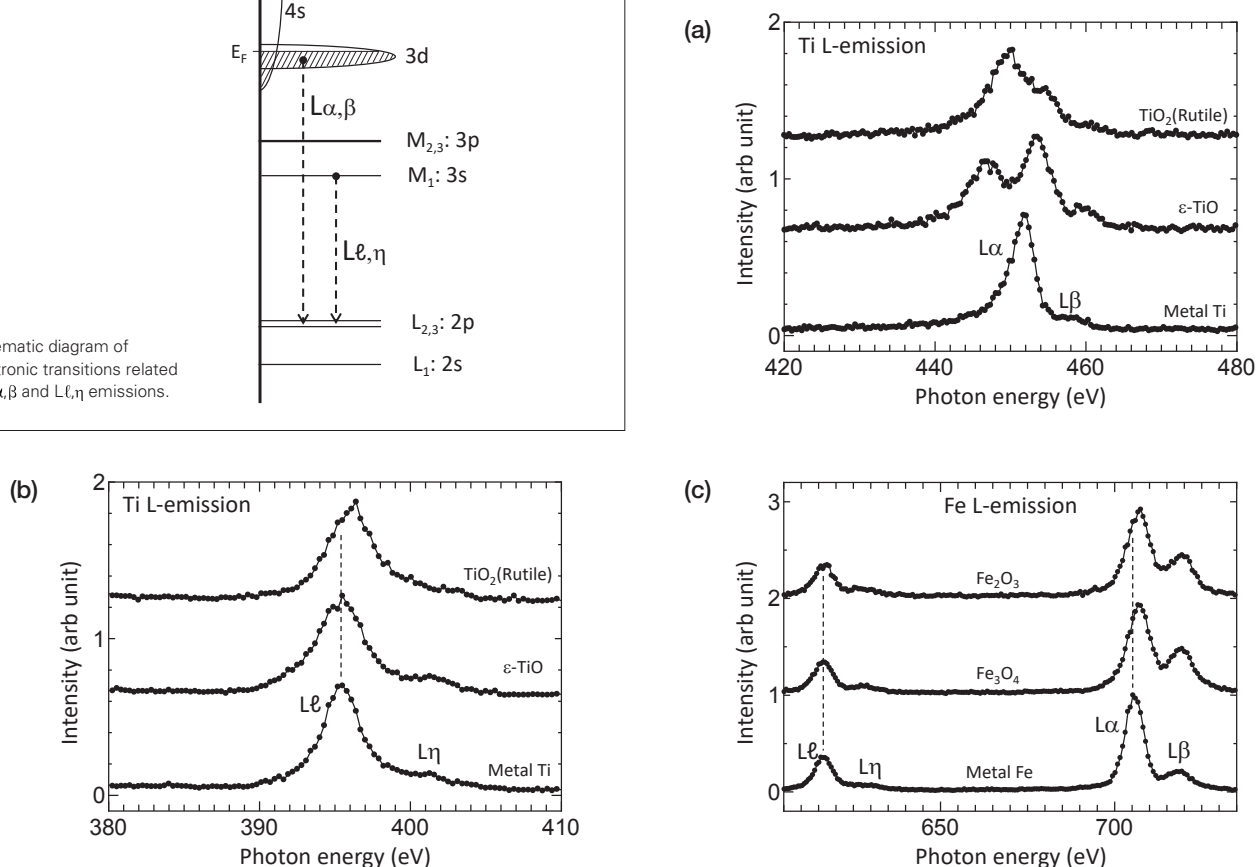
Fig. 6

Schematic diagram of electronic transitions related to Lα,β and Lℓ,η emissions.

Fig. 7

(a) Lα,β emission and (b) Lℓ,η emission spectra of metal-Ti, a recently reported ε-TiO and TiO_2 (rutile). (c) Fe L-emission spectra of metal-Fe and its oxides.

and TiO_2 (rutile). It is clearly seen that intensity distributions of $L\alpha,\beta$ emissions are different for different materials. Those reflect that energy states of bonding electrons are different for different atomic arrangements or crystal structures. In a simple ionic model, TiO_2 is considered as $Ti^{4+}O^{-2}_2$ and cannot emit $L\alpha,\beta$ intensity because a Ti^{4+} ion has no $3d$ electron. Since $L\alpha,\beta$ emissions are observed in experiment, Ti atom in TiO_2 is not a pure Ti^{4+} ion via covalent bonding between Ti and surrounding O atoms. For discussing intensity distributions of $L\alpha,\beta$ emissions, not only the density of state of valence bands but also energy shift of inner shell level (chemical shift) has to be considered. Furthermore, overlapping of $L\alpha$ and $L\beta$ intensity distributions and a presence of an absorption edge between $L\alpha$ and $L\beta$ has to be taken into account. On the other hand, intensity distribution of $L\ell,\eta$ due to transitions between two inner-shell levels is much easier to discuss.

$L\alpha$ peak energy of TiO_2 is about 2 eV smaller than that of metal-Ti. In turn, $L\ell$ peak energy of TiO_2 is 0.7 eV larger than that of metal-Ti. $L\ell$ position of ε-TiO is almost the same with that of metal-Ti. In case of Fe and its oxides shown in Fig. 7(c), $L\ell$ of metal-Fe and Fe_3O_4 is almost the same energy positon. $L\ell$ of Fe_2O_3 positons a little higher energy side of about 0.2 eV than others. Those suggest that the origin of the energy shifts of $L\alpha$ and $L\ell$ is not simple. A larger intensity ratio of $L\beta/L\alpha$ in Fe oxides can be due to a suppression of Coster-Kronig process in oxides [18].

Based on a discussion on a binding energy shift due to a change of chemical effects in X-ray photoelectron spectroscopy, information included in $L\alpha$ and $L\ell$ emission intensity is concluded as follows [16]. A change of $L\alpha$ emission intensity distribution reflects changes of a valence charge and solid state effects (crystal-field, density of states, bandgap and etc.). A change of $L\ell$ peak position is caused by a change of a M_1 core-hole effect in the final state, which reflects a local screening effect. WIEN2k code was used to evaluate a difference of core-hole effect in metal and its oxides. The values of TiO_2 compared with metal-Ti and of Fe_2O_3 compared with metal-Fe were +0.7 eV and +0.2 eV, respectively. Those values well reproduce the experimentally observed values. This peak shifts due to core-hole effect are closely related to dielectric property, band-gap energy of a material examined [19, 20].

Conclusion

Recently commercialized SXES instrument for EPMA and SEM has an energy resolution of 0.2 eV for Al-L-emission, which is about 10-100 times better than WDS and EDS. This SXES method is useful as a spectroscopy method for chemical state analyses and those mapping of bulk materials as TEM-EELS method for thin specimens. As there is no need for thin specimen preparation, this EPMA/SEM-SXES can make a quick feedback to material production processes. This instrument provides a bonding electron spectroscopy method not only for a wide variety of new functional materials developments but also for basic research of compounds.

Acknowledgments

References

[1] H. Takahashi, T. Murano, M. Takakura, N. Handa, M. Terauchi, M. Koike, T. Kawachi, T. Imazono, N. Hasegawa, M. Koeda, T. Nagano, H. Sasai, Y. Oue, Z. Yonezawa and S. Kuramoto, *JEOL News*, **49**, 73 (2014).

[2] H. Takahashi, T. Murano, M. Takakura, S. Asahina, M. Terauchi, M. Koike, T. Imazono, M. Koeda and T. Nagano, *IOP Conf. Series: Materials Science and Engineering*, **109**, 012017 (2016).

[3] Y. Sato, M. Terauchi and K. Adachi, *Journal of Applied Physics*, **112**, 074308 (2012).

[4] O.L. Krivanek, T.C. Lovejoy, N. Dellby, T. Aoki, R. W. Carpenter, P. Rez, E. Soignard, J. Zhu, P. E. Batson, M. J. Lagos, R. F. Egerton and P. A. Crozier, *Nature*, **514**, 209 (2014).

[5] M. Terauchi, chapter 7 in *Transmission Electron Microscopy Characterization of Nanomaterials*, ed. Kumar C S S R (Springer-Verlag), 287 (2014).

[6] M. Terauchi, H. Yamamoto and M. Tanaka, *Journal of Electron Microscopy*, **50**, 101 (2001).

[7] M. Terauchi and M. Kawana, *Ultramicroscopy*, **106**, 1069 (2006).

[8] M. Terauchi, H. Takahashi, M. Takakura and T. Murano, *Handbook of Soft X-ray Emission Spectra ver.3* (IMRAM Tohoku Univ. & JEOL), (2016).

[9] M. Terauchi, H. Takahashi, M. Takakura, T. Murano, M. Koike, T. Imazono, T. Nagano, H. Sasai and M. Koeda, *Microscopy and Microanalysis*, **22(Suppl 3)**, 414 (2016).

[10] S. J. B. Reed, *Electron Microprobe Analysis 2nd edition* (Cambridge Univ. Press.), 200 (1993).

[11] S. Ishii, M. Terauchi, Y. Sato, N. Tamura, M. Aono and H. Abe, *accepted for Microscopy* (2018).

[12] A. Moewes, E. Z. Kurumaev, J. S. Tse, M. Geshi, M. J. Ferguson, V. A. Trofimova and Y.M. Yarmoshenko, *Phys. Rev. B*, **65**, 153106 (2002).

[13] Z. Wei, C. Quing-Yun, Z. Zhao-Yi and C. Ling-Cang, *Chin. Phys. B*, **24**, 107101 (2015).

[14] M. Takeda, M. Terui, N. Takahashi and N. Ueda, *J. Solid State Chemistry*, **179**, 2823 (2006).

[15] H. Kuribayashi, S. Makino and M. Takeda, *Abstract of ISBB-18*, 148 (2014).

[16] M. Terauchi, S. Koshiya and K. Kimoto, *IOP Conf. Series: Materials Science and Engineering*, **304**, 012018 (2017).

[17] S. Amano, D. Bogdanovski, H. Yamane, M. Terauchi and R. Dronskowski, *Angewandte Chemie*, **55**, 1652 (2016).

[18] E. Antonides and G.A. Sawatzky, *J. Phys. C: Solid State Phys.*, **9**, L547 (1976).

[19] K. Hirose, M. Kihara, H. Okamoto, S. Shinagawa, H. Nohira, E. Ikenaga, M. Higuchi, A. Teramoto, S. Sugawa, T. Ohmi and T. Hattori, *Applied Physics Letters*, **89**, 154103 (2006).

[20] K. Hirose, H. Suzuki, H. Nohira, E. Ikenaga, D. Kobayashi and T. Hattori, *J. Physics: Conference Series*, **100**, 01211 (2008).

X-ray, Electron and NMR Crystallography to Structural Determination of Small Organic Molecules

Yusuke Nishiyama   [1] JEOL RESONANCE Inc. [2] RIKEN CLST-JEOL Collaboration Center

Here we present the recent development at RIKEN CLST-JEOL collaboration laboratory to explore the molecular structures of low-molecular weight pharmaceutical compounds in natural abundance (without any isotopic labeling); the recent progress in fast magic angle spinning (MAS) technology in solid-state nuclear magnetic resonance (ssNMR) and in ultra high sensitivity camera in transmission electron microscopy (TEM) paves a new way to answer problems in the pharmaceutical industry and sciences. 1) Crystalline polymorphs and 2) salt/cocrystal are two major concerns in terms of quality control, stability, and intellectual property. To identify the crystalline form, powder X-ray diffraction and ^{13}C cross-polarization MAS ssNMR are widely used methods, however, the former is sometimes not suitable for mixture analysis and latter fails to distinguish crystalline forms with similar molecular conformations. To solve these issues, we use electron diffraction (ED) and ^{1}H fast MAS NMR. The crystalline form can be determined from nano- to micro-meter sized single crystals using ED, since electron interactions are 4 to 5 order stronger than X-ray interactions. ^{1}H NMR also gives suitable information to molecular packing since ^{1}H is located at the surface of the crystals. The salt/cocrystal issue, where hydrogen plays a key role, is a serious problem, since single crystal X-ray diffraction (SCXRD) cannot determine the hydrogen atom position precisely. Here we determine the internuclear distances between ^{1}H and ^{15}N using ssNMR at fast MAS conditions, while the global structure is obtained through SCXRD, answering the salt/cocrystal questions.

Introduction

While biotechnology-based medicines are listed at the top shares in pharmaceutical market, the traditional low-molecular weight drugs are still very important for daily treatment, for example adult diseases. These low-molecular weight active pharmaceutical ingredients (APIs) can typically be crystallized in several different forms, i.e. crystalline polymorphs, depending on the crystallization conditions. Since the solubility and stability are largely affected by the crystalline form, it is very important to control and monitor the crystalline form in view point of quality control from development to production stages [1, 2, 3]. When the crystals with large enough size (~100 μm) is available, single crystal X-ray diffraction (SCXRD) gives distinct answer to crystalline forms with atomic resolution. However, most of the low-molecular weight drugs are provided in micro-crystalline forms with various formulation including tablets, pills, powders. As these formulations involve the excipient, it is crucial to determine crystalline form from micro-crystals in mixture. Powder X-ray diffraction (PXRD) and ^{13}C cross-polarization magic angle spinning nuclear magnetic resonance (CPMAS NMR) are two major methods to identify

the crystalline form. As the experimental patterns/spectra gives finger prints of each crystalline form, the comparison of patterns/spectra between drug and standard form gives, in most cases, clear answer to the crystalline from in it. However, both methods still have practical problems. PXRD sometimes fails to identify the crystalline form as many diffraction patters from API and excipient are overlapped to each other. On the other hand, ^{13}C CPMAS which is sensitive to molecular conformation is suitable method for mixture analysis as most signals from excipient appear at the positions different from those from API, avoiding the overlapping of signals. However, ^{13}C CPMAS is rather insensitive to molecular packing as carbon atoms are buried inside the molecules and located far from the molecular surface. Thus, the ^{13}C CPMAS fails to identify the crystalline forms with similar molecular conformations. Moreover, the sensitivity to crystalline form is less than PXRD.

The other major issue in low-molecular weight API is way to identify salt/cocrystal/continuum in multi-component systems. It is sometimes required to improve the solubility and/or stability of API crystals. The multi-component systems composed with API and inert coformer are one of the widely used solutions to this issue. Many examples can be found in multi-component systems

〉〉 [1] Musashino, Akishima, Tokyo 196-8558, Japan, [2] Tsurumi, Yokohama, Kanagawa 230-0045, Japan | Email: yunishiy@jeol.co.jp

by mixing the (typically basic) API and (acidic) coformer. When the difference of pKa (ΔpKa) is larger than 3, this forms salt, where intermolecular ionic interactions are found. In salt, proton from coformer totally moves toward API. Recently, another class of multi-component systems, cocrystal, is introduced when ΔpKa is less than 3. In cocrystal, the proton in coformer still stays there and intermolecular hydrogen bonding is formed. In addition, the system between salt and cocrystal is also found, i.e. continuum where proton is located between API and coformer. It is crucial to identify salt/cocrystal/continuum in terms of intellectual view point, especially when ΔpKa is smaller than 3. However, lack of ability to determine the proton position in XRD based methods brings serious issue to the identification of salt/cocrystal/continuum, since the difference between them comes only from hydrogen positions.

The major issues which are not solved yet are 1) analysis of mixture, 2) identification of crystalline form with similar molecular conformation, and 3) lack of ability to determine the ^{1}H positions. The former two issues are related to crystalline polymorphs and the last one is to salt/cocrystal/continuum. Here, we combine electron diffraction (ED), ^{1}H ssNMR, and SCXRD to tackle with these issues. ED is one of the observation methods in transmission electron microscopy (TEM) equipments and gives diffraction patterns. Since interaction of electron is 10^4 to 10^5 stronger than that of X-ray, ED pattern can be observed from nano- to micro-sized single crystals, enabling mixture analysis. Although the application of ED has largely been limited to inorganic materials which are robust to electron irradiation, recent progress in high-sensitivity camera allows low-dose mode together with cryo sample holder, paving a way to ED

observation of organic crystals including low-molecular weight API. The issue 2) is raised because ^{13}C CPMAS is insensitive to molecular conformation as mentioned above. Fortunately, the introduction of very fast MAS technology > 70 kHz enables the high resolution ^{1}H observation even in rigid solids [4, 5, 6], where [1]Hs are tightly coupled with [1]H-^{1}H dipolar interactions at moderate MAS rate. Since ^{1}H is located at the surface, ^{1}H isotropic chemical shifts are sensitive to not only conformation but also molecular packings. In addition, [1]H-^{1}H intermolecular correlation gives distinct patterns for each molecular packing. The fast MAS technology realizes not only high resolution ^{1}H NMR but also several sophisticated experiments, including ^{14}N NMR and [1]H-^{15}N distance measurements. The former reveals protonated state in small organic molecules. The latter gives clear answer to salt/cocrystal/continuum issue where hydrogen positions play a key role. In addition, we evaluate the throughput of each method.

Crystalline Polymorphs [7]

Identification of crystalline forms in pharmaceutical applications is crucial and usually performed by PXRD and ^{13}C CPMAS ssNMR. However, the former is not suitable for mixture analysis and the latter sometimes fails as discussed above. As an example, ^{13}C CPMAS spectra of three different (pseudo) polymorphs of L-histidine are shown in **Fig. 1**. L-histidine (Fig. 1b, c) gives distinct spectra from its hydrochloride salt of L-histidine·HCl·H$_2$O (Fig. 1a), because of different molecular conformation. On the other hand, L-histidine in orthorhombic (Fig. 1b) and monoclinic (Fig. 1c) form gives almost identical ^{13}C CPMAS spectra, reflecting the close conformation to each

Fig. 1
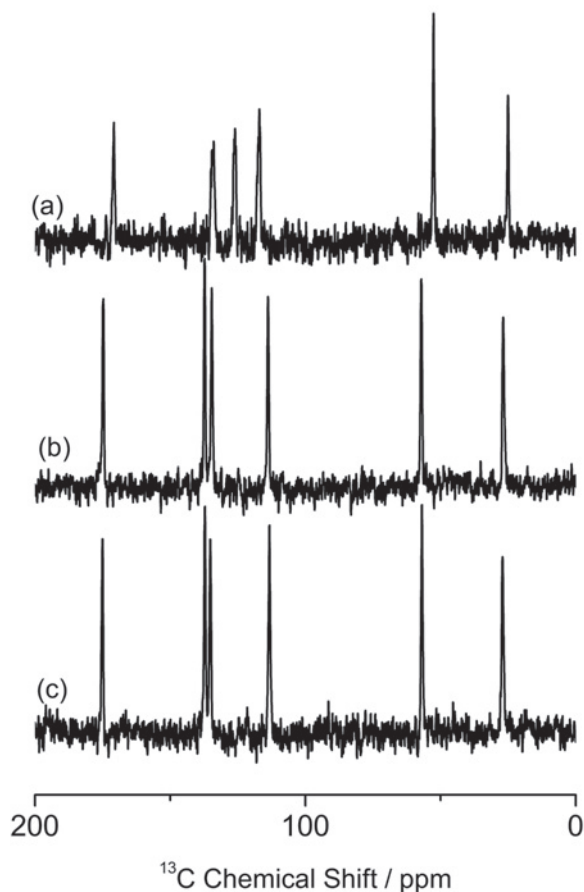
^{13}C CPMAS spectra of (a) L-histidine·HCl·H$_2$O, (b) L-histidine (orthorhombic) and (c) L-histidine (monoclinic), together with the molecular conformations. 256 scans for (a) and 512 scans for (b) and (c) were accumulated. (a) was measured at 16.4 T with a JNM-ECA700II spectrometer (JEOL RESONANCE Inc., Japan). The figure is reproduced from the reference 7.

other. As shown here, ^{13}C CPMAS is sensitive measure to identify crystalline form with different conformation, however, fails to distinguish the polymorphs with similar molecular conformation. We here propose a combined approach of ED and ^{1}H ssNMR at very fast MAS to answer these questions.

Figure 2 shows TEM image and ED pattern of L-histidine·HCl·H$_2$O measured at room temperature. While the size of crystal is about 1 µm, which is typically found in pharmaceutical products, 100 nm nano-beam is applied. Thus, in principle, crystals with 100 nm are large enough to obtain single crystalline ED patterns. In fact, we have measure ED patterns from 100 nm or even smaller crystals. As the critical dose of L-histidine·HCl·H$_2$O at room temperature is only 10-20 e$^-$nm^{-2}, we set the dose rate to 10 e$^-$nm^{-2}s^{-1} with exposure time of 1 s, resulting in a total dose of 10 e$^-$nm^{-2}. Even with such a very low dose conditions, the state-of-the-art CMOS camera (OneView, Gatan, Inc., USA) gives enough sensitivity. While the critical doses of 10-20 e$^-$nm^{-2} are typically found in organic molecules, cryo sample holder improves the critical dose further if needed. As the ED pattern can easily calculated from the crystalline structure, crystalline form can be identified by comparing the experimental and calculated ED patterns. The ED patterns of L-histidine in orthorhombic and monoclinic forms are shown in **Fig. 3** and **Fig. 4**, respectively. While ^{13}C CPMAS fails to distinguish these two forms (Fig. 1), ED diffraction gives distinct patterns for each crystalline form. This is because the lattice parameters are totally different in these two forms. In addition, ED enables high throughput measurements within one minute compared to PXRD (tens of minutes) and ^{13}C CPMAS (hours). The ED measurements were performed using JEM-ARM200F (JEOL Ltd., Japan). Most TEM instruments are capable of this measurement if high sensitivity camera is installed.

The molecular packing can be investigated using ^{1}H NMR at very fast MAS. 1D ^{1}H NMR spectra of L-histidine (pseudo) polymorphs at 70 kHz MAS are shown in **Fig. 5**, giving different patterns. Notably, L-histidine in the orthorhombic form (b) gives different pattern from one in the monoclinic form (c). These differences come from different molecular packings. This highlights the advantage of ^{1}H NMR over the ^{13}C CPMAS which fails to identify these two crystalline forms. Thanks to the high abundance (>99%) and Larmor frequency (600 MHz at 14.1 T), it takes less than one minutes to observe these 1D spectra. The difference between two crystalline forms can be magnified by observing ^{1}H/^{1}H homonuclear correlation experiments, which should be sensitive to intermolecular ^{1}H/^{1}H connectivity, thus crystalline packings. The ability of homonuclear correlation is one of the unique features of ^{1}H NMR with the aid of its high sensitivity and abundance. **Figure 6** gives 2D ^{1}H double-quantum (DQ) / single-quantum (SQ) homonuclear correlation spectra of L-histidine in orthorhombic and monoclinic forms. While 1D spectra only show the local information, 2D homonuclear correlation spectra also reflect the information on molecular packings, as clearly shown in the overlaid spectra. As the DQ coherences are created through ^{1}H-^{1}H dipolar interactions, the cross peak intensities reflect the spatial proximity. For example, the internuclear distances between H1 and H4 is 4.1 Å for the orthorhombic, it is much shorter and 2.86 Å in the monoclinic form. Although the difference in distance is only 1.4 times, this results in 2.9 times stronger dipolar interactions in the monoclinic form. Thus the H1-H4 correlations are only observed in the monoclinic form. It is 2D experiment, however, the measurement time is typically less than one hour, giving higher throughput than ^{13}C CPMAS.
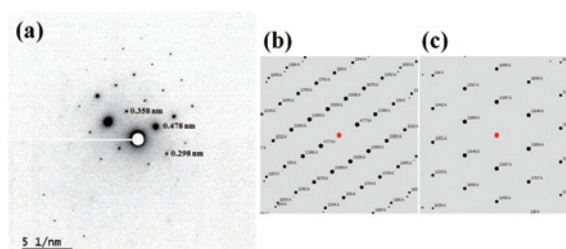
^{1}H/^{14}N correlation NMR also gives fruitful information. There


Fig. 2
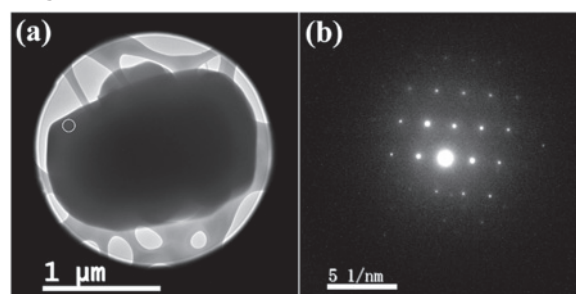
(a) TEM image and (b) nano-beam (100 nm diameter) diffraction pattern of the microcrystalline L-histidine·HCl·H$_2$O sample. The diffraction pattern was obtained from the area indicated by the white circle in (a). The figure is reproduced from the reference 7.


Fig. 3

(a) The negatively displayed experimental ED pattern for L-histidine (orthorhombic) and the calculated ED patterns for (b) L-histidine (orthorhombic) and (c) L-histidine (monoclinic). The d-spacings corresponding to the diffraction spots are estimated by the calibrated camera length of 40 cm and a wavelength of 2.51 pm at 200 kV accelerating voltage. The ED pattern was calculated for a [631] zone axis incidence beam. The figure is reproduced from the reference 7.

Fig. 4
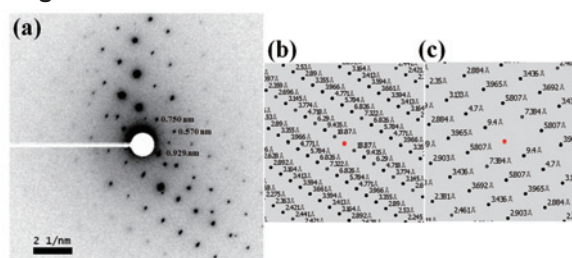
(a) The negatively displayed experimental ED pattern for L-histidine (monoclinic) and the calculated ED patterns for (b) L-histidine (orthorhombic) and (c) L-histidine (monoclinic). The d-spacings corresponding to the diffraction spots are estimated by the calibrated camera length of 40 cm and a wavelength of 2.51 pm at 200 kV accelerating voltage. The ED pattern was calculated for a [100] zone axis incidence beam. The figure is reproduced from the reference 7.

Fig. 5
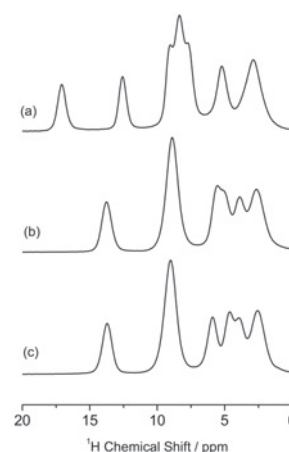
The ^{1}H NMR spectra of (a) L-histidine·HCl·H$_2$O, (b) L-histidine (orthorhombic) and (c) L-histidine (monoclinic). The figure is reproduced from the reference 7.

are multiple possible protonated states in L-histidine. Either or both of the two nitrogens at τ and δ on the imidazole ring could be protonated to NH moiety. In addition, L-histidine can be Zwitterion. It is challenging to distinguish these protonated states by either XRD or ED, since both methods are not sensitive to hydrogen positions. However, $^1H/^{14}N$ correlation spectra of L-histidine (**Fig. 7**) give the clear answer. In the acidic environment in L-histidine·HCl·H$_2$O, three NH correlation appears. This clearly shows both τ and δ nitrogens are protonated. The one more NH correlation appears at low frequency position in the ^{14}N dimension at -260 ppm suggest that this amino acid is Zwitterion with the NH$_3^+$ moiety. This is because of small quadrupolar coupling in NH$_3^+$ due to the local symmetry. On the other hand, two L-histidine polymorphs only gives two NH peaks for each. It is clear both are Zwitterion and only one of τ and δ nitrogen is protonated. It should be noted that the $^1H/^{14}N$ takes typically less than 10 minutes because both ^1H and ^{14}N are abundant nuclei.

All the above measurements were performed using JNM-ECZ600R spectrometer (JEOL RESONANCE Inc., Japan) equipped with 1 mm fast MAS ssNMR probe (JEOL RESONANCE Inc.) at 14.1 T. The sample amount used in the measurements is about 1 mg for each.

New Methods Developed for Crystalline Polymorphs

In spite of the importance of nitrogen in chemistry, pharmacy, material sciences etc., nitrogen NMR is rather limited. This is simply because low sensitivity of ^{15}N NMR due to low abundance of ^{15}N (0.4%). Although ^{15}N is preferred because of its spin quantum number of I = 1/2, the other isotope of ^{14}N is also NMR active nucleus with favorable high abundance of 99%. The integer spin quantum number (I = 1) and presence of quadrupolar coupling hampers the application of ^{14}N NMR. To overcome these problems, we developed the ^1H-{^{14}N} heteronuclear multi-quantum coherence (HMQC) measurements at very fast MAS conditions [8]. This method enables high throughput measurements with mass limited samples less than 1 mg. Because of high sensitivity, the method can be expanded into three dimensions for $^{14}N/^1H$ DQ/^1H SQ correlation experiments[9]. In addition, the method explores the observation of ^{35}Cl which is often found in pharmaceutical salt [10].

Signal assignments helps to interpret the NMR spectra as discussed above in Fig. 6. While two dimensional homo/heteronuclear correlation helps a lot to assign the signal through

Fig. 6
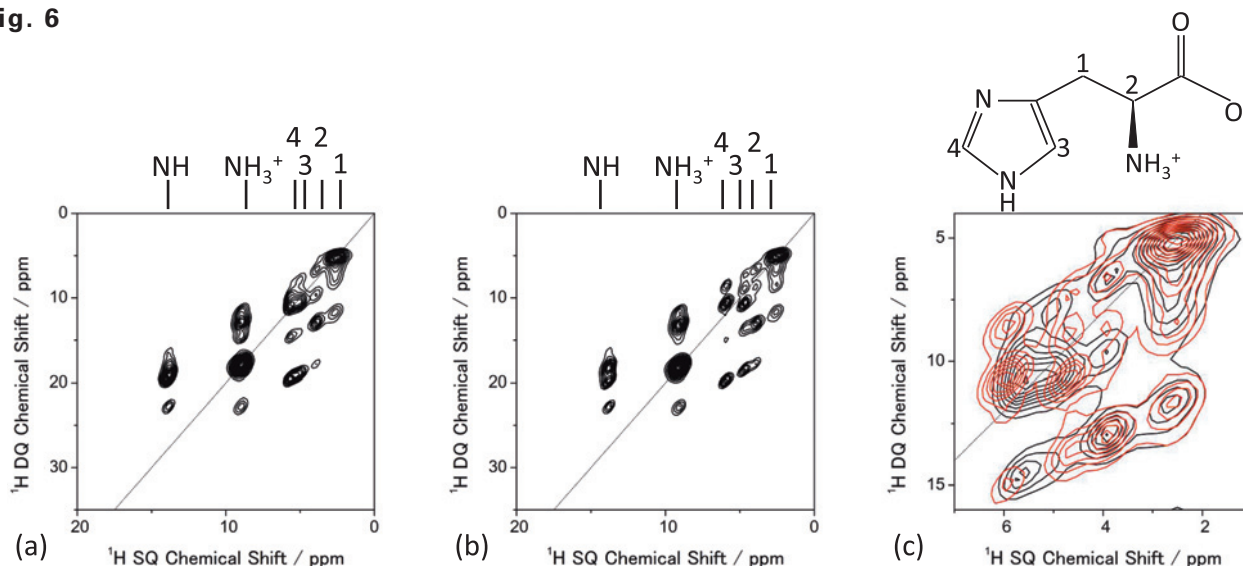
^1H DQ/^1H SQ NMR spectra of (a) L-histidine (orthorhombic) and (b) L-histidine (monoclinic). The expansion of overlaid spectra is also shown in (c) (L-histidine (orthorhombic) in black and L-histidine (monoclinic) in red). Four scans for each t$_1$ period were accumulated with 32 t$_1$ increments. The figure is reproduced from the reference 7.

Fig. 7
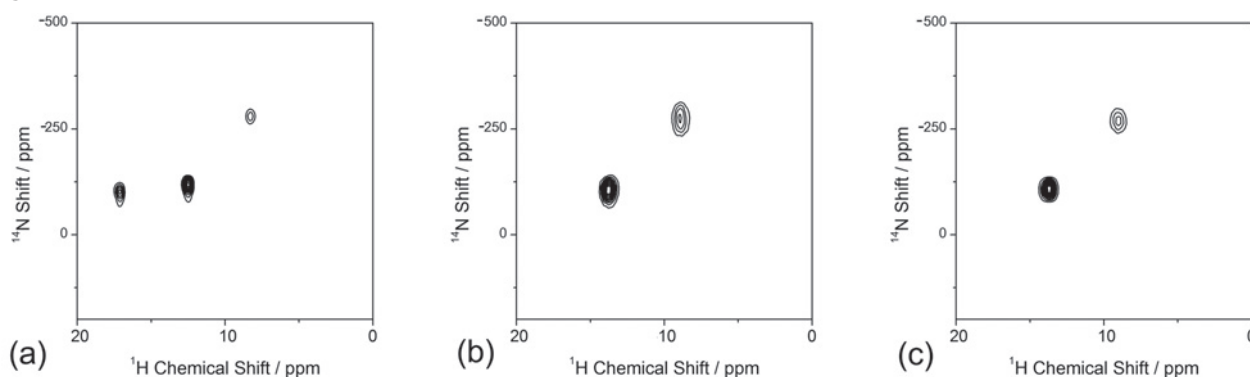
The $^1H/${^{14}N} NMR spectra of (a) L-histidine·HCl·H$_2$O, (b) L-histidine (orthorhombic) and (c) L-histidine (monoclinic). Spectrum (a) was measured at a 90 kHz MAS rate with a 0.75 mm HXMAS probe (JEOL RESONANCE Inc., Japan). Eight scans for each t$_1$ period were accumulated with (a) 64 and (b)/(c) 32 t$_1$ increments. No ^1H–^{14}N recoupling was applied during the mixing time. The figure is reproduced from the reference 7.

two-spin connectivites, three dimensional experiments gives much clearer assignments. To this end, we developed ^{13}C/^{1}H DQ/^{1}H SQ correlation to reveal the local ^{1}H-^{1}H spin network in vicinity of ^{13}C [11]. The complete assignments were achieved from a single three dimensional spectra with 1 mg sample at natural abundance.

Salt/Cocrystal/Continuum[12]

As discussed above, the identification of salt/cocrystal/continuum still remains a big issue in pharmaceutical applications because of lack of ability to locate hydrogen in XRD. The difference between these three classes can be interpreted as the different distances between hydrogen and nitrogen (**Fig. 8**). Thus, the size of ^{1}H-^{15}N dipolar interactions, which are inversely proportional to cube of the internuclear distances, should give clear answer to salt/cocrystal/continuum.

Here, we propose a combined method of SCXRD and ssNMR. While SCXRD determines global crystalline structure, ssNMR gives local internuclear distances. By combining these two kinds of information, the seamless understanding of the crystalline structure can be established. As a demonstration, first, we synthesize four model multi-component systems shown in **Fig. 9**. The crystalline structures are determined by SCXRD. The results clearly show the presence of intermolecular contact between N and OH as expected (**Fig. 10**). The question is whether it is salt/cocrystal/continuum. To answer this question, we tried to determine the hydrogen positions by SCXRD, however, it gives machine dependent values, resulting in unreliable positions. As the crystalline structure determined by SCXRD clearly shows, there is intermolecular ^{1}H/^{15}N coupling. The ^{1}H/^{15}N distances, thus coupling strength between ^{1}H and ^{15}N, should give the answer to salt/cocrystal/continuum problems. For example,

^{1}H/^{15}N distance in SA2 is determined to be 1.25 Å (Fig. 10). With the distances between nitrogen and oxygen of 2.54 Å, which is determined by SCXRD, we can conclude SA2 is continuum as hydrogen is located at the middle of oxygen and nitrogen. It should be noted that SA2 is consisted of strong acid and base with ΔpKa larger than 3. This result highlights the importance of SCXRD/ssNMR measurements to identify salt/cocrystal/continuum even for the system with large ΔpKa. The structures and internuclear distances of the other three systems have been successfully determined (Fig. 10). The bottleneck of this method is experimental time for ^{1}H-^{15}N distance measurement. In addition to the low natural abundance of ^{15}N and small ^{1}H-^{15}N couplings, these pharmaceutical samples typically show very long ^{1}H T$_1$ relaxation time. Moreover, the need of fast MAS reduces the sample volume, resulting in further sensitivity reduction. We have developed a method to improve the throughput as discussed in the following section, each measurements still requires 4-5 days. We agree with the fact of the limited throughput. Nevertheless, we believe this method is quite useful as no other method gives clear answer.

All the NMR measurements were conducted with JNM-ECA700II NMR spectrometer (JEOL RESONANCE Inc.) using 1 mm double resonance fast MAS probe (JEOL RESONANCE Inc.) at 16.4 T.

New Methods Developed for Salt/Cocrystal/Continuum

The size of ^{1}H/^{15}N dipolar coupling should be precisely measured. However, it is not straightforward task because of 1) low abundance of ^{15}N (0.4%), 2) small gyromagnetic ratio (1/10 of ^{1}H), and 3) abundant ^{1}H nuclei which are not bonded to ^{15}N, resulting in low sensitivity, small dipolar coupling (1-7 kHz), and overlapping of ^{1}H resonances, respectively. More importantly, the previous methods tend to show the ^{1}H/^{15}N dipolar coupling which depends on experimental conditions, giving unreliable distances. To overcome these difficulties, we have introduced inverse detected CP with variable contact time (inv CP-VC) method at fast MAS [13]. Firstly, the method gives well defined dipolar splittings which is independent to experimental conditions [14]. Actually, the scaling factor of inv CP-VC method largely depends on the rf field strength. However, signals from the area with B$_1$ inhomogeneity are scattered over the broad spectral range, making these signals invisible. Thus the signals from homogeneous B$_1$ field are selectively observed. The sensitivity enhancement by ^{1}H detection in inv CP-VC alleviates the low sensitivity due to small abundance and sample volume. Experimentally, it is shown that inv CP-VC is capable to monitor

Fig. 8
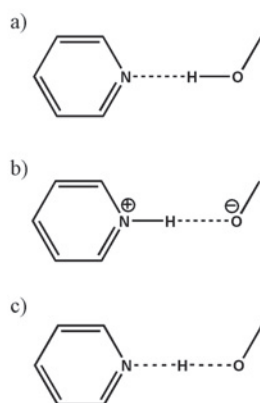
Schematic presentation of (a) a cocrystal, (b) a salt and (c) a continuum (where the H-atom position is shared between the two heavy atoms) in a typical O...H...N interaction. The figure is reproduced from the reference 12.

Fig. 9
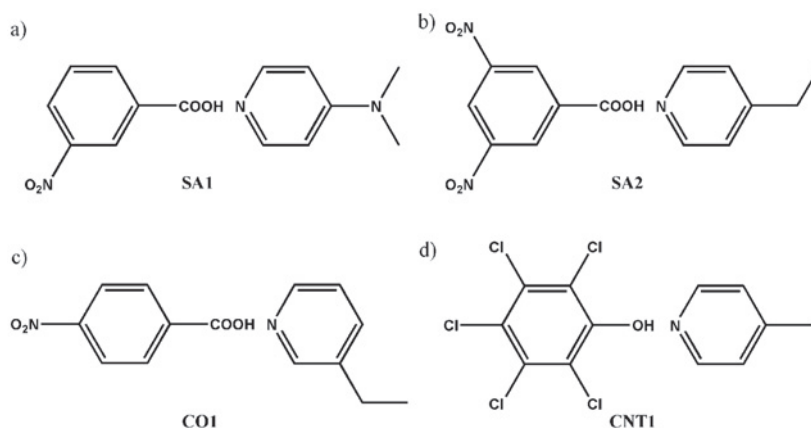
Schematic representation of the compounds used in the present study, showing (a) SA1 (3-nitrobenzoic acid and N,N-dimethypyridin-4-amine), (b) SA2 (3,5-dinitrobenzoic acid and 4-ethylpyridine), (c) CO1 (4-nitrobenzoic acid and 3-ethylpyridine) and (d) CNT1 (pentachlorophenol and 4-methylpyridine). The figure is reproduced from reference 12.

Fig. 10

CO1

SA2

SA1
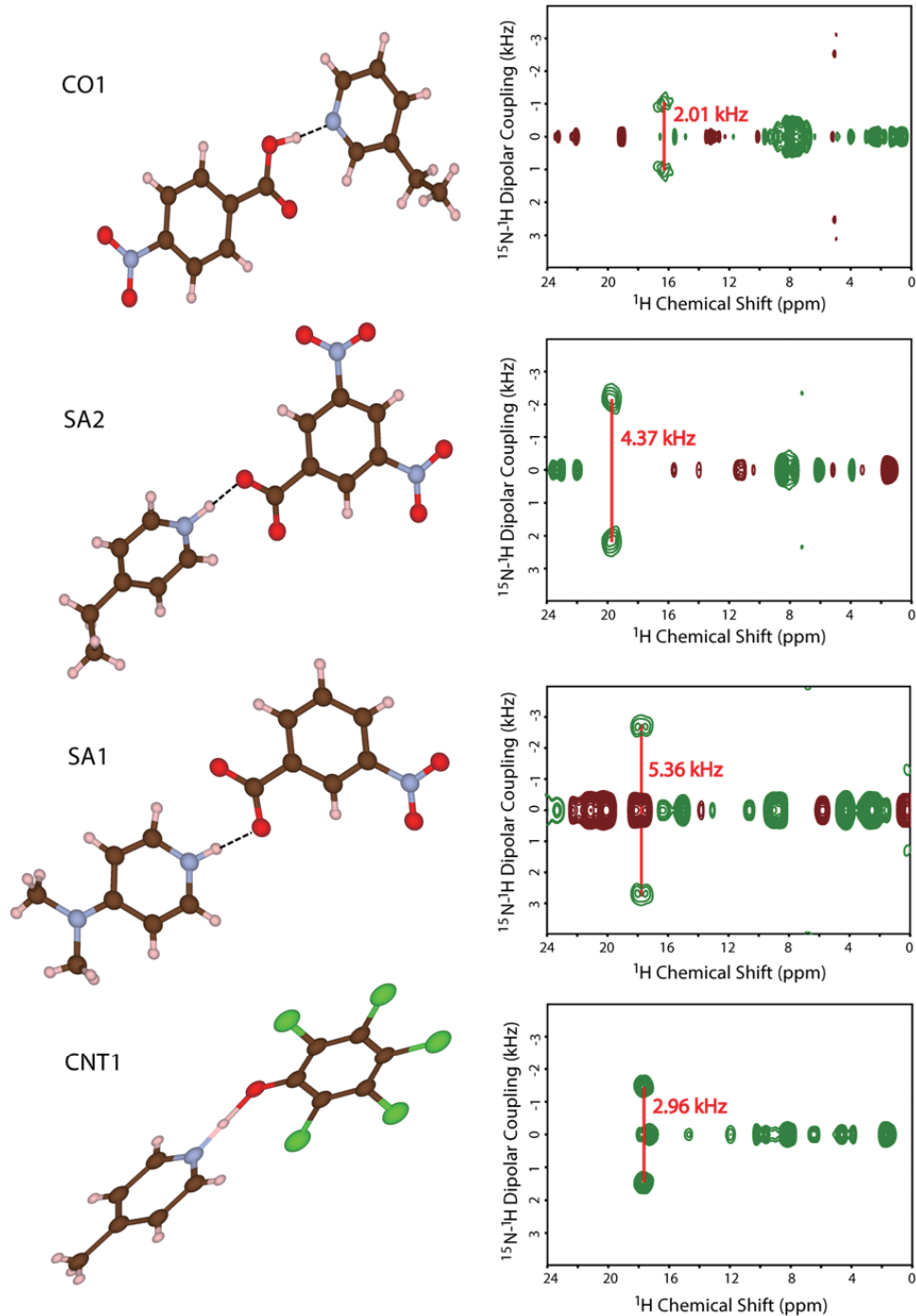
CNT1

The molecular structures and the two-dimensional invCP-VC spectra (^{15}N-^{1}H dipolar couplings versus ^{1}H chemical shift) of SA1, SA2, CO1 and CNT1. The figure is reproduced from the reference 12.

a ^{1}H/^{15}N coupling of 2 kHz. The inv CP-VC works as filtering of ^{1}H resonances, giving selective observation of ^{1}H in vicinity of ^{15}N. This avoids the complexity of overlapped resonances between ^{1}Hs. In addition, inv CP-VC paves a way to analyze mass limited samples less than 1 mg.

Repetition delay must be inserted between the consecutive scans in NMR measurements so that the spin system returns to close to the thermal equilibrium before starting the NMR measurements. As the repetition delay should be an order of T_1 relaxation time, which is typically much longer than the rest of the experiments, T_1 relaxation time is the dominating factor of experiment time in NMR. In the inv CP-VC experiments, the magnetization starts from ^{1}H, thus, ^{1}H T_1 is important. However, well crystalline low-molecular weight APIs tend to have very long ^{1}H T_1 relaxation time of tens to hundreds of seconds, reducing the

throughput dramatically. At the fast MAS rate, the issue is more severe, because ^{1}H-^{1}H spin diffusion is suppressed, resulting in longer ^{1}H T_1 relaxation time. Since NH protons, which are of our interest, are spatially and spectrally isolated from the other ^{1}Hs, very slow ^{1}H-^{1}H spin diffusion hampers the ^{1}H magnetization from recovering to its thermal equilibrium. This results in slower ^{1}H T_1 relaxation time of NH protons compared to the rest of 1Hs. To overcome this difficulty, we have applied radio-frequency driven recoupling (RFDR) sequences on ^{1}H, during repetition delay [15]. This enhances the ^{1}H-^{1}H spin diffusion, bringing the magnetization from rapidly relaxing ^{1}H to NH protons. Since the relaxation mechanisms of rapidly relaxing proton are utilized multiple times, not only NH proton but also the overall sensitivity could also be improved. We also optimized the phase cycling in the RFDR sequence suitable to ^{1}H mixing [16, 17].

Conclusion

Both TEM and NMR are continuously improved even now despite the fact that they have been introduced more than 70 years ago. The recently introduced high sensitivity camera in TEM opens a way to the novel application in cryo TEM to determine the protein structure using the single particle analysis approach. The sensitivity enhancement is beneficial for not only protein but also beam-sensitive samples including low-molecular weight API. Another big burst is observed in fast MAS technology of ssNMR, which enables ^{1}H NMR even rigid solids. These new developments not only provide the new information which had previously been inaccessible but also improve the throughput, which is one of the key factors for wide spread of use. In addition, it is quite important to apply several different analytical methods which are complimentary to each other. The proper combination provides useful information with high throughput. Indeed, JEOL Ltd. also pushes the YOKOGUSHI strategy to offer attractive combinations of equipments.

In this article, we combine XRD, ED, and ssNMR to solve the structural problem in pharmaceutical sciences including crystalline polymorphs and salt/cocrystal/continuum issues. For the crystalline polymorphs issue, we demonstrate the combined approach of ED and ^{1}H fast MAS NMR to identify the crystalline form, as a method complimentary to the PXRD and ^{13}C CPMAS. ED enables crystalline form determination from nano- to micro-sized single crystals. On the other hand, ^{1}H fast MAS can distinguish the crystalline form with similar molecular conformation. In addition, fast MAS enables ^{1}H/^{14}N correlations, giving proton positions close to nitrogen nuclei. To identify the salt/cocrystal/continuum, the combined approach of SCXRD and ssNMR at very fast MAS rate is introduced. While SCXRD provide the global molecular structure, it fails to determine the proton positions which are crucial to salt/cocrystal/continuum issue. On the other hand, ssNMR gives precise [1]H-^{15}N distances, although the global structure is hardly obtained. This approach provides seamless understanding of molecular structure from crystalline structure to hydrogen bonding to answer salt/cocrystal/continuum issue. The formation of continuum in the multi-component systems with $\Delta pKa > 3$ highlights the importance of thorough investigation using SCXRD and ssNMR.

Acknowledgments

References

[1] R. K. Harris, *J. Pharm. Pharmacol*. **59** (2007) 225–239.

[2] M. Geppi, G. Mollica, S. Borsacchi, C. A. Veracini, *Appl. Spectrosc. Rev*. **43** (2008) 202–302.

[3] F. G. Vogt, *Future Med. Chem*. **2** (2010) 915–921.

[4] Y. Nishiyama*, Fast Magic-Angle Sample Spinning Solid-State NMR at 60-100 kHz for Natural Abundance Samples, *Solid State Nuclear Magnetic Resonance*, **78** (2016) 24-36. DOI: 10.1016/j. ssnmr. 2016.06.002.

[5] Y. Nishiyama*, Solid-state NMR under ultrafast MAS rate of 40 – 120 kHz, in Experimental Approaches of NMR Spectroscopy - Methodology and Application to Life Science and Materials Science, Springer (2017).

[6] T. Kobayashi, Y. Nishiyama*, M. Pruski*, Heteronuclear correlation spectroscopy with inverse detection, in Modern Methods in Solid-State NMR: A Practitioner's Guide, Royal Society of Chemistry (2018).

[7] T. Oikawa, M. Okumura, T. Kimura, Y. Nishiyama*, Solid-state NMR meets electron diffraction: Determination of crystalline polymorphs of small organic microcrystalline samples, *Acta Cryst*. **C73** (2017) 219–228. DOI: 10.1107/S2053229617003084.

[8] Y. Nishiyama*, Y. Endo, T. Nemoto, H. Utsumi, K. Yamauchi, K. Hioka, T. Asakura, "Very fast magic angle spinning ^{1}H-[14]N 2D solid-state NMR: sub-micro-liter sample data collection in a few minutes", *J. Magn. Reson*. **208** (2011) 44-48.

[9] G. N. M. Reddy, M. Malon, A. Marsh, Y. Nishiyama, S. P. Brown*, A fast magic-angle spinning three-dimensional NMR experiment for simultaneously probing H-H and N-H proximities in solids, *Analytical Chemistry*, **88** (2016) 11412–11419.

[10] M. K. Pandey, H. Kato, Y. Ishii, Y. Nishiyama*, Two-dimensional proton-detected [35]Cl/^{1}H correlation solid-state NMR experiment under fast magic angle sample spinning: Application to pharmaceutical compounds, *PhysChemChemPhys*, **18** (2016) 6209-6216.

[11] M. Malon, M. K. Pandey, Y. Nishiyama*, Revealing the Local Proton Network Through Three-Dimensional ^{13}C/[1]H Double Quantum/[1]H Single Quantum and [1]H Double Quantum/^{13}C/[1]H Single Quantum Correlations Fast MAS Solid-State NMR Spectroscopy at Natural Abundance, *J. Phys. Chem*. **B 121** (2017) 8123-8131. DOI: 10.1021/acs.jpcb.7b06203.

[12] L. Rajput†, M. Banik†, J. R. Yarava, S. Joseph, M. K. Pandey, Y. Nishiyama*, G. R. Desirajua*, Exploring the salt-cocrystal continuum with solid-state NMR using natural abundance samples: implications for crystal engineering, IUCrJ 4 (2017) 466-475. DOI: 10.1107/S205225251700687X.

[13] Y. Nishiyama*, M. Malon, M. J. Potrzebowski, P. Paluch, J. P. Amoureux*, Accurate NMR determination of C–H or N–H distances for unlabeled molecules, *Solid State Nucl. Magn. Reson*. **73** (2016) 15-21. DOI: 10.1016/j. ssnmr. 2015.06.005.

[14] P. Paluch, J. Trébosc, Y. Nishyama, M. Potrzebowski*, M. Malon, J. -P. Amoureux*, Theoretical study of CP-VC: a simple, robust and accurate MAS NMR method for analysis of dipolar C-H interactions under rotation speeds faster than ca. 60 kHz, *J. Magn. Reson*. **252** (2015) 67-77.

[15] Y. Q. Ye, M. Malon, C. Martineau, F. Taulelle, Y. Nishiyama*, Rapid measurement of multidimensional ^{1}H solid-state NMR Spectra at ultra-fast MAS frequencies, *J. Magn. Reson*. **239** (2014) 75-80.

[16] Y. Nishiyama, R. Zhang, A. Ramamoorthy, Finite-Pulse Radio Frequency-Driven Recoupling with Phase Cycling for 2D ^{1}H/[1]H Correlation at Ultrafast MAS Frequencies, *J. Magn. Reson*. **243** (2014) 25-32.

[17] R. Zhang, Y. Nishiyama, P. Sun, A. Ramamoorthy*, Phase Cycling Schemes for finite-pulse-RFDR MAS Solid State NMR Experiments, *J. Magn. Reson*. **252** (2015) 55-66.

Structural Analysis of Semiconductor Devices by Using STEM/EDS Tomography

Yoshitaka Aoyama[1], Ichiro Ohnishi[1], Noriaki Endo[1], Eiji Okunishi[1], Takeo Sasaki[2], Yorinobu Iwasawa[3], Yukihito Kondo[1]

[1] EM Business Unit, JEOL Ltd. [2] JEOL (U.K.) LTD. [3] EC Business Unit, JEOL Ltd.

Recently, semiconductor devices are designed to be a 3D stacking architecture for high performance and high integration. Therefore, 3D structural analysis of semiconductor devices with nano-scale meter resolution is important for improving semiconductor devices. EDS tomography is getting popular for characterization of samples having 3D structures such as semiconductor devices or metal materials, since the method enables us to see 3D distribution of the atomic species for samples. It is essential to enhance the sensitivity of X-ray detection, since the signals of characteristic X-rays are generally weak. To obtain more X-ray signals from the samples, the X-ray detection system with two EDS detectors was developed. In the system, the detectors are placed symmetrically with respect to the tilt axis of the sample holder. Thus, some portion of the generated X-rays are blocked by the sample holder or supporting grid (mesh) in a specific tilting angle range. The shadowing in this configuration can cause artifacts in the resulting 3D elemental maps. Recently, we developed a new EDS detection system whose detector is placed on the tilting axis of the sample stage in order to obtain EDS tomograms with no shadowing. The system was installed in a 300 kV TEM. EDS tomograms from the paint film sample were obtained using the EDS detector. The intensities of each Ti Kα map were almost constant over the sample tilting range. It is indicated that the EDS detector placed at the new position had almost no blocking of X-ray from the holder and the grid of the sample. The 3D elemental maps of the FinFET, which is one of the modern semiconductor devices, were successfully obtained by using the new EDS detector configuration.

Introduction

Semiconductor devices are widely used in electronic products all over the world. Historically, high density-integrated semiconductor devices have been implemented by downsizing transistors on a chip. Recently, semiconductor devices are designed to be a three-dimensional (3D) stacking architecture for high integration and performance [1-2]. The 3D observation with nanometer scale resolution is essential for development and failure analysis of new devices [3-4]. Electron Tomography (ET) is one of the methods of acquiring 3D structure of the samples with nano-scale 3D resolution by using transmission electron microscopy (TEM). EDS tomography is performed by combining with Energy Dispersive X-ray Spectroscopy (EDS) and ET to realize 3D chemical characterization from sets of the 2D elemental tilt series maps taken by TEM equipped with EDS detectors [5-6]. The technique is applied to the new semiconductor devices and metal materials to observe these 3D structures [7-11]. When the first result of EDS tomography was reported in 2003, silicon-lithium type EDS detectors, which had low analytical counting rate, were commonly used to obtain EDS map of high electron dose and long acquisition time. Therefore, EDS tomography was not useful for 3D elemental analysis because of irradiation beam damage and contamination on samples. But recently, large-sized silicon drift detectors (SDD) and multiple EDS detection system for TEMs were developed [12]. By using the new SDD system, EDS maps can be obtained about 13 times faster than by using the previous silicon-lithium type detection system [13]. EDS tomograms from hard materials have become to be easily obtained by using the dual SDD system, though it is still difficult to obtain EDS tomograms from beam sensitive materials like bio samples.

EDS tomography is a powerful tool to analyze 3D elemental structure qualitatively, but EDS tomography has two kinds of limitation for 3D quantitative analysis caused by the relative positions of TEM samples and EDS detectors [14]. **Figure 1**(a) shows absorption effect, which is a limitation for quantitative analysis in EDS tomography. The black arrows indicate the paths of X-rays generated by incident electrons. When the structure of the sample is symmetric, the total amount of the generated X-rays from the near side and far side of the EDS detectors is the same. However, the generated X-rays from

the far side can be absorbed by the sample itself. As a result, the detected X-rays from the far side are fewer than that from the near side. The absorption effect can cause artifacts in the resulting 3D elemental map. The recent study has attempted to compensate the self-absorption effect by calculation on the acquired EDS tomograms [15]. Figure 1(b) shows another limitation, that is shadowing effect. Normally, TEM samples were fixed on a grid and the gird is fixed on a sample holder. When two EDS detectors are located symmetrically with respect to the tilt axis of the sample holder in the previous EDS system, some of the generated X-rays are blocked by a grid or a sample holder in a specific tilting angle range. The shadowing in this configuration can also cause artifacts in the resulting 3D elemental map. In order to avoid this shadowing effect, it is necessary to correct the measured intensity of the EDS map after acquisition, according to the expected or pre-measured detection efficiency. For 3D quantitative analysis, both absorption effect and shadowing effect have to be removed from EDS tomograms.

The previous EDS-detector configuration is shown in **Fig. 2**(a). The EDS detectors are located on both sides of the tilting axis. In this configuration, the solid angles of the SDDs are varied on the tilting angle. We have improved to this variation by a new EDS-detector configuration, where SDD is placed on the tilting axis (Fig. 2(b)). It was expected that the SDD on the tilting axis has no shadowing effect in all tilting angle range for EDS tomography. The purpose of this study is to make clear that a new EDS-detector configuration have no shadowing effect in EDS tomography and to obtain 3D quantitative elemental maps from the semiconductor devices.

Experimental

The microscope used for our experiments was an aberration corrected 300 kV TEM (JEM-ARM300F, JEOL Ltd.) equipped with two SDDs (see **Fig. 3**). One detector is located on the tilting axis of a sample holder (SDD2), and the other is in the right side of the tilting axis (SDD1) (Fig. 2(b)). For obtaining the EDS tomogram quickly with no shadowing effect by using only SDD2, the 300 kV TEM equipped with a new pole piece, a new analytical high tilting holder and large-sized SDDs, was used. The new pole piece, named the wide gap pole piece (WGP), was designed thinner than the previous pole piece in order that EDS detectors can approach close to the sample holder. The spatial resolution of the 300 kV TEM with WGP is 0.062 nm due to the Cs aberration corrector. The new analytical high tilting holder was developed for EDS tomography. The tip of this holder is narrow and thin so as to make the generated X-ray unblocked for EDS tomography. By using these attachments and large-

---

Fig. 1 Schematic diagrams of the two limitations for 3D quantitative analysis in EDS tomography.
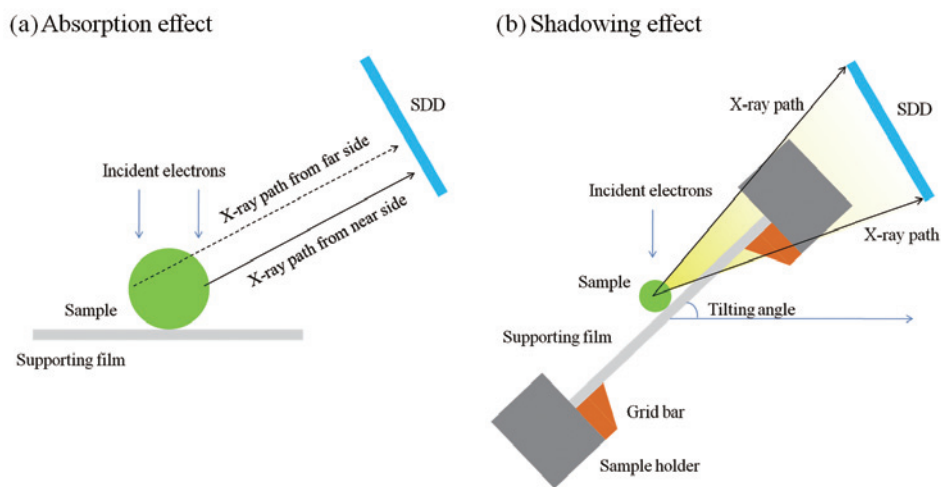
(a) Absorption effect by sample. The X-rays from the far side of the sample are more absorbed by the sample itself than that from the near side. (b) Shadowing effect by sample holder. The X-rays from the sample are blocked by the sample holder or grid bars in a specific tilting angle range. The black arrows show the ray path toward the EDS detectors.

Fig. 2
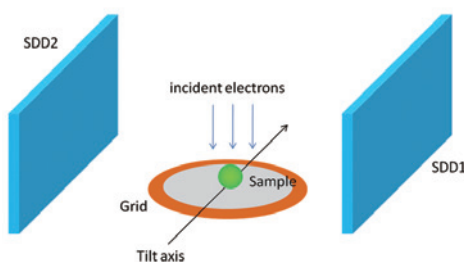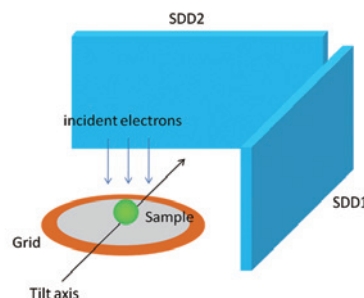
(a) Previous EDS detection system, which consists of two SDDs located symmetrically. One on the right side of the tilt axis and the other on the opposite side. (b) New configuration of the EDS detection system. There are also two SDDs, and SDD2 is added to the tilt axis. It is expected that quantitative EDS tomogram without shadowing effect can be obtained by using only SDD2 for EDS tomography.

Fig. 3

(a) 300 kV TEM with wide gap pole piece

(b) Large sized SDD (158 mm²)

(c) High Tilt Analytical Holder

(a) 300 kV TEM (JEM-ARM300F, JEOL Ltd.) with the two large sized SDD shown in (b). The detection area is 158 mm². (c) High tilt analytical holder developed for EDS tomography. The tip of the holder is narrower and thinner than the standard one so as not to block the generated X-rays.

sized SDDs, whose detection area is 158 mm², the solid angle of only SDD2 is reached to be more than 1.1 sr. Our EDS detection system can realize high spatial resolution and high analytical counting rate even with a single detector [13].

We prepared two kinds of samples for our experiments. One is a paint film sample to evaluate the shadowing effect in the new EDS detection system. The other is the fin-type field effect transistor (FinFET) which is one of cutting-edge semiconductor devices. The bulk of paint films, which were embedded by epoxy resin, were sliced by microtomy to be 200 nm thick. The thin sections were mounted on a supported membrane of the 3 mm-diameter thin-bar grid. 2D EDS maps were obtained using the 300 kV TEM with a probe current of 300 pA. A tilt series of EDS maps from -60 to +60 degrees with a 5 degree increment were automatically acquired by the tomography software (TEMography, SYSTEM IN FRONTIER Inc.) which is installed in the control PC for the TEM. The size of each EDS map was 256 by 256 pixels. The pixel size was 9.766 nm/pixel. The acquisition time was 190 minutes. All of EDS maps taken in our experiment were translated to the net counts maps from gloss counts maps with the same condition by using batch processing implemented in the EDS analyzer software (Analysis Station™, JEOL Ltd.). At the beginning in the reconstruction procedure, tilt series of HAADF-STEM images were aligned by fiducial markers and the 3D structures without elemental information were reconstructed. The 3D reconstruction algorithm for this reconstruction was simultaneous iterative reconstruction technique (SIRT). Both the same alignment condition and the same reconstruction condition were applied to the EDS tilt series by using batch processing implemented in the TEMography software. Finally, we obtained the 3D elemental maps of paint film samples.

The FinFET sample was roughly cut by a low speed diamond wheel saw. The section of the sample was thinned by mechanical polishing. Finally the samples were milled by Argon ions milling machine (Ion Slicer™, JEOL Ltd.) for TEM observation [16]. The gold colloidal particles with a diameter of 5 nm were dropped down on the sample and used as a fiducial marker for alignment of the tilt series. The TEM was operated at an accelerating voltage of 200 kV. The tilt series of EDS elemental maps were automatically acquired in a tilting angular range from +64 to -64 degrees. The degree step is 4 degree. The size of each EDS map was 256 by 256 pixels. The pixel size was 1.953 nm/pixel. Current density was 300 pA. The total acquisition time was about 120 minutes by using the single SDD (SDD2). The reconstruction procedure of the FinFET sample was the same as the paint film sample.

Results and Discussion

EDS tomograms from the paint film sample were obtained in order to evaluate the shadowing effect in the new EDS detection system, which was installed in 300 kV TEM. The HAADF images and 3D elemental maps were shown in **Fig. 4**. The paint film sample consisting of titanium oxide particles, small silica particles, small iron oxide particles and carbon resin are marked in yellow, green, magenta and blue colors in Fig. 4(b), respectively. The measured total intensities of Ti Kα from the EDS maps of the paint film sample are plotted against the tilting angle of the sample stage in the TEM. The red, blue and green dots shown in **Fig. 5** correspond to the total intensities detected by SDD1, SDD2 and SDD1+SDD2, respectively. Because the volumes of the titanium oxide particles in each EDS map are constant, the total intensities from Ti Kα maps have to be constant in the result of quantitative EDS analysis. However, the intensities detected by SDD1 and SDD1+SDD2 decreased around -20 degrees by the shadowing effect. On the other hands, the intensities detected by SDD2 kept almost constant over the sample tilting range. This result indicates that the EDS detector located on the tilting axis had almost no blocking of X-rays from the holder and the grid of the sample. A nearly shadow-less EDS tomography system was realized by using this single EDS detector.

The shadow-less EDS tomography system was applied to the semiconductor devices. The HAADF image and the EDS tilt series maps of the FinFET were obtained by the 300 kV TEM shown in **Fig. 6**. The white dots in the HAADF image correspond to the gold nano-particles which were used as fiducial makers for the alignment in 3D reconstruction procedure. 3D elemental maps of the FinFET shown in Fig. 6 were reconstructed by using SIRT algorithm. In the resulted maps, germanium, titanium, tungsten, oxygen, nitrogen and silicon were detected. The 3D structures of the gate electrode on the silicon substrate were clearly observed by EDS tomography. The 3D nitrogen map corresponding to the insulating film was

**Fig. 4**

(a) DF-STEM image   (b) 3D elemental map

600 nm
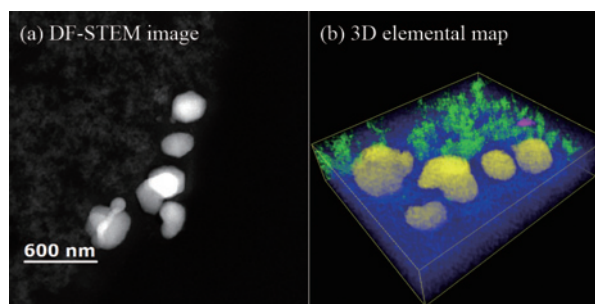
(a) The HAADF image of the paint film sample, taken by JEM-ARM300F equipped with the EDS detector, whose detector area is 158 mm². (b) The 3D image reconstructed from the sample shown in (a). Colors indicate atomic species: yellow (Ti), green (Si), magenta (Fe) and blue (c).

still noisy. Higher electron dose or longer acquisition time is necessary to observe 3D elemental distributions of light elements with high signal to noise ratio even by using the highly sensitive 158 mm² SDD. **Figure 7** shows the slices normal to the X, Y and Z directions extracted from the obtained 3D elemental volume map. The position of the Y-cut slice map is indicated by a yellow line in the corresponding Z-slice map shown below the Y-cut slice map. The germanium stressor (yellow), tungsten electrode (green) and the silicon channel (blue) are clearly seen in the Y-cut slice map (a). And the nitrogen (magenta) located between the channel and electrode was obtained in the 3D elemental maps. From these results, we can conclude that the EDS tomography is useful to analyze 3D elemental structures of modern semiconductor devices.

In this study, we tried to remove the shadowing effect in EDS tomography by improving the detector configuration in the TEM. However, the absorption effect also has to be removed for 3D quantitative analysis. When samples consist of light elements together with heavy elements, the effect of absorption was serious in quantitative 3D elemental analysis by EDS tomography. We have evaluated the effect of X-ray absorption by the paint film sample itself in EDS tomography. The EDS tomogram data set were taken by a 200 kV TEM (JEM-F200, JEOL Ltd.) equipped with two SDDs which were located on the tilting axis and in the right side of the sample holder, respectively. The 3D elemental maps of titanium, iron, aluminum, silicon, oxygen and carbon were reconstructed from the EDS tilt series maps of the paint film samples. The elemental composition ratio with voxel by voxel was calculated by using Cliff-Lorimer method. We have compared the 3D composition ratios from the three titanium dioxide particles which were indicated by the yellow arrows in **Fig. 8**. The 3D composition ratio from the particles with the diameter of 115 nm was consistent with the fact that the particles were titanium dioxide. But the atomic percent of oxygen in the particles with diameters of 190 nm and 315 nm was underestimated. It is considered that

---

Fig. 5
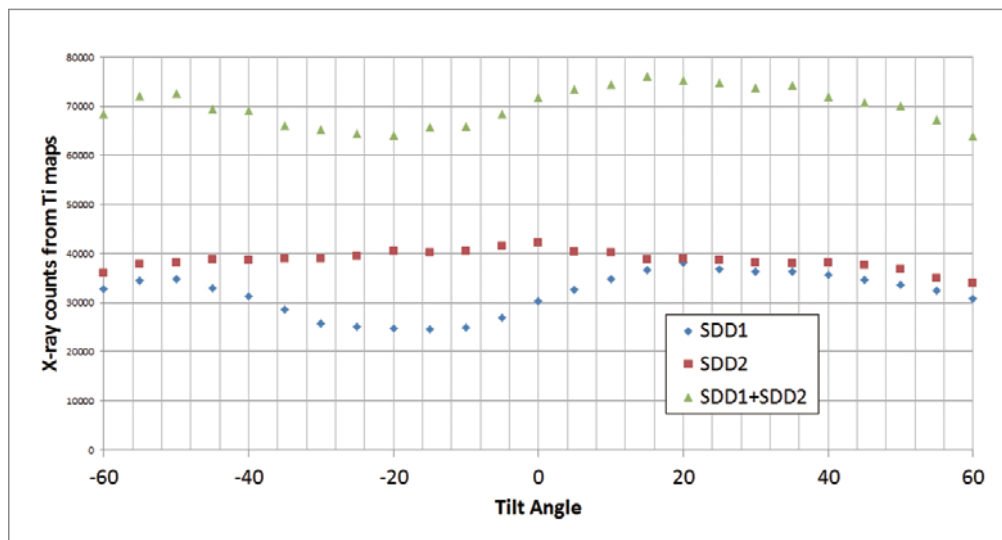
Total intensities of Ti Kα maps of the paint film sample using different detector signals plotted against the tilting angle. The blue dots, red dots and green dots correspond to the Ti Kα maps made by the signals of the SDD1, SDD2 and SDD1+SDD2, respectively. The intensities detected by SDD2 were almost constant over the sample tilting range for ET.

Fig. 6
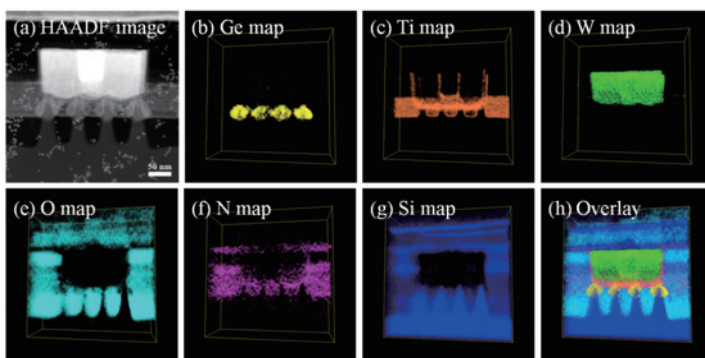
(a) HAADF image of the FinFET sample taken by a JEM-ARM300F equipped with single large-sized SDD whose detection area is 158 mm². White dots correspond to gold nano-particles used as fiducial markers. (b)-(h) 3D elemental maps of the same sample in (a), reconstructed from the EDS tilt series maps, showing the distribution of germanium, titanium, tungsten, oxygen, nitrogen and silicon atoms, respectively. The sample was thinned by ion milling. The size of the reconstructed volume is (381, 377, 121) nm.

Fig. 7
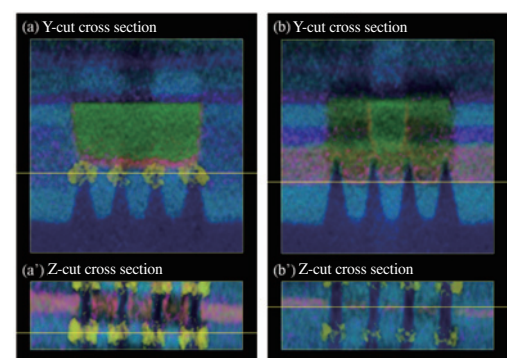
Y-cut and Z-cut slice maps extracted from the reconstructed 3D elemental volume map of the FinFET sample using EDS tomography. (a) and (b) show elemental maps of the Y-cut slices at different positions indicated by a yellow line in the corresponding Z-cut slice maps below. The Z-cut slice is parallel to the wafer surface. The germanium stressor, tungsten electrode and silicon channel and substrate are colored yellow, green and blue, respectively.

Fig. 8
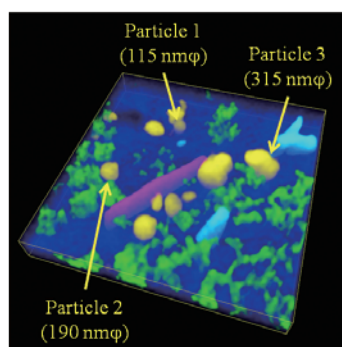
Element	Atomic %		
	Particle 1 (115 nmφ)	Particle 2 (190 nmφ)	Particle 3 (315 nmφ)
Titanium	31.86	38.43	45.69
Iron	0.12	0.54	0.51
Aluminum	0.58	0.94	0.74
Silicon	0.53	1.22×10^{-5}	6.69×10^{-4}
Oxygen	65.51	58.79	53.05
Carbon	1.39	1.30	0.01

3D elemental map of the paint film sample reconstructed by EDS tomogram obtained using JEM-F200 equipped with the SDDs with 100 mm² detection area (the left figure). 3D quantitative analysis of the three titanium dioxide particles indicated by the yellow arrows was shown in the right table. The composition ratio of oxygen in the particle 2 and 3 is underestimated due to the X-ray absorption effect. The absorption effect cannot be ignored for quantitative analysis in EDS tomography.

the X-rays from oxygen were absorbed by the sample itself. The corrections of the absorption effect are desired to analyze 3D quantitative elemental distribution with high accuracy in EDS tomography.

Summary

In order to obtain quantitative 3D elemental analysis, we developed the new EDS detection system for TEMs, and installed the system to the aberration corrected 300 kV TEM. The detection system consisted of the two differently configured EDS detectors, which are placed on the tilting axis of the sample stage (SDD2), and in the right side of the tilting axis (SDD1). The detection areas of these SDDs are 158 mm². In addition, we developed the high tilt analytical holder whose tip is narrower and thinner than the standard holder to make the generated X-ray from samples unblocked. By using this microscope with these attachments, the solid angles of SDD1 and SDD2 are 1.106 sr and 1.108 sr, respectively. EDS tomograms from the paint film samples were obtained by using the new EDS detection system. The total intensities from the Ti Kα maps of the paint film were almost constant over the sample tilting range for tomography. The result indicated that the new EDS detection system can obtain EDS tomograms with no shadowing effect. The 3D elemental maps from the FinFET were obtained with no shadowing effect by using the new EDS detection system. The shadowing effect can be removed by our EDS detection configuration. The correction of the absorption effect is desired to analyze 3D quantitative elemental distribution with high accuracy in EDS tomography.

References

[1] D. Hisamoto, W. C. Lee, J. Kedzierski, E. Anderson, H. Takeuchi, K Asano, T. J. King, J. Bokor and C. Hu, "A folded-channel MOSFET for deep-sub-tenth micron era", IEDM Tech. Dig., (1998) pp. 1032-1034.

[2] H. Tanaka, M. Kido, K. Yahashi, M. Oomura, R. Katsumata, M. Kito, Y. Fukuzumi, M. Sato, Y. Nagata, Y. Matsuoka, "Bit Cost Scalable Technology with Punch and Plug Process for Ultra High Density Flash Memory" Proceedings of the Symposium on VLSI Technology, (2007) pp. 12–14.

[3] A. M. Cormack, *J. Applied Physics*, **35**, (1964) p. 2908.

[4] M. Hayashida, L. Gunawan, M. Malac, C. Pawlowicz and M. Couillard, "High-accuracy electron tomography of semiconductor devices", *Microsc. Microanal*., **21**, 3 (2015).

[5] B. Fu, M. Gribelyuk, L. Dumas, C. Fang, N. LaManque, L. Hodgkins and E. Chen, "The Combination of STEM Tomography and STEM/EDS Analysis of NiSi Formation Related Defects in Semiconductor Wafer-foundries", *Microsc. Microanal*., **22**, 3 (2016).

[6] K. Lepinay, F. Lorut, R. Pantel and T. Epicier, "Chemical 3D tomography of 28 nm high K metal gate transistor: STEM XEDS experimental method and results", *Micron* **47** (2013) pp. 43–49.

[7] P. Burdet, J. Vannod, A. Hessler-Wyser, M. Rappaz and M. Cantoni, "Three-dimensional chemical analysis of laser welded NiTi-stainless steel wires using a dual-beam FIB", *Acta Mater*., **61**, 8 (2013) pp. 3090–3098.

[8] A. Genc, L. Kovarik, M. Gu, H. Cheng, P. Plachinda, L. Pullan, B. Freitag and C. Wang, "XEDS STEM tomography for 3D chemical characterization of nanoscale particles", *Ultramicroscopy* **131** (2013) pp. 24–32.

[9] B. Goris, L. Polavarapu, S. Bals, G. Van Tendeloo and L. Liz-Marzan, "Monitoring galvanic replacement through three-dimensional morphological and chemical mapping", *Nano Lett*., **14**, 6 (2014) pp. 3220–3226.

[10] G. Möbus, R. Doole, B. Inkson, "Spectroscopic electron tomography", *Ultramicroscopy* **96**, 3–4 (2003) pp. 433–451.

[11] Z. Saghi, X. Xu, Y. Peng, B. Inkson and G. Möbus, "Three-dimensional chemical analysis of tungsten probes by energy dispersive x-ray nanotomography", *Appl. Phys. Lett*., **91** (2007) p. 25.

[12] L. Strueder, P. Lechner and P. Leutenegger, "Silicon drift detector—the key to new experiments", Naturwissenschaften **85** 11 (1998) pp. 539–543.

[13] I. Ohnishi, K. Miyatake, Y. Jimbo, Y. Iwasawa, M. Morita, T. Sasaki, H. Sawada and E. Okunishi, "Ultrahighly Efficient X-Ray Detection System of Two Very Large Sized SDDs for Aberration Corrected 300 kV Microscope", Proceedings of Microscopy & Microanalysis 2016, **22** S3 (2016) pp. 318-319.

[14] C. S. M. Yeoh, D. Rossouw, Z. Saghi, P. Burdet, R. K. Leary and P. A. Midgley, "The dark side of EDX tomography-modeling detector shadowing to aid 3d chemical signal analysis", *Microsc. Microanal*., **21**, 3 (2015) pp. 759–764.

[15] Pierre Burdet, Z. Saghi, A. N. Filippin, A. Borrás and P. A. Midgley, "A novel 3D absorption correction method for quantitative EDX-STEM tomography", *Ultramicroscopy* **160** (2016) pp. 118–129.

[16] A. Yasuhara, "Development of Ion Slicer (Thin-Film Specimen Preparation Equipment)", *JEOL News* **40** (2005) pp. 46-49.

Comparison of 3D Imaging Methods in Electron Microscopy for Biomaterials

Tomohiro Haruta   Application Management Department, JEOL Ltd.
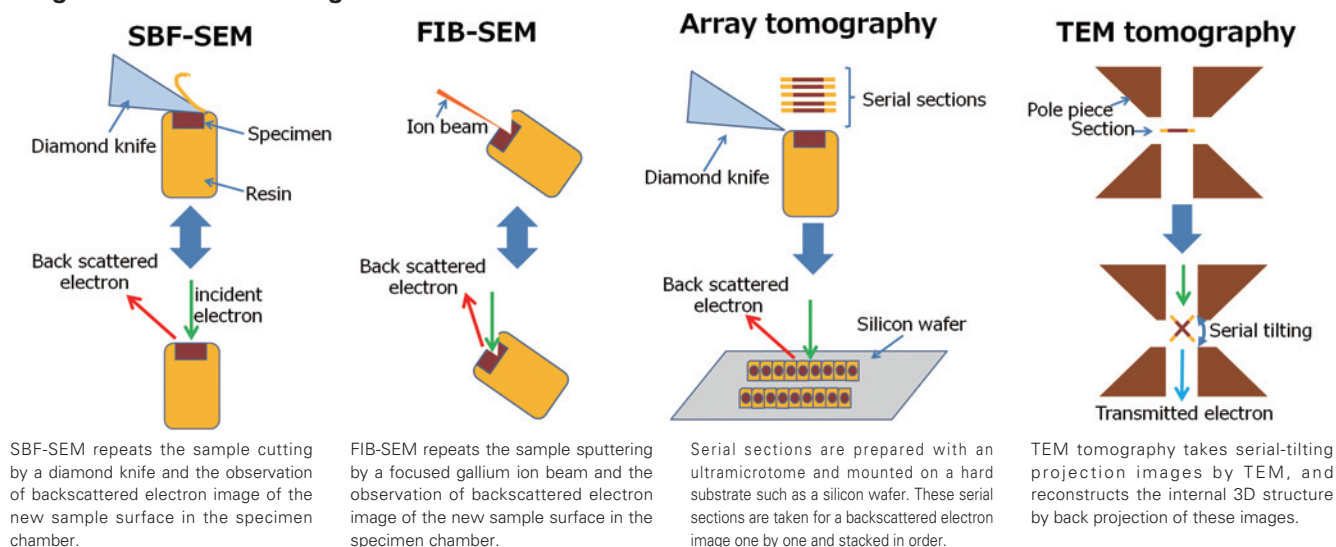
TEM tomography has been widely used for three-dimensional (3D) analysis of fine structures. Recently, new 3D structure analysis methods with SEM, FIB-SEM, Serial Block-Face SEM (SBF-SEM), and Array tomography, are focused by many researchers due to performance improvements of computers and SEM. These methods are suitable for biological samples because their observable area is very wide compared with TEM tomography. Each method has its own advantages and disadvantages, however, there is little example of comparison among these methods using the same sample. In this study, we reconstructed 3D structure of the same sample (*E.coli* and phages) by FIB-SEM, SBF-SEM method, Array tomography and TEM tomography, and investigated advantages and disadvantages of these methods.

Introduction

It is important to know the 3D structure and localization of organelle and protein complex that are components of cells to understand the functions of cells and tissues. This information plays important roles not only in academic research but also in development of therapy for lethal diseases. Previously, TEM tomography has been used for 3D structure observation of these nano-structures. In TEM tomography, we take micrographs of serial tilting images, and reconstruct the 3D image by back-projection of obtained image series. TEM tomography provides high resolution 3D images, and also has a thickness limitation defined by transmission of the electron beam. Therefore, it is difficult to observe the 3D image of whole cell or tissues by TEM tomography. Recent histology or cell biology is strongly connected with molecular biology, and thus it is important to reveal the influence of the morphology and distribution of nano-structures on tissues and whole cell. For that reason, new microscopic methods have been developed, which enable us to observe a large area where the whole cell or tissues is recognized, and can maintain high-resolution while recognizing organelle and protein complexes. In this study, we focus on three kinds of new 3D observation methods, FIB-SEM, SBF-SEM, and Array tomography [1, 2, 3] (**Fig. 1**).

Fig. 1 Schematic diagram of 3D reconstruction methods.

SBF-SEM repeats the sample cutting by a diamond knife and the observation of backscattered electron image of the new sample surface in the specimen chamber.

FIB-SEM repeats the sample sputtering by a focused gallium ion beam and the observation of backscattered electron image of the new sample surface in the specimen chamber.

Serial sections are prepared with an ultramicrotome and mounted on a hard substrate such as a silicon wafer. These serial sections are taken for a backscattered electron image one by one and stacked in order.

TEM tomography takes serial-tilting projection images by TEM, and reconstructs the internal 3D structure by back projection of these images.

〉〉 3-1-2 Musashino, Akishima, Tokyo, 196-8558, Japan | E-mail: tharuta@jeol.co.jp

FIB-SEM is a SEM equipped with a Focused ion beam (FIB) column. A sample in the specimen chamber is sputtered by FIB, and the sputtered surface can be observed by SEM. FIB is not popular in biology but is popular in materials science. This is because specimens in materials science (metals, ceramics, etc.) are too hard to slice by a diamond knife, but can be made into a thin section or exposed new surface by sputtering with FIB. To observe the 3D structure with the FIB-SEM, we sputter the surface of the specimen, and observe the new exposed surface by backscattered electron imaging with SEM, and repeat the process of sputtering and observation. Finally, we can reconstruct the 3D structure by stacking the images of serial section series [1]. The advantages of FIB-SEM are high-precision determination of sputtering sites and preparation of thin sections from hard samples like bones and metals. On the other hand, the disadvantages are narrow observation area and slow sputtering speed.

In the SBF-SEM, we use a SEM that has a mechanism for cutting samples with a diamond knife in its specimen chamber. To reconstruct the 3D image, the surface of the sample is sliced by the diamond knife in the specimen chamber, and a new exposed surface is observed by the SEM. 3D images are reconstructed by stacking the images of serial section series like the FIB-SEM [2]. Advantages of SBF-SEM are high cutting speed and wide cutting area, since samples are cut by the diamond knife. On the other hand, there is a disadvantage that SBF-SEM needs special sample preparation (ex. NCMIR method) because samples are required to be prepared with high electron conductivity and strong heavy metal staining [3]. The preservative quality of nano-structures by this special sample preparation is poorer than the conventional preparation for TEM. Although the conductivity of the sample is increased by the special sample preparation, occasionally the sample may become charged.

In Array tomography, first we prepare the specimen of ultra-thin section ribbon by an ultramicrotome, and serial sections are mounted on the conductive wafer like a silicon wafer. These serial sections are observed piece by piece with a SEM, and 3D images are reconstructed to stack the images in order [4]. Advantages of this method are as follows; Suppression of charging of samples that are very thin and mounted on the conductive wafer, Low initial cost because this method needs only a conventional SEM and an ultramicrotome, and we can use good samples prepared by the conventional preparation techniques for TEM. A disadvantage of this method is that a lot of manual efforts are required, for example, preparation of serial section series.

There is little discussion to compare the features and specifications of these three methods, because the principle of these 3D reconstruction methods with SEM is almost the same. That is, the three methods enable us to make serial sections and observe new sections. In this study, we observed 3D structures of the same sample by these methods, and compared the results. Finally, we discuss and summarize the features of these methods and which sample and analysis are suitable. Furthermore, we attempted analysis of some sample using the suitable methods.

Materials and Methods

We used *E.coli* infected by T4 phage, λ phage, and ϕ 174 phage as samples. Phages are a kind of virus infecting bacteria. The size is 200 nm or less, and it is impossible to observe their morphology without using an electron microscopy (**Fig. 2** a-c).

Phages inject their genome such as DNA or RNA into *E.coli* when phages attach to *E.coli*. The infected phages take over the transcription system, the translation system, and the replication system of host cells, and proliferate itself in host cells. In this stage, we can observe proliferating phages in *E.coli* (Fig. 2 d-f). When phages proliferate sufficiently in the host, phages burst and go out from the host cell. New proliferated phages attach and infect the new host cell.

First, we piled up the soft LB agar containing *E.coli* on hard LB agar. Phages were infected with *E.coli* by dropping the phage containing solution onto this agar. We were able to recognize the area where the phages were infected with *E.coli*, as a plaque after incubation of this agar, and obtained the phage infected *E.coli* by taking out these plaques.

For TEM tomography and Array tomography, samples were prefixed by 2.5% glutaraldehyde in 0.1 M sodium cacodylate (pH 7.2), and postfixed 1% OsO_4 in 0.1 M sodium cacodylate (pH 7.2). Fixed samples were embedded in epoxy resin. The samples were sliced by an ultramicrotome into thin sections which were mounted on silicon wafers for Array tomography. These thin sections were stained by uranium acetate and lead citrate.

For FIB-SEM and SBF-SEM, we applied the NCMIR method for strong heavy metal stain [3]. FIB-SEM can also use samples that are prepared by the conventional method, and in this study we applied the NCMIR method to obtain the strong contrast image. After fixation and staining, the samples were embedded in epoxy resin. Observation conditions are shown in **Table 1**.

Serial section images obtained by FIB-SEM, SBF-SEM and Array tomography were aligned by Fiji [5], and 3D images were reconstructed by stacker (System In Frontier Inc. Japan). In TEM tomography, TEMography was used for acquisition of serial tilting images and 3D reconstructions. Obtained 3D images were segmented and analyzed by Colorist (System In Frontier Inc. Japan).

Results and Discussions

Comparison of 3D reconstruction method using electron microscopy

We observed 2D images using FIB-SEM, SBF-SEM

Fig. 2 TEM images of phages.
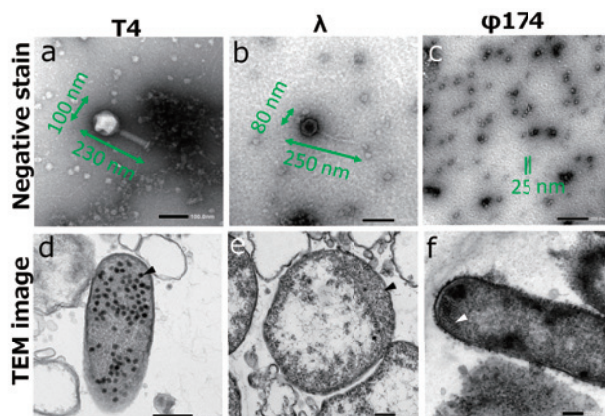
Negative stained images of phage (a-c) and proliferating in *E.coli* (d-f, arrow heads).

(backscattered electron images of the surface of bulk sample, accelerating voltages were 1.0 kV and 3.0 kV, respectively), Array tomography (backscattered electron images of thin section sample mounted on silicon wafer, accelerating voltage was 7.0 kV), and TEM tomography (projection image of thin section sample, no tilting, accelerating voltage was 120 kV). FIB-SEM and SBF-SEM for observation of the surface of bulk sample were inferior to Array tomography and TEM tomography for observation of thin section in the sharpness of images (**Fig. 3**). This is because, in this sample, most observation area was occupied only with low conductivity resin and we had to observe with low accelerating voltage to suppress the charging. The image quality of Array tomography is equal to that of TEM tomography. This result suggested that improvement of sample conductivity and observation at high accelerating voltage are important factors for observing biological samples in 3D structural observation with SEM (Fig. 3 c). In addition, the image quality of FIB-SEM and SBF-SEM is low compared with the other two methods, but they kept the resolution to recognize phage particles.

Next, we compare results of 3D reconstruction. In TEM tomography, the thickness of the slice (200 nm) is smaller than the diameter of *E.coli* (about 2 μm), so that the whole image of one *E.coli* cannot be reconstructed into 3D (**Fig. 4** d). On the other hand, SBF-SEM and FIB-SEM succeeded in 3D observation of a large volume (Fig. 4 a, b). In Array tomography, the observation area of the XY plane is comparable to those of SBF-method and FIB-SEM. However, the thickness of observation volume was reduced because the prepared slices are only 20 in this study (Fig. 4 c). Although mature skills and long acquisition time were required, we consider that it is possible to increase the thickness of 3D reconstruction image by preparing mass serial sections and increasing the number of micrographs taken. In results of extracting one *E.coli* and segmentation of phages contained in the *E.coli* and the extracellular membrane of *E.coli*, we could recognize the morphology of the *E.coli* and 3D distribution of phages using any method, although there are differences in spatial resolution (Fig. 4 e-h). Focusing on the one phage particle, the shape of phage is extended in the Z direction in SBF-SEM and Array tomography, since the resolution along the Z is insufficient against the size of phages (Fig. 4 i, k). In FIB-SEM, although a phage was reconstructed as a ball shape, however, details of the 3D reconstruction image are lost compared to the result of TEM tomography (Fig. 4 j, l). Considering the result of the comparisons, it was found that the quantitative analysis of

---

Table 1 Observation conditions of 3D observation methods.

	SBF-SEM	FIB-SEM	Array tomography	TEM tomography
Instrument	JSM-7800F with Gatan 3View 2XP	JIB-4610F	JSM-7800F	JEM-1400Plus
Acquisition area (X,Y)	24×24 μm²	18×24 μm²	19×24 μm²	3.5×3.5 μm²
Acquisition depth (Z)	7.5 μm (50 nm×150 image)	10.8 μm (20 nm×543 image)	1.4 μm (70 nm×20 image)	200 nm
Pixel size (X,Y)	3 nm	9.4 nm	4.7 nm	1.72 nm
Pixel size (Z)	50 nm	20 nm	70 nm	1.72 nm
Numbers of pixels	8192×8192	1920×2560	3840×5120	2048×2048
Accelerating voltage	1.0 kV	3.0 kV	7.0 kV	120 kV
Acquisition time	2.5 hour	48 hour	4 hour	1 hour

Fig. 3 Comparison of observation area and image quality of each method.
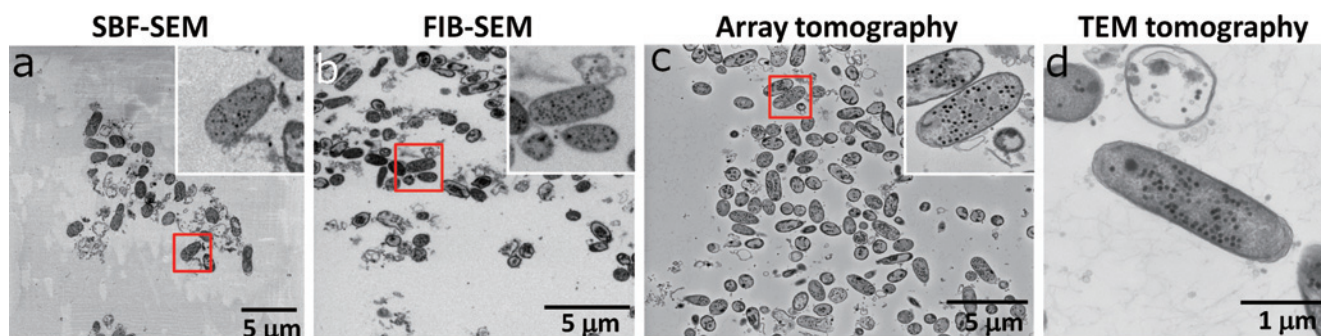
In SBF-SEM, the specimen is easily charged, deteriorating the image quality, because block resin that is little conductive occupies a wide observation area (a). FIB-SEM also enables to observe the wide block resin area, but gallium ions that sputtered the sample surface suppress the charging (b). In Array tomography, we were able to observe high signal-to-noise (SN) ratio images, because the charging was suppressed for the sliced thin sections mounted on a silicon wafer that is highly conductive (c). In TEM tomography, we observed only one *E.coli* (d).

morphology of *E.coli* and the analysis of distribution of phages in *E.coli* can be performed by any 3D reconstruction method with SEM, meanwhile, TEM tomography provides high spatial resolution necessary for observing the nano-structure such as phages. Very similar results were obtained with SBF-SEM and FIB-SEM, which have the common basis of slicing and observing bulk samples in their specimen chambers. Almost the same volumes were obtained by SBF-SEM and FIB-SEM in this study, and the acquisition time of SBF-SEM (2.5 hours) is about 20 times as fast as that obtained by FIB-SEM (48 hours) (Table 1). However, FIB-SEM provided the reconstructed 3D structure image with higher Z resolution than SBF-SEM. The difference of this resolution is due to the difference of cutting thickness: 20 nm for FIB-SEM and 50 nm for SBF-SEM.

These results were summarized in **Table 2**. The image quality of SBF-SEM was inferior to that of other methods, however the wide range of observation area and the speed of observation were unrivaled with SBF-SEM. Furthermore, in samples with high conductivity, the image quality would be improved because the accelerating voltage can be raised more. For the above features, SBF-SEM is suitable for very large samples with high conductivity and for comprehensive analysis. For example, tissue samples are large, the resin area is small, and conductivity is high. Comprehensive analysis is required in connectome analysis.

FIB-SEM needs long acquisition time compared with SBF-SEM, however, it is advantageous for FIB-SEM that Z resolution is very high. This advantage is only valid for a narrow observation area. FIB-SEM is suitable for small samples, for example, small tissues or one whole cell. FIB-SEM has high affinity for quantitative analysis, since high quantitativeness needs the high resolution. In addition, it is possible to cut bones and metals, enabling 3D analysis of hard tissues and contact portion between metals and tissues.

Fig. 4 Comparison of 3D reconstruction results.
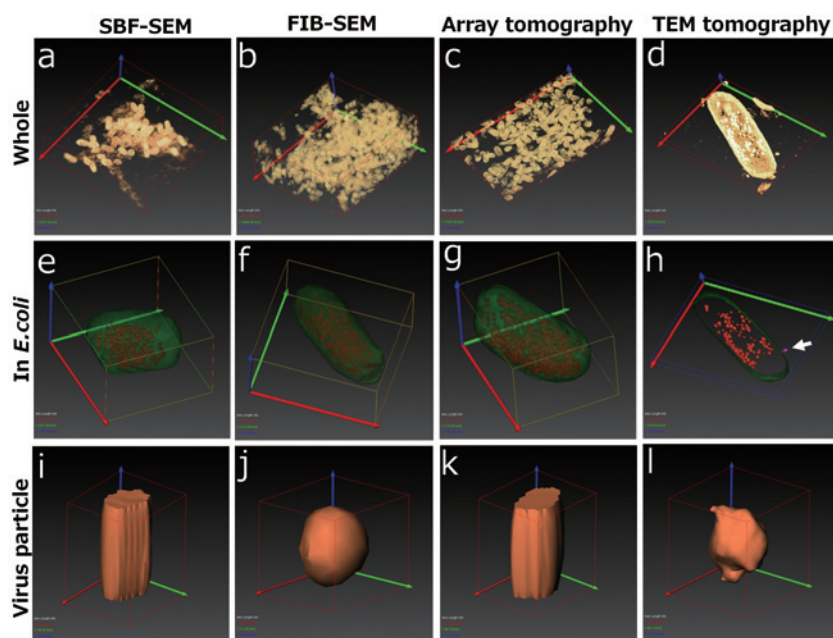
We reconstructed the 3D structure of *E.coli* infected with T4 phages. Volume rendering images of the whole observation area (a-d). Segmentation images of one *E.coli* cell that is infected with T4 phages (green), T4 phages that is grown in *E.coli* (orange), and infected (pink) (e-h). Segmentation images of one T4 phages in *E.coli* (i-l).

Table 2 Summary of the features of 3D structural analysis by electron microscopy.

	SBF-SEM	FIB-SEM	Array tomography	TEM tomography
field of view(X,Y)	1 0 0 μm over	1〜1 0 0 μm	1 0 0 μm over	5 μm less
Depth of field of view(Z)	Very deep	Deep	Narrow	Verry narrow
3D resolution(Z)	5 0 nm	2 0 nm	7 0 nm	1 nm
Acquisition time	Some decade ours	Some days	Some days	1〜2 hours
effort to acquisition	Little	Little	Enormous	Little
Optimal samples	Tissues, Brain	Tissues, Cultured cell	Tissues, Embryo, Cultured cell	Organelle, Virus
Optimal application	Conectome、Exhaustive analysis	Morphological observation, Quantitative analysis	Quantitative analysis, CLEM	Morphological observation

In Array tomography, samples remain after the observation; meanwhile, matured techniques that make serial sections and long acquisition time were required to deepen the observable depth. Array tomography is suitable for detailed analysis of rare phenomena in a large observation area. We expected that the transparent substrate such as glass allows for various correlative methods, including correlative light and electron microscopy (CLEM). Array tomography is effective for observation of floating cells, bacteria and embryos which have low conductivity, surrounded by resin around samples, since the samples are thin sections on a conductive substrate, charging are suppressed and the samples can be observed with high accelerating voltage.

Analysis of 3D reconstruction image

(1) The relationship of morphology of *E.coli* that is infected by T4 phages and internal phage particle

SBF-SEM was enough to analyze the morphology of *E.coli* and distribution of T4 phage. We analyzed the relationship of the morphology of *E.coli* and internal phages by using the result of SBF-SEM. First we examined the relationship between the volume of *E.coli* and the number of phages (**Fig. 5** a). The results show that the maximum number of internal phage in an *E.coli* is about 280 particles, and no *E.coli* containing more phage particles could be observed. We considered that as the number of phage particles increases further, this increase causes *E.coli* to burst. The number of contained phage particles tends to increase, as the volume of *E.coli* increases. However, this relationship is not linear; there was a difference in the number of phage particles even in the same volume *E.coli* (B and C, D, E in Fig. 5 a). Therefore, we selected characteristic *E.coli* (A-E in Fig. 5 a, c). Selected *E.coli* cells are as follows. The ones were small volume and they have few phage particles (A, B in Fig. 5 a, c). Next ones were also small volume, but they had many phage particles (C-E in Fig. 5 a, c). Another ones were large volume and they had a lot of phage particles (F in Fig. 5 a, c). *E.coli*

cells were divided into three parts in the long axis direction, center part, middle part, and side part. We analyzed which part of the T4 phage particles was localized (Fig. 5 b). Most of phage particles localized at the center part, when phage particles were few. The phage particles localized in the center part were dispersed from the middle part to side part, as the internal phage particles increase. Furthermore, as the volume of *E.coli* increased, phage particles in the center part decreased more, and phage particles localized in the side part increased. Next, we focused on the shape of *E.coli*. The shape of *E.coli* that had few T4 phage particles was rod like shape (Fig. 5 c B). When internal T4 phage particles were increased, *E.coli* expanded to the short axis direction, and the shape became barrel like shape (Fig. 5 c C-E).

(2) The relationship between type of phage and distribution of phage in *E.coli*

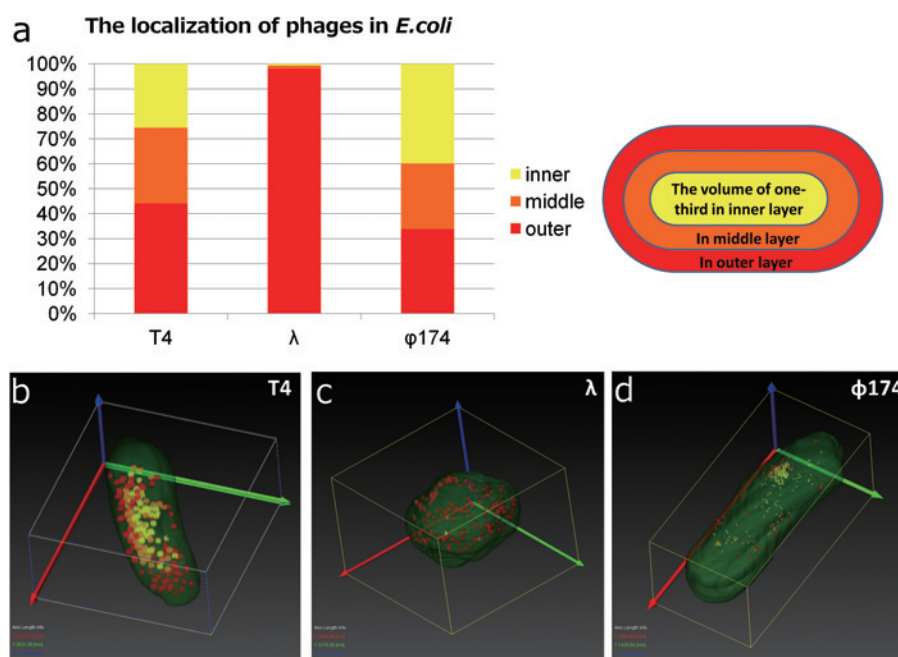T4 phage could be recognized by any 3D structure analysis with SEM since it has strong contrast in *E.coli*. However, λ phage and ϕ174 phage were difficult to recognize in *E.coli* because they had low contrast in *E.coli*, and ϕ174 phage was too small (Fig. 2 e, c, f). Therefore, the comparison of the *E.coli* infected by T4 phage, λ phage and ϕ174 phage was done using 3D reconstruction images by Array tomography. First we focused on the morphology of the *E.coli*. The shape of the *E.coli* infected by λ phage changed from a rod-like structure to a ball-like structure. We separated *E.coli* infected phages into three layers; inner layer, middle layer, and outer layer, and investigated which phages are localized in which layer (**Fig. 6** a). The result show that T4 phage and ϕ174 phage dispersed in *E.coli* without bias, however, almost λ phage particle localized at the outer layer. T4 phage and ϕ174 phage are lytic phage. As soon as they are infected with *E.coli*, they begin to proliferate in host cells and host cells burst (lyse). On the other hand, λ phage is a temperate phage. When they are infected with *E.coli* and inject their genome into host cells,

---

Fig. 5 Relationship of morphology of *E.coli* and involved phages.
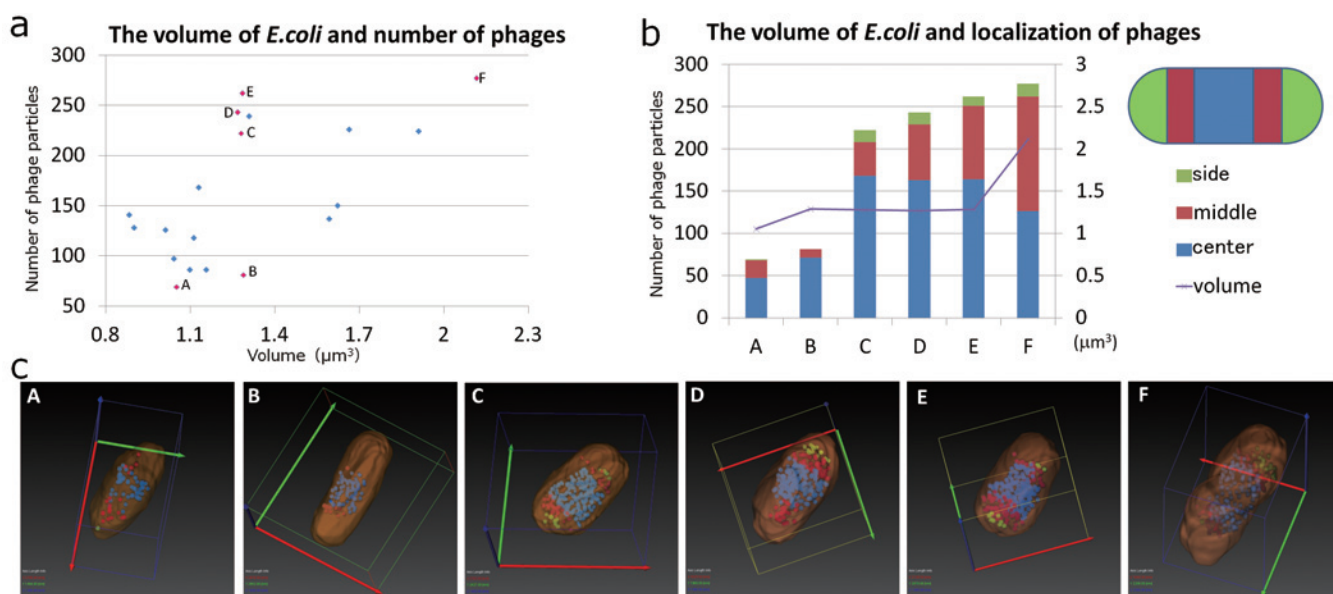
The left graph shows the relationship of the volume of *E.coli* infected with T4 phage and the number of involved T4 phages (a). We selected six characteristic *E.coli* cells (pink dot in the left graph, A-F). The morphology of these 6 *E.coli* cells that involved T4 phages were visualized by segmentation (c), the right graph shows the relationship of the volume of *E.coli* and the distribution of T4 phage (b).

Fig. 6 3D distribution of phages in *E.coli*.

a The localization of phages in *E.coli*

inner
middle
outer

The volume of one-third in inner layer
In middle layer
In outer layer

b T4   c λ   d φ174

We compared distributions of phages from the results of 3D structure reconstruction of T4 phage, λ phage, and φ174 phage form Array tomography. We separated *E.coli* into three parts; the inner area, middle area and outer area, and counted the number of phages involved in each part. T4 phages and φ174 phages have little bias of distribution, however almost λ phages localized at the outer area (a). *E.coli* that infected with λ phage changed their shapes from rod to globular (c).

they do not lyse immediately. After infection, they insert their genome into the genome of host and behave as part of the host (lysogenization). However, the repressor which suppresses the proliferation of the phage is inactivated by the change of environment, phage start to proliferate and the host lyse. The difference in observed morphological change and localization of phages may originate from proliferation area, lytic phages proliferate in infected area immediately and the temperate phages proliferate on the host genome. ϕ 174 phages did not show the biased distribution in the three layers, but they localized in specific part (Fig. 6 d). In this experiment, we could not identify the first infected place, but the localized place may be related to the first infected place.

Conclusion

Each 3D reconstruction method with SEM has its own strength and weakness depending on the sample preparation and acquisition conditions such as accelerating voltage. In SBF-SEM and FIB-SEM, data acquisition is performed automatically, on the other hand, after segmentation analysis is often performed manually. Segmentation that extracts tissues and regions of interest is often performed based on image contrast. However, biological samples have small differences in contrast, and sometimes the contrast alone may not determine the segmentation. It is possible to segment with the morphology as a landmark by keeping high resolution of the image, and thus it helps improve segmentation efficiency. SBF-SEM and FIB-SEM need to introduce the dedicated instruments, while Array tomography can be started with conventional SEM and ultramicrotome, but some skills are required. The choice of which method to use is an important strategy in promoting research efficiently. We hope this paper is helpful for researchers who are planning to start the 3D analysis with electron microscopy.

References

[1] Knott G, Marchman H, Wall D, Lich B. Serial section scanning electron microscopy of adult brain tissue using focused ion beam milling. *J Neurosci*. (2008).

[2] Micheva KD, Smith SJ. Array tomography: a new tool for imaging the molecular architecture and ultrastructure of neural circuits. *Neuron*. (2007).

[3] Deerinck, T. J. & Bushong, Eric & Thor, A & Ellisman, Mark. NCMIR methods for 3D EM: A new protocol for preparation of biological specimens for serial block face scanning electron microscopy. *Nat Center Microsc Imag Res*. 6-8. (2010).

[4] Denk W, Horstmann H. Serial block-face scanning electron microscopy to reconstruct three-dimensional tissue nanostructure. *PLoS Biol*. (2004).

[5] Schindelin J, Arganda-Carreras I, Frise E, Kaynig V, Longair M, Pietzsch T, Preibisch S, Rueden C, Saalfeld S, Schmid B, Tinevez JY, White DJ, Hartenstein V, Eliceiri K, Tomancak P, Cardona A. Fiji: an open-source platform for biological-image analysis. *Nat Methods*. (2012).

Biomarker Analysis in Petroleum Samples Using GC×GC-HRTOFMS with an Ion Source Combining Electron Ionization (EI) and Photo Ionization (PI)

Masaaki Ubukata and Yoshihisa Ueda   MS Business Unit, JEOL Ltd.

Two kinds of petroleum samples were analyzed by "JMS-T200GC AccuTOF™ GCx-plus", the latest model of JEOL GC-TOFMS (gas chromatograph time-of-flight mass spectrometer) that has high mass resolution and high-speed mass spectra acquisition capabilities combined with the photoionization source and the GC×GC system. Several kinds of biomarkers such as 18-Norabiotane, Cholestane, Hopane, Adamantane, Iceane and Diamantane could be separated and selectively detected by GC×GC and photoionization.

Introduction

As a result of recent advancement in gas chromatography (hereinafter referred to as "GC") technologies, especially for capillary column technologies, a variety of capillary columns have been developed with different separation capabilities. Furthermore, comprehensive two-dimensional GC (hereinafter referred to as "GC×GC") has been developed using these capillary column capabilities to separate chemical substances that have very complex compositions [1, 2]. GC×GC systems consist of two types of capillary columns with different separation modes connected in series. Additionally, there is a cryo-trap system (thermal modulator) placed between the first and second columns to modulate the sample injection into the second column. This two-column system allows GC×GC to use two different separation modes in a single analysis. The components are separated in the first column, cryo-trapped for 5-10 seconds, and then rapidly released by the thermal modulator into the second column which has a narrow inner diameter and short length. This process means that the eluted components from the first column are trapped and released at intervals of 5 to 10 seconds and then are continuously and rapidly separated in the second column. As a result, the two-dimensional chromatogram contains two retention time axes, one for the primary column and one for the secondary column.

In general, quadrupole mass spectrometers (hereinafter referred to as "QMS") are widely used for GC-MS measurements. However, these systems are generally not suitable as a GC×GC detector. As described previously, the second column of the GC×GC system has a unique geometry (narrow diameter and short length) that separates the components very rapidly. This feature results in chromatographically narrow peak widths that require high data-acquisition speeds in order to acquire enough data points across each analyte peak. If a QMS is used, then there are limited data points measured for the second-dimension peaks in the chromatogram, thus resulting in poor quality 2D chromatographic data. Therefore, it is not optimal to use a QMS system as the detector for GC×GC.

To overcome this problem, JEOL developed a gas chromatograph time-of-flight mass spectrometer (hereinafter referred to as GC-TOFMS) with both high mass resolution (R=10,000) and high-speed mass spectral data acquisition (up to 50 Hz) that is optimal for combining with GC×GC. This combination GC×GC-TOFMS system was first introduced in 2004 and is widely used for the analysis of various complex samples [3-7]. In this report, we use our 4th generation GC-TOFMS model "JMS-T200GC AccuTOF™ GCx" with an optional photoionization source and GC×GC system to analyze biomarkers in petroleum samples.

GC×GC-PI-TOFMS System

GC×GC system

A Zoex Corporation ZX2 GC×GC thermal modulator system was used with our GC-TOFMS system. The schematic diagrams of GC×GC thermal modulator was shown in **Fig. 1**. This modulator unit was placed between the two capillary columns in order to cryo-trap the components eluting from the first column using the "cold jet gas" and in order to release them using the "hot jet gas". Since the "hot jet gas" is sprayed for very short period (300-400 msec) with regular interval (5-10 seconds), released

〉〉 3-1-2 Musashino, Akishima, Tokyo, 196-8558, Japan | E-mail: yaida@jeol.co.jp

components are introduced into the second column each interval regularly, as a result the two-dimensional chromatographic separation is achieved as shown in **Fig. 2**.

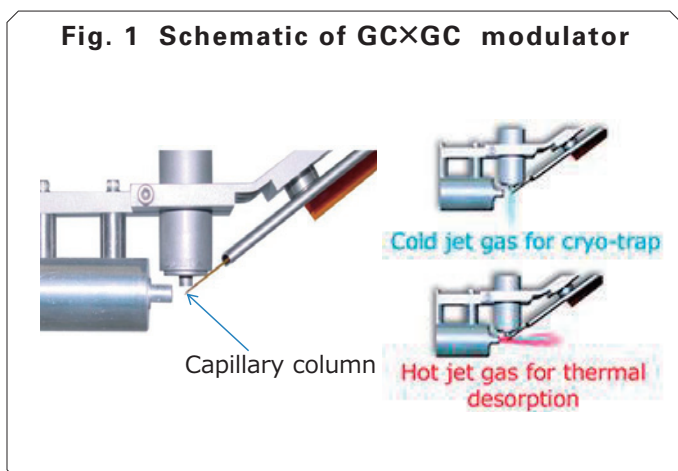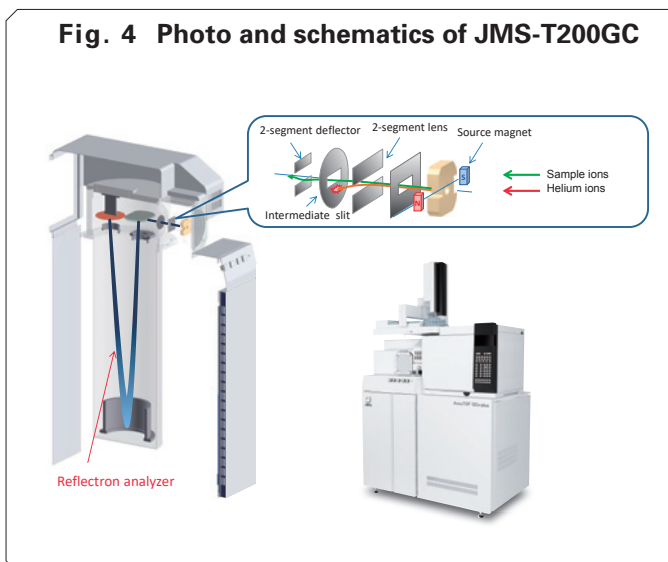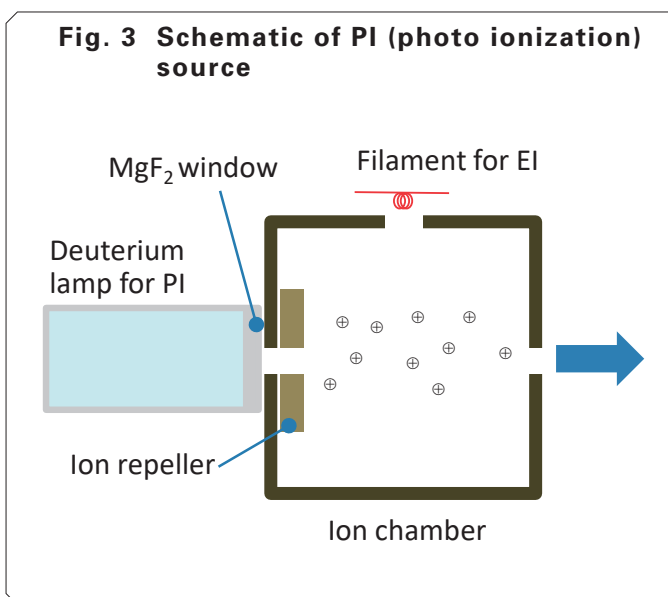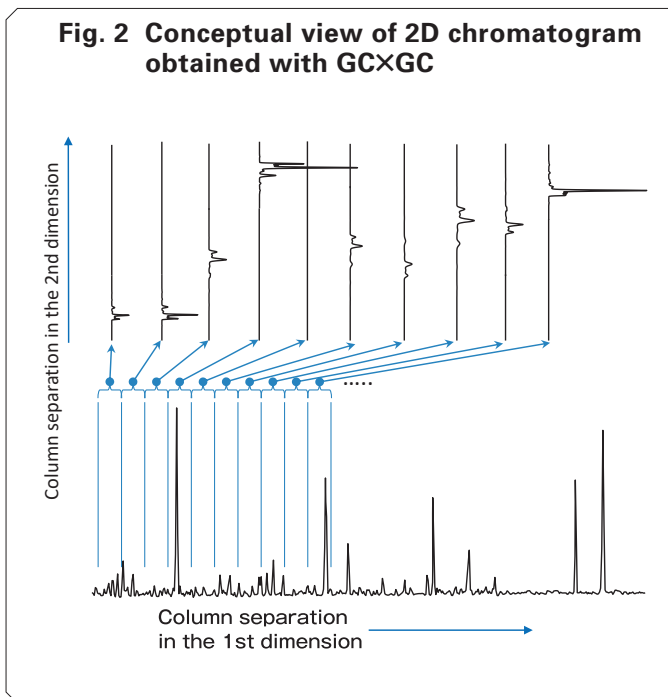## Photoionization Source (PI)

The most commonly used ionization method for GC-MS is Electron Ionization (EI). EI is a hard ionization technique that uses high energy electrons to ionize the analytes, resulting in many fragment ions. These mass spectra can be very useful for chemical structural analysis of target compounds and can be compared to MS search libraries such as the NIST database to help confirm the identity of target compounds. However, the EI spectra can often have low intensity molecular ions, which can make it difficult to estimate the elemental composition from the measured exact mass. As a result, this technique is not always an ideal ionization method for these purposes. Alternatively, soft ionization techniques that use low energy methods to ionize the sample analytes can be used to generate higher intensity molecular ions. In the GC-MS analysis field, Chemical Ionization (CI) is the most common soft ionization method available. JEOL offers not only CI but also Field Ionization (FI) and Photoionization (PI) as optional soft ionization methods for the JMS-T200GC.

The PI photon source is a deuterium lamp with radiation wavelengths from 115 to 400 nm. The energy for the smallest wavelength (115 nm) is 10.8 eV which is a good match for the primary ionization energy for typical organic compounds (~10 eV). As a result, this source is suitable for the soft ionization of these types of analytes.

The PI source schematic is shown in **Fig. 3**. The JEOL PI source is incorporated into the standard EI source, which allows for the unique capability of switching between EI and PI without breaking vacuum. All that is necessary for EI measurements is to turn on the EI filament, and then for PI measurements, simply turn off the EI filament and turn on the deuterium lamp.

High resolution TOFMS system

A photo of the external view of JEOL AccuTOF™ GCx along with the schematics for the ion source, ion transfer system and ion optical system are shown in **Fig. 4**. The compounds eluting from the GC column are first ionized in the ion source and then transferred into the TOF analyzer using a low kinetic energy of approximately 30 eV. Afterwards, the ions are measured by using a single-stage reflectron TOF analyzer that orthogonally accelerates the ions away from the ion-transfer direction. This type of TOFMS is called an

Fig. 1 Schematic of GC×GC modulator

Capillary column

Cold jet gas for cryo-trap

Hot jet gas for thermal desorption

Fig. 2 Conceptual view of 2D chromatogram obtained with GC×GC

Column separation in the 2nd dimension

Column separation in the 1st dimension

Fig. 3 Schematic of PI (photo ionization) source

MgF$_2$ window

Filament for EI

Deuterium lamp for PI

Ion repeller

Ion chamber

Fig. 4 Photo and schematics of JMS-T200GC

2-segment deflector   2-segment lens   Source magnet

Sample ions
Helium ions

Intermediate slit

Reflectron analyzer

"Orthogonal-Acceleration Time-of-Flight Mass Spectrometer" (oa-TOFMS).

It is worth noting that there are some challenges for using TOF instruments as GC-MS detectors. In particular, helium gas is used as the GC carrier gas which means that the volume of this gas is relatively large compared to the target compounds present in the sample injections. For EI, helium is also ionized and transferred together with the sample ions into the analyzer, thus resulting in a large number of helium ions in the ion beam. These ions can produce large space charging effects (charging, etc.) within the analyzer that can degrade the resolution of the instrument. Additionally, for TOFMS analyzers, these helium ions will reach the detector, resulting in the rapid deterioration of the microchannel plate (MCP). To overcome this problem, the JEOL GC-TOFMS system is innovatively designed so that the ion transfer system removes 99.9% or more of the helium ions produced in the ion source by adjusting the lens balance voltages.

Biomarker Analysis of Petroleum Samples Using GC×GC-PI-TOFMS

Biomarkers contained within crude oils and their source rocks are often investigated to index petroleum samples and to determine petroleum sample origins. Biomarkers are organic compounds that originated from the living organisms that were present in the source material of the oil. These biomarker molecules, which are indicators of the origin organic substances, sedimentary environments, maturity, etc.,

can be used to determine the origins of an unknown crude oil. However, petroleum samples are comprised from an aggregate of hundreds or even thousands of hydrocarbons. Further complicating the situation, biomarkers are hydrocarbons with specific structures found within these complex petroleum samples. As a result, comprehensively detecting biomarkers within petroleum samples is very difficult to accomplish.

In this report, we will use the high separation capabilities of GC×GC in combination with the combo EI/PI source and high mass resolution TOFMS to comprehensively detect the biomarkers within petroleum samples.

Measurement conditions

The measurement conditions are listed in **Table 1**. A ZX2 thermal modulation system (Zoex Corporation) was used for the GC×GC measurements. A nonpolar BPX5 column (SGE Corporation, 30 m length, 0.25 mm I. D., 0.25 μm liquid phase thickness) was used for the first column. A more polar BPX50 column (SGE Corporation, 3 m length, 0.1 mm I. D., 0.1 μm liquid phase thickness) was used for the second column. Two test samples (Petroleum Fractions A and B) were prepared for these tests, and the biomarker amounts were estimated and compared for each fraction.
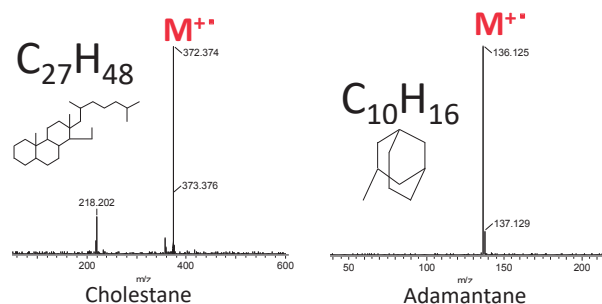
Measurement results

The PI mass spectra for Cholestane and Adamantane, both of which are typical biomarkers, are shown in **Fig. 5**. The molecular ions M+· were detected as the base peak for each of these compounds, thus confirming that PI is effective for

---

Table 1 Measurement conditions

Instrument	JEOL AccuTOF™ GC series
	Zoex ZX2 thermal modulator
1st Column	BPX5, 30 m × 0.25 mm, 0.25 μm
2nd Column	BPX50, 3 m × 0.1 mm, 0.1 μm
Modulator period	6 sec
Inlet pressure	350 kPa (Out flow : 1.75 mL/min)
Inlet mode	Cool on column, Oven track mode, 1 μL Injection
Oven Temp.	50 ℃ (2 min) → 10 ℃/min → 250 ℃
Ion Source	EI/PI Combination Ion Source
Ionization mode	PI+ (D₂ lamp, 115 to 400 nm)
m/z range	m/z 35 to 700
Spectrum recording speed	25 spectra / sec

Fig. 5 PI mass spectra of Cholestane and Adamantane

$C_{27}H_{48}$ — M+· 372.374, 373.376, 218.202 — Cholestane

$C_{10}H_{16}$ — M+· 136.125, 137.129 — Adamantane

Fig. 6 2D TIC of Petroleum fraction A, measured by GC×GC/PI

C_nH_{2n-8}
C_nH_{2n-6}
C_nH_{2n-4}
Retention time of 2nd Column
n-Alkanes and Cycloalkanes
Retention time of 1st Column

Fig. 7 2D TIC of Petroleum fraction B, measured by GC×GC/PI

C_nH_{2n-8}
C_nH_{2n-6}
C_nH_{2n-4}
Retention time of 2nd Column
n-Alkanes and Cycloalkanes
Retention time of 1st Column
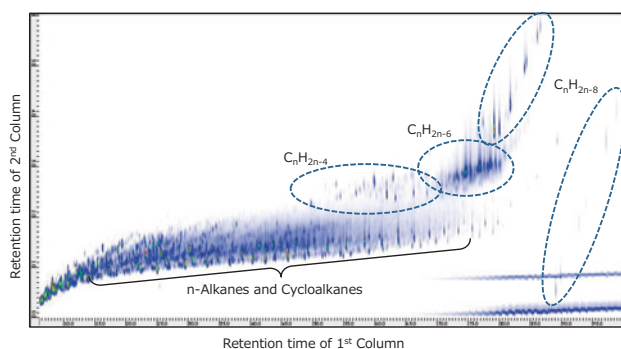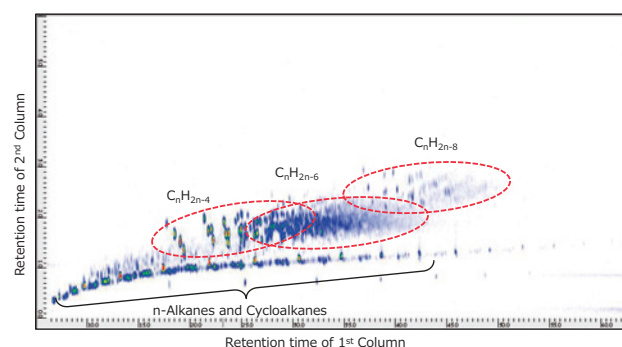
detecting these biomarker molecular ions.

The 2D TICCs (total ion current chromatograms) for the GC×GC/PI measurements are shown in **Fig. 6** and **Fig. 7** for each crude oil sample. Both samples contained n-Alkanes (C_nH_{2n+2}) and Cycloalkanes (C_nH_{2n+1}) along with numerous chemical compounds detected at later secondary column retention times. These compounds were identified as C_nH_{2n-4}, C_nH_{2n-6} and C_nH_{2n-8} which have higher degrees of unsaturation than n-Alkanes and Cycloalkanes. Additionally, these two petroleum fraction samples were measured by GC×GC/EI under the same conditions. Based on the library search results

for the EI mass spectra corresponding to C_nH_{2n-4}, C_nH_{2n-6} and C_nH_{2n-8}, Petroleum Fraction A mainly contained the Cholestane polycyclic saturated hydrocarbons while Petroleum Fraction B mainly contained the Adamantene saturated-bridged cyclic hydrocarbons.

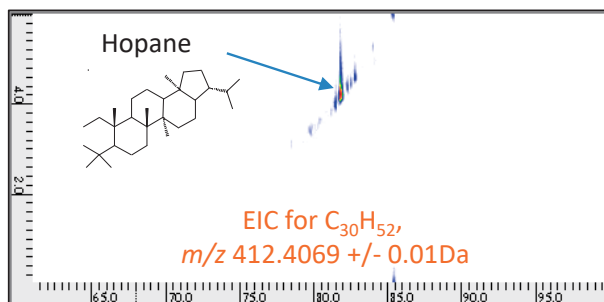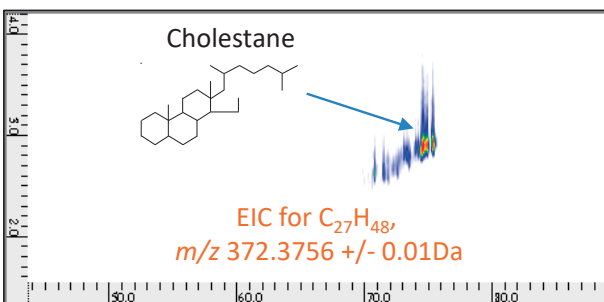Next, high selectivity 2D EICs (Extracted Ion Chromatograms) were constructed for the molecular ions of six chemical compounds that are generally known as biomarkers (**Table 2**). As shown in **Fig. 8** and **Fig. 9**, 18-Norabietane, Cholestane and Hopane were specifically identified in Petroleum Fraction A, and Adamantane, Iceane and Diamantane were identified in

Table 2 Typical biomarkers and "*m/z*" of their molecular ions

Compounds	Rational Formula	*m/z*
18-Norabietane	$C_{19}H_{34}$	262.2661
Cholestane	$C_{27}H_{48}$	372.3756
Hopane	$C_{30}H_{52}$	412.4069
Adamantane	$C_{10}H_{16}$	136.1252
Iceane	$C_{12}H_{18}$	162.1409
Diamantane	$C_{14}H_{20}$	188.1565

Fig. 8 2D EIC of Petroleum fraction A, measured by GC×GC/PI

Isomers of 18-Norabietane

EIC for $C_{19}H_{34}$, *m/z* 262.2661 +/- 0.01Da

Cholestane

EIC for $C_{27}H_{48}$, *m/z* 372.3756 +/- 0.01Da

Hopane

EIC for $C_{30}H_{52}$, *m/z* 412.4069 +/- 0.01Da
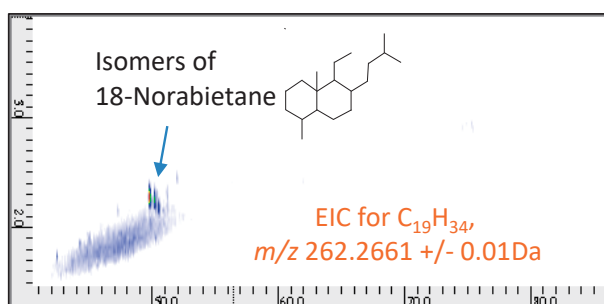
(*m/z* 262.2661, 372.3756, 412.4069)

Fig. 9 2D EIC of Petroleum fraction B, measured by GC×GC/PI

Adamantane

EIC for $C_{10}H_{16}$, *m/z* 136.1252 +/- 0.01Da

Iceane

EIC for $C_{12}H_{18}$, *m/z* 162.1409 +/- 0.01Da

Diamantane

EIC for $C_{14}H_{20}$, *m/z* 188.1565 +/- 0.01Da
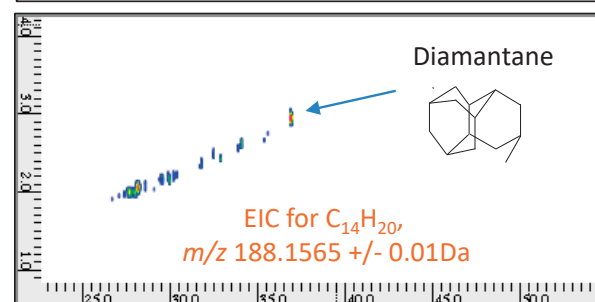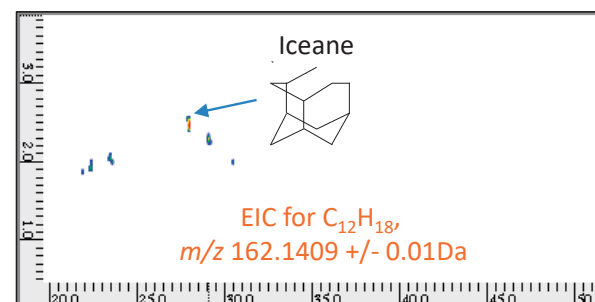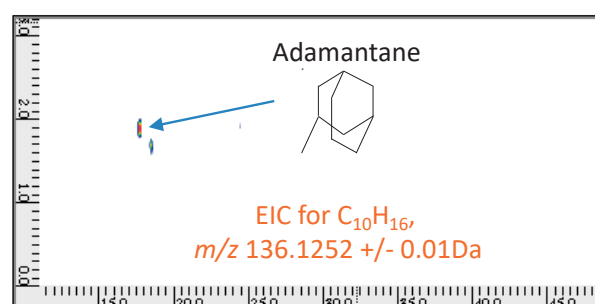
(*m/z* 136.1252, 162.1409, 188.1565)

Fig. 10 Total 2D EIC of Petroleum fraction A, measured by GC×GC/PI

Summed EIC for C_nH_{2n-4} series (n=19-31),
Exact mass of the molecular ions +/- 0.01Da

Androstane

Summed EIC for C_nH_{2n-6} series (n=19-30),
Exact mass of the molecular ions +/- 0.01Da

Summed EIC for C_nH_{2n-8} series (n=27-35),
Exact mass of the molecular ions +/- 0.01Da
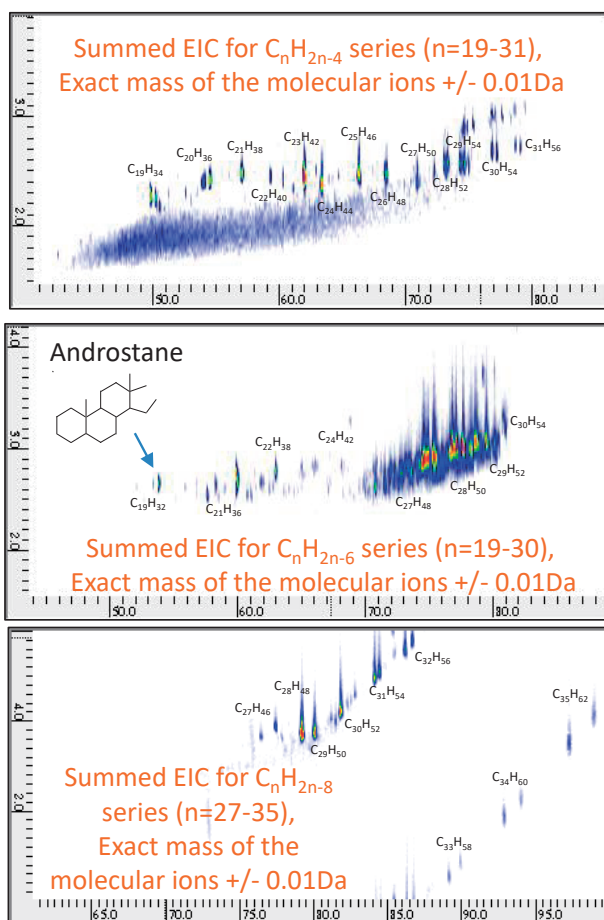
(C_nH_{2n-4} : n=19〜31, C_nH_{2n-6} : n=19〜31, C_nH_{2n-8} : n=27〜35)

Fig. 11 Total 2D EIC of Petroleum fraction B, measured by GC×GC/PI

Summed EIC for C_nH_{2n-4} series (n=10-18),
Exact mass of the molecular ions +/- 0.01Da

Summed EIC for C_nH_{2n-6} series (n=12-19),
Exact mass of the molecular ions +/- 0.01Da

Summed EIC for C_nH_{2n-8} series (n=14-20),
Exact mass of the molecular ions +/- 0.01Da
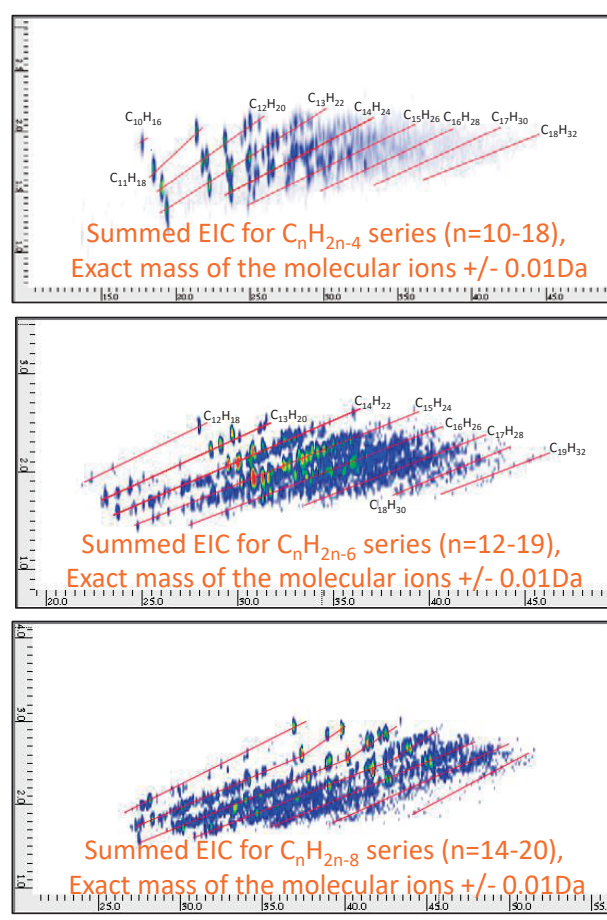
(C_nH_{2n-4} : n=10〜18, C_nH_{2n-6} : n=12〜19, C_nH_{2n-8} : n=14〜20)

Petroleum Fraction B. Next, the related compounds for these biomarkers were systematically evaluated by creating summed 2D EICs for the C_nH_{2n-4}, C_nH_{2n-6} and C_nH_{2n-8} series. The 2D EICs for these series are shown in **Fig. 10** and **Fig. 11**.

These results clearly showed that the biomarkers and their related compounds are present within each petroleum fraction. Since the PI method selectively produces molecular ions for these analytes, a systematic evaluation for the biomarker amounts was achieved by combining the high separation capabilities of GC×GC with the soft ionization of PI and high resolution TOFMS. Additionally, the 2D EICs for the PI measurements made it much easier to interpret the data and correctly assign the biomarker identities in the crude oil samples.

Summary

GC×GC is an advanced GC technology that offers dramatically higher chromatographic separation capabilities than that of conventional 1D GC. To maximize the quality of data obtained with this high-separation capability, it is effective to use a TOFMS that offers both high speed data acquisition and high mass resolution in combination with hard ionization and soft ionization methods. The JEOL GC×GC-TOFMS system equipped with the combination EI/PI source accomplishes all of this in a single package.

As reported in this application note, our latest GC×GC-TOFMS in combination with the optional EI/PI source is a very powerful tool for the analysis of complex mixtures like biomarkers in petroleum samples.

References

[1] Z. Liu, J. B. Phillips, *J. Chromatogr. Sci*., **29** 227 (1991).
[2] J. C. Giddings, *Anal. Chem*., **56** 1258A (1984).
[3] GERSTEL K. K. Japan, N. Ochiai, "Ultra micro-volume analysis of environmental contaminants using GC×GC-TOFMS", JEOL MS Users Meeting (2008) (in Japanese).
[4] S. Hashimoto, Y. Takazawa, A. Fushimi, H. Ito, K.Tanabe, Y. shibata, M. Ubukata, A. Kusai, K. Tanaka, H. Otsuka, K. Anezaki, *J. Chromatogr. A*., **1178** 187 (2008).
[5] Kyushu Environmental Evaluation Association, M. Ueda, "Qualitative and quantitative analyses of organic compounds in fuel oil using GC×GC-HRTOFMS", JEOL MS Users Meeting (2010) (in Japanese).
[6] *Nihondenshi News* **Vol. 44** (2017) p40 to 49 (in Japanese).
[7] Anupam Giri, et al., *Anal. Chem*., **89** (10) (2017) p5395 to 5403.

Development of the JBX-8100FS Electron Beam Lithography System

Yukinori Aida   SE Business Unit, JEOL Ltd.

An Electron Beam Lithography system (hereafter EBL) is a product that can reproduce data designed by a user onto a silicon substrate or photomask blank. The shape of the electron beam will vary according to the application. A spot type electron beam (hereafter SB) is described in this report. The SB is an electron beam with a circular diameter of several nm, so it is possible to process patterns of less than 10 nm in size. With high-precision stage positioning technology incorporating a laser measurement system, it is possible to correct the position of the electron beam to compensate for errors in the stage stopping position. Conventionally, the application for SB with these features was mainly the research and development of next-generation semiconductor devices. Recently, however, the worldwide demand for SB has been growing as they are being used in production for a wide variety of communication devices and sensors. Applications can range from the production of sensors used for collision-prevention systems for automobiles to Distributed Feedback (DFB) lasers, which are used in the communication hubs for 4th generation communication systems (4G). To meet this demand, a new product, the JBX-8100FS, has been developed. This report introduces the JBX-8100FS series.

Introduction

The user creates pattern data using CAD, etc. This data can be replicated onto a substrate material by the EBL system, making it possible to perform nanofabrication. Since one of the goals in the manufacture of semiconductor devices is to make products smaller, the makers of the equipment used to manufacture semiconductors must develop equipment that can provide smaller pattern size. There is also a need to control the pitch with high accuracy of 0.1 nm or less for the production of DFB lasers, for example. This means that highly-accurate positioning is required. For research on nanoimprint template production, in addition to the accuracy described above, it is also necessary to achieve high positioning accuracy within the substrate. Furthermore, for the fabrication of transistors used in millimeter-wave devices, patterns must be overlaid onto pre-fabricated materials with high accuracy. As this illustrates, the accuracy demands differ according to the type of device being produced. The JBX-8100FS (**Fig. 1**) was developed to satisfy these various needs.

The specifications of JBX-8100FS (**Table 1**) include a maximum accelerating voltage of 100 kV, maximum scan speed of 125 MHz, writable area of 150 mm × 150 mm, and a laser measurement resolution of 0.6 nm. The performance specifications for High throughput mode and High resolution mode are shown; this system can handle a wide range of needs, from manufacturing to R&D. The performance in High throughput mode includes maximum field size of 1000 μm, minimum beam diameter of 5.1 nm, data increment of 0.5 nm,

field stitching accuracy of ± 20 nm or less, overlay accuracy of ± 20 nm or less, minimum line width of 12 nm or less, current drift of 0.2%p-p/h or less, and beam position drift of 60 nm p-p/h or less. In comparison, in High resolution mode, the performance includes maximum field size of 100 μm, minimum beam diameter of 1.8 nm, data increment of 0.05 nm, field stitching accuracy of ± 9 nm or less, overlay accuracy of ± 9 nm or less, minimum line width of 8 nm or less, current drift of 0.2%p-p/h or less, and beam position drift of 10 nmp-p/h or

Fig. 1 Exterior view of JBX-8100FS

All units are contained within the panels, except the power supplies, cooling water circulator, and dry pump.

〉〉 3-1-2 Musashino, Akishima, Tokyo, 196-8558, Japan | E-mail: yaida@jeol.co.jp

less. In addition, since the power consumption during normal operation is 3 kVA, this is also an attractive instrument in terms of running costs.

Performance Test Results

The performance of the JBX-8100FS with regard to minimum line width, field stitching accuracy, overlay accuracy and field in-plane dimensional accuracy was measured.

Minimum Line Width

To evaluate the lithography performance of the JBX-8100FS, a 50 nm thickness of ZEP520A resist (ZEON Corp.) was applied to a silicon substrate, and writing was performed under conditions of 100 pA beam current and a minimum beam diameter of 1.8 nm. A minimum line width of 8 nm or less is guaranteed. Special development was used this time to obtain an even finer structure. Low temperature development is generally known as a method for obtaining enhanced structures [1]. ZEP520A resist was developed at a temperature of 2.8ºC, which allowed data demonstrating a minimum line width of 4.2 nm to be obtained (**Fig. 2**).

Field Stitching Accuracy

The JBX-8100FS utilizes a stage position correction system called Laser Beam Control (hereafter LBC), providing highly accurate position correction. Furthermore, with the addition of JEOL's exclusive material distortion correction and deflection distortion correction, the accuracy is guaranteed. To measure the field stitching accuracy, an optical coordinate measurement system was used. "L" marks were placed at the corners of each processing field, and a 4 × 4 layout of fields was processed. The coordinates of the L-shaped marks at the points of intersection between the fields were measured, and the position accuracy was evaluated. The results for a 1000 µm area are reported here. The specifications guarantee an accuracy of within ± 20 nm or less. The actual results obtained were +11.5 nm / -9.8 nm (**Fig. 3**(a)). Even Vernier patterns with a resolution of 8 nm placed at the field corners were visually confirmed, and similar performance results were obtained (Fig. 3(b)).

Overlay Accuracy

One feature of the SB is the ability to directly write a pattern onto a substrate which already has another pattern written

---

Table 1 Main specifications of JBX-8100FS (entry model)

Items	JBX-8100FS(G1) Entry model
Acceleration voltage	100 kV
Field size	1,000 µm × 1,000 µm (HT), 100 µm × 100 µm (HR) (HT; High Throughput Mode / HR: High Resolution mode)
Minimum data increment	0.5 nm (HT), 0.05 nm (HR)
Scan speed	125 MHz
Scan speed modulation	256 rank / resolution 0.05 nsec ~
Positioning DAC / Scanning DAC	20 bit / 14 bit
Beam diameter	5.1 nm (HT), 1.8 nm (HR)
Minimum line width	<12 nm (HT), <8 nm (HR)
Field stitching accuracy	≦ ± 20 nm (HT), ≦ ± 9 nm (HR)
Overlay accuracy	≦ ± 20 nm (HT), ≦ ± 9 nm (HR)
Beam current stability	0.2%p-p /h (@2 nA, HT)
Beam position stability	≦ 60 nmp-p/h (@2 nA/HT), ≦ 10 nm/hp-p (@2 nA/HR)
Operating system	Linux, ('Data preparation program' can work on Windows 8.1 and 10)
Writing area	150 mm × 150 mm
Substrate size	Full 6 inch wafer, 8 inch wafer loadable, small piece, 6 inch Mask
Maximum stage speed	25 mm/sec
Laser measurement resolution	0.6 nm
Electric requirements	3 kVA (Main console 2 kVA, cwc 1 kVA, Normal)

Other options include a 12 cassettes auto loading system and switchable acceleration voltage (50 kV/25 kV).

Fig. 2 Cross section image of a minimum width line (×200 k)
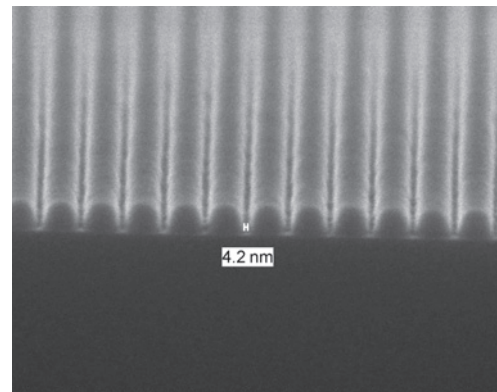
4.2 nm

With ZEP520A (by ZEON) at thickness 40 nm, using the low-temperature effect, a line width of 4.2 nm can be achieved.

Fig. 3 Field stitching accuracy measurement results
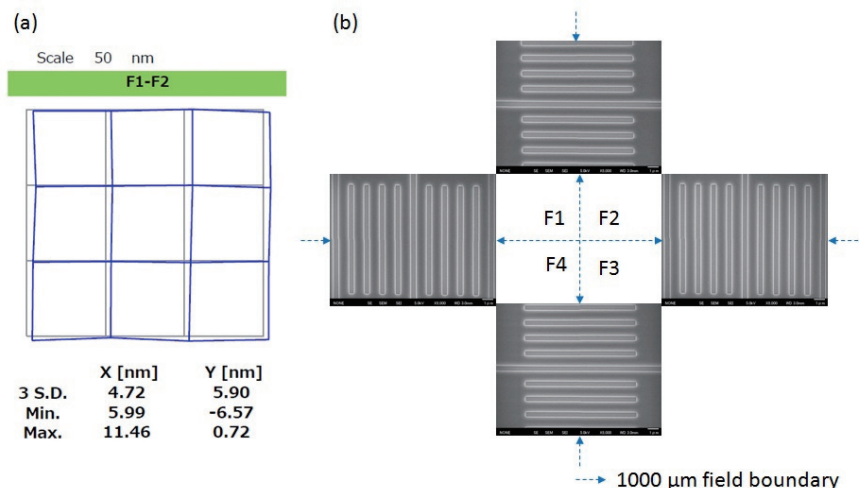
(a)

Scale 50 nm

F1-F2

(b)

F1 F2
F4 F3

1000 µm field boundary

	X [nm]	Y [nm]
3 S.D.	4.72	5.90
Min.	5.99	-6.57
Max.	11.46	0.72

(a) The measurement area was defined by a 4 × 4 array of points at 10 mm intervals (defining a 30 mm × 30 mm area), and the field stitching accuracy was measured. The guaranteed value is ± 20 nm or less, but the actual results obtained were +11.5 nm / -9.8 nm (X/Y).

(b) In the same way, the results of SEM observation of Vernier patterns with a resolution of 8 nm were obtained, and similar values were observed.

on it. The EBL systems are equipped with a mark-detection function whereby alignment marks created on the material being processed can be detected and the coordinates determined. If the position of the pattern being drawn is recorded relative to the coordinates of the alignment marks, the deviation can be calculated and corrected when writing is performed. To evaluate this performance, EBL was used to process both the first and second layers. The writing area was 30 mm × 30 mm (4 × 4 points at 10 mm intervals.) The measurement was made by superimposing a 3 mm × 3 mm area (4 × 4 points at 1 mm intervals.) at one location within the 30 mm × 30 mm writing area, and the overlay accuracy was measured. The guaranteed performance is ± 20 nm or less, and the actual results obtained were +4.1 nm / -6.7 nm (**Fig. 4**(a)). Similarly, the results of measurements of Vernier patterns with a resolution of 8 nm showed that the superimposition was nearly perfectly centered in both the X and Y directions (Fig. 4(b)).

CD (Critical Dimension) uniformity within field

The drawing of a grating, like that required for DFB lasers, was performed and the accuracy of the line widths was determined. A line-and-space pattern was placed at the center and each corner of a 1000 μm field. Writing with a line width of 100 nm and 200 nm pitch was performed. The results show and accuracy of 1.1%p-p, with a maximum of 100.6 nm and a minimum of 99.5 nm (**Fig. 5**).

Stability

The stability is an important performance factor for EBL, which basically runs 24 hours per day. It is also possible to equip this system with a JEOL dedicated air conditioning unit and JEOL EMI countering unit, making it possible to achieve even better stability. The results of measurements in 100 kV High throughput mode using a current of 2 nA indicated a current drift of 0.08%p-p/h, and a beam position drift in the X direction of 9.5 nmp-p/h, and 10.8 nmp-p/h in the Y direction (**Fig.6**).

Throughput

Since the beam profile is small with the SB, there is a tendency for the processing times to become longer in comparison to the variable type EBL. As mentioned above, since these are being used for manufacturing in recent years, the focus of device development has been on improving the throughput. The factors that determine the throughput of a lithography system include the stage movement time, stage settling time after movement, the correction time, data transfer time, the electrical system settling time, and the beam exposure time. The improvements in these factors achieved with the JBX-8100FS are described below.

① Stage movement time
This depends on the maximum speed of stage movement, but for short distances, the acceleration is also quite important. This has been improved by 10% to 20% through the optimization of the various parameters.

② Data transfer time
This is the time needed for figure data transfer before writing. This has been improved to be 1/3 to 1/5 the time needed by conventional systems.

③ Sub Deflector Amplifier settling time
This is the time needed from data transfer until writing

starts. Compared to the transfer time, this is now short enough to be ignored.

④ Beam exposure time
The beam irradiation time for a single spot with the spot beam, given by the following equation.

$$t = \frac{Q \times p^2}{I}$$

t: Beam irradiation time [sec], Q: Resist sensitivity [C/cm^2], p: Shot pitch [cm], I: Beam current [A]

With the JBX-8100FS, the minimum value for t is 8 nsec (125 MHz when expressed as a frequency). Compared to conventional systems, scanning is possible at more than double the speed.

As a result of the improvements described above, a 30% to 40% improvement in the total writing time is possible for a pattern with a writing area covering about 10% of the total substrate surface.

Power Consumption

After a system is purchased, an important on-going factor becomes the running costs. Particularly for EBL systems, in order to obtain stable function, it is necessary to continuously supply the same electrical power, even when lithography is not being performed. The electrical units and power sections of the JBX-8100FS have been compactly designed, reducing the power consumption to 3 kVA during normal operation. This allows the system to be operated using only about 1/3 the power required by the conventional systems.

Summary

The R&D and production of semiconductor devices covers a broad range of applications, and the functions and precision required vary. The JBX-8100FS has been developed as an electron beam lithography system that can be used with high precision and high speed in any field, while also reducing power consumption. Future plans include further improvement of the throughput and improved substrate handling methods.

Acknowledgements
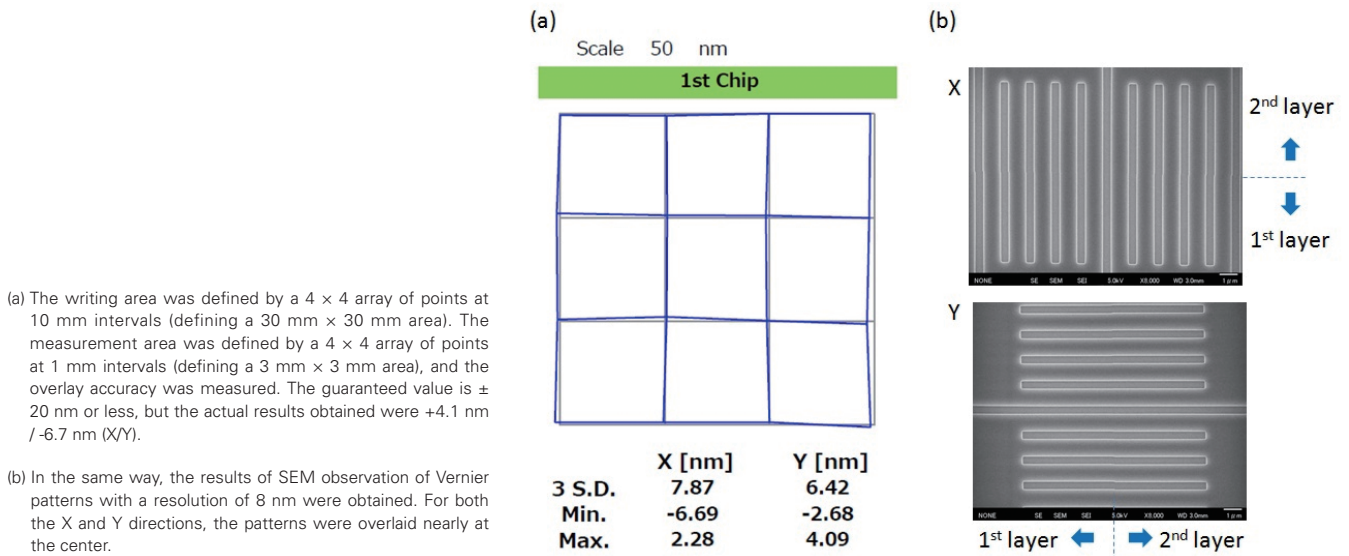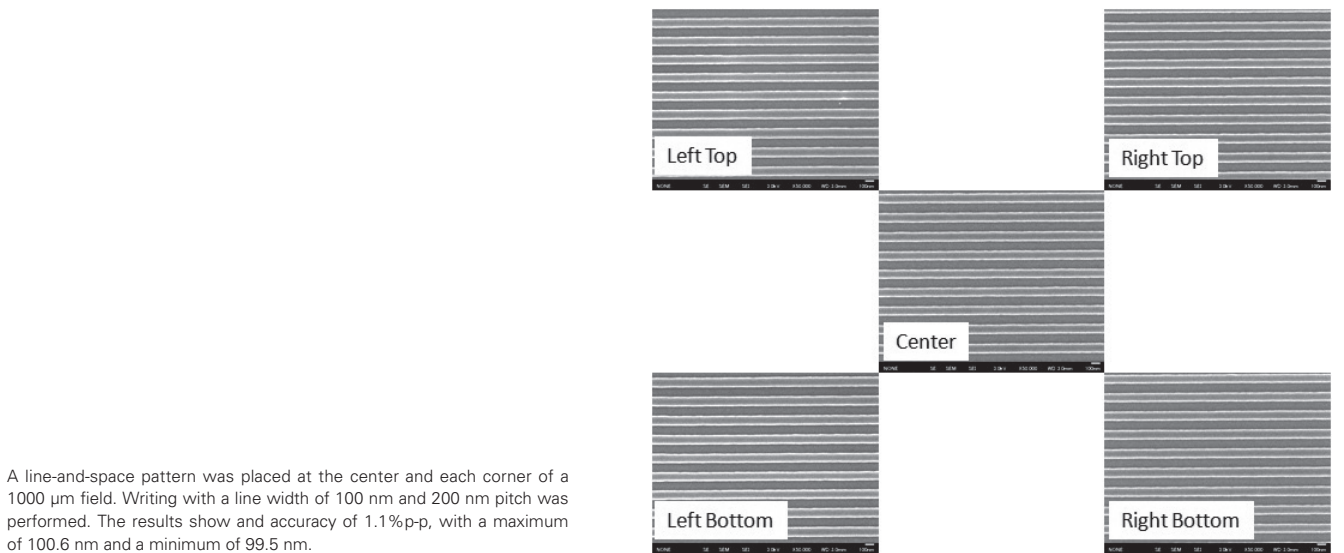
References

[1] T. Okada, J. Fujimori, M. Aida, M. Fujimura, T. Yoshizawa, M. Katsumura, and T. Iida: "Enhanced resolution and groove-width simulation in cold development of ZEP520A" *J. Vac. Sci. Technol.* **B 29** (2011) 021604.
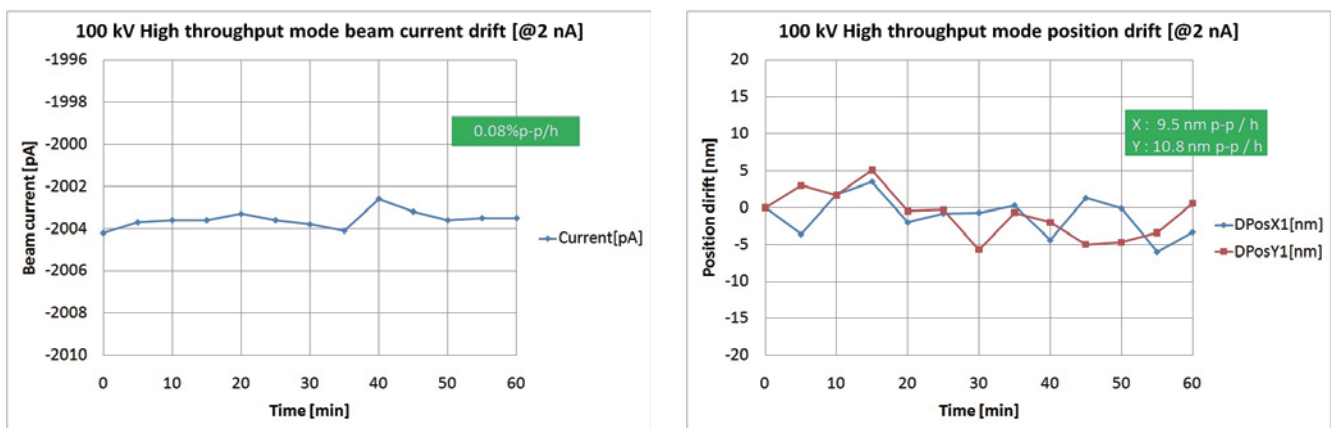
Fig. 4 Overlay accuracy measurement values

(a)

Scale   50   nm

1st Chip

(b)

X

2nd layer

↑
↓

1st layer

Y

1st layer ⬅ ➡ 2nd layer

(a) The writing area was defined by a 4 × 4 array of points at 10 mm intervals (defining a 30 mm × 30 mm area). The measurement area was defined by a 4 × 4 array of points at 1 mm intervals (defining a 3 mm × 3 mm area), and the overlay accuracy was measured. The guaranteed value is ± 20 nm or less, but the actual results obtained were +4.1 nm / -6.7 nm (X/Y).

(b) In the same way, the results of SEM observation of Vernier patterns with a resolution of 8 nm were obtained. For both the X and Y directions, the patterns were overlaid nearly at the center.

	X [nm]	Y [nm]
3 S.D.	7.87	6.42
Min.	-6.69	-2.68
Max.	2.28	4.09

Fig. 5 Critical dimension uniformity within field

Left Top

Right Top

Center

Left Bottom

Right Bottom

A line-and-space pattern was placed at the center and each corner of a 1000 µm field. Writing with a line width of 100 nm and 200 nm pitch was performed. The results show and accuracy of 1.1%p-p, with a maximum of 100.6 nm and a minimum of 99.5 nm.

Fig. 6 Stability

100 kV High throughput mode beam current drift [@2 nA]

0.08%p-p/h

Beam current [pA] vs Time [min]

—•—Current[pA]

100 kV High throughput mode position drift [@2 nA]

X : 9.5 nm p-p / h
Y : 10.8 nm p-p / h

Position drift [nm] vs Time [min]

—•—DPosX1[nm]
—■—DPosY1[nm]

The stability was measured over a 1 hour period in 100 kV high throughput mode. Using a current of 2 nA, the current drift was 0.08%p-p/h, and the position drift in the X direction was 9.5 nmp-p/h, and 10.8 nmp-p/h in the Y direction.

JEOL Ltd.   3-1-2 Musashino Akishima Tokyo 196-8558 Japan   Sales Division Tel. +81-3-6262-3560   Fax. +81-3-6262-3577

www.jeol.com   ISO 9001 · ISO 14001 Certified

ARGENTINA
COASIN S.A.C.I.yF.
Virrey del Pino 4071,
C1430CAM-Buenos Aires
Argentina
Tel. 54-11-4552-3185
Fax. 54-11-4555-3321

AUSTRALIA & NEW ZEALAND
JEOL (AUSTRALASIA) Pty.Ltd.
Suite 1, L2 18 Aquatic Drive
- Frenchs Forest NSW 2086
Australia
Tel. 61-2-9451-3855
Fax. 61-2-9451-3822

AUSTRIA
JEOL (GERMANY) GmbH
Gute Aenger 30
85356 Freising, Germany
Tel. 49-8161-9845-0
Fax. 49-8161-9845-100

BANGLADESH
A.Q. CHOWDHURY SCIENCE & SYNERGY PVT. LTD.
87, Suhrwardry Avenue, Floor 2
Baridhara, Dhaka1212
Bangladesh
Tel. 8802-9862272, 8953450, 8953501
Fax. 8802-9854428

BELGIUM
JEOL (EUROPE) B.V.
Planet II, Gebouw B
Leuvensesteenweg 542,
B-1930 Zaventem
Belgium
Tel.32-2-720-0560
Fax.32-2-720-6134

BRAZIL
JEOL Brasil Instrumentos Cientificos Ltda.
Av. Jabaquara, 2958 5° andar conjunto 52 ;
04046-500 Sao Paulo, SP
Brazil
Tel. 55-11-5070 4000
Fax. 55-11-5070 4010

CANADA
JEOL CANADA, INC.
3275 1ere Rue, Local #8
St-Hubert, QC J3Y-8Y6, Canada
Tel. 1-450-676-8776
Fax. 1-450-676-6694

CHILE
ARQUIMED INNOVATION
Arturo Prat 828,
Santiago, Chile
Tel. 56-2-634-6266
Fax. 56-2-634-4633

CHINA
JEOL (BEIJING) CO., LTD.
Zhongkeziyuan Building South Tower 2F,
Zhongguancun Nansanjie Street No. 6,
Haidian District, Beijing, P.R.China
Tel. 86-10-6804-6321
Fax. 86-10-6804-6324

JEOL (BEIJING) CO., LTD., SHANGHAI BRANCH
Rm. 1505-1506, Benben Mansion No. 300, Xikang Road,
Shanghai 200040, China
Tel. 86-21-6248-4487 / 4868
Fax. 86-21-6248-4075

JEOL (BEIJING) CO., LTD., GUANGZHOU BRANCH
N1601, World Trade Center Building,
#371-375, Huan Shi Road East, Guangzhou,
Guangdong Prov., 510095, P.R.China
Tel. 86-20-8778-7848
Fax. 86-20-8778-4268

JEOL (BEIJING) CO., LTD., WUHAN BRANCH
Room A2118, Zhongshang Plaza Office Bldg.,
No. 7 Zhongnan Road, Wuhan,
Hubei, 430071, P.R.China
Tel. 86-27-8713-2567
Fax. 86-27-8713-2567

JEOL LTD. (BEIJING) CO., LTD., CHENGDU BRANCH
1807A Zongfu Building,
NO. 35 Zhongfu Road, Chengdu, Sichuan, 610016
P.R. China
Tel. 86-28-86622554
Fax. 86-28-86622564

EGYPT
JEOL SERVICE BUREAU
3rd Fl. Nile Center Bldg., Nawal Street,
Dokki, (Cairo), Egypt
Tel. 20-2-3335-7220
Fax. 20-2-3338-4186

FRANCE
JEOL (EUROPE) SAS
Espace Claude Monet, 1 Allee de Giverny
78290, Croissy-sur-Seine, France
Tel. 33-13015-3737
Fax. 33-13015-3747

GERMANY
JEOL (GERMANY) GmbH
Gute Aenger 30
85356 Freising, Germany
Tel. 49-8161-9845-0
Fax. 49-8161-9845-100

GREAT BRITAIN & IRELAND
JEOL (U.K.) LTD.
JEOL House, Silver Court, Watchmead,
Welwyn Garden City, Herts AL7 1LT, U.K.
Tel. 44-1707-377117
Fax. 44-1707-373254

GREECE
N. ASTERIADIS S.A.
56-58,S. Trikoupi Str. P.O. Box 26140
GR-10022, Athens, Greece
Tel. 30-1-823-5383
Fax. 30-1-823-9567

HONG KONG
FARMING LTD.
Unit No. 1009, 10/F., Prosperity
663 King's Road, North Point, Hong Kong
Tel. 852-2815-7299
Fax. 852-2581-4635

INDIA
JEOL INDIA Pvt. Ltd.
Unit No. 305, 3rd Floor,
ABW Elegance Tower,
Jasola District Centre,
New Delhi 110 025, India
Tel. 91-11-6472-2578
Fax. 91-11-4060-1235

JEOL India Pvt. Ltd. Mumbai Branch
Regus Mumbai
Levels Ground & 1, Trade Centre Bandra Kurla Complex 1108,
Bandra (E) Mumbai, 400051,India
Tel : +91-22-40700700

INDONESIA
PT. TEKNOLABindo Penta Perkasa
Komplek Gading Bukit Indah Blok I/11
Jl. Bukit Gading Raya Kelapa Gading Permai,
Jakarta 14240, Indonesia
Tel. 62-21-45847057/58
Fax. 62-21-45842729

ITALY
JEOL (ITALIA) S.p.A.
Palazzo Pacinotti - Milano 3 City,
Via Ludovico il Moro, 6/A
20080 Basiglio(MI) Italy
Tel. 39-02-9041431
Fax. 39-02-90414343

KOREA
JEOL KOREA LTD.
Dongwoo Bldg. 7F, 1443, Yangjae Daero,
Gangdong-Gu, Seoul, 05355, Korea
Tel. 82-2-511-5501
Fax. 82-2-511-2635

KUWAIT
Ashraf & CO. Ltd.
P.O.Box 3555 Safat 13036, Kuwait
Tel. 965-1805151
Fax. 965-24335373

MALAYSIA
JEOL (MALAYSIA) SDN.BHD.
508, Block A, Level 5,
Kelana Business Center,
97, Jalan SS 7/2, Kelana Jaya,
47301 Petaling Jaya, Selangor, Malaysia
Tel. 60-3-7492-7722
Fax. 60-3-7492-7723

MEXICO
JEOL DE MEXICO S.A. DE C.V.
Arkansas 11 Piso 2
Colonia Napoles
Delegacion Benito Juarez, C.P. 03810
Mexico D.F., Mexico
Tel. 52-5-55-211-4511
Fax. 52-5-55-211-0720

Middle East
JEOL GULF FZCO
P.O. Box No. 371107
Dubai Airport Free Trade Zone West Wing 5WA No. G12,
Dubai, UAE
Tel. 971-4-609-1497
Fax. 971-4-609-1498

PAKISTAN (Karachi)
ANALYTICAL MEASURING SYSTEM (PVT) LTD. (AMS LTD.)
14-C Main Sehar Commercial Avenue Lane 4,
Khayaban-e-Sehar,
D.H.A-VII, Karachi-75500, Pakistan
Tel. 92-21-35345581/35340747
Fax. 92-21-35345582

PANAMA
PROMED S.A.
Parque Industrial Costa del Este
Urbanizacion Costa del Este
Apartado 0816-01755, Panama, Panama
Tel. 507-303-3100
Fax. 507-303-3115

PORTUGAL
Izasa Portugal Lda.
R. do Proletariado, 1
2790-138 CARNAXIDE, Portugal
Tel. 351-21-424-73-00
Fax. 351-21-418-60-20

QATAR
Mannai Trading Company W.L.L.
ALI Emadi Complex,
Salwa Road P.O.Box 76, Doha, Qatar
Tel. +974 4455-8216
Fax. +974 4455-8214

RUSSIA
JEOL (RUS) LLC
Krasnoproletarskaya Street, 16,
Bld. 2, 127473, Moscow,
Russian Federation
Tel. 7-495-748-7791/7792
Fax. 7-495-748-7793

SAUDI ARABIA
ABDULREHMAN ALGOSAIBI G.T.C.   (Riyadh)
Algosaibi Building-Old Airport Road
P.O. Box 215, Riyadh-11411, Saudi Arabia
Tel. 966-1-477-7932

SCANDINAVIA
SWEDEN
JEOL (Nordic) AB
Hammarbacken 6A, Box 716, 191 27 Sollentuna
Sweden
Tel. 46-8-28-2800
Fax. 46-8-29-1647

SINGAPORE
JEOL ASIA PTE.LTD.
2 Corporation Road
#01-12 Corporation Place
Singapore 618494
Tel. 65-6565-9989
Fax. 65-6565-7552

SOUTH AFRICA
ADI Scientific (Pty) Ltd.
370 Angus Crescent,
Northlands Business Park, 29 Newmarket Road
Northriding, Ranburg, Republic of South Africa
Tel. 27-11-462-1363
Fax. 27-11-462-1466

SPAIN
IZASA Scientific SLU.
Argoneses, 13, 28108 Alcobendas,
Madrid, Spain
Tel. 34 902 20 30 80
Fax. 34 902 20 30 81

SWITZERLAND
JEOL (GERMANY) GmbH
Gute Aenger 30
85356 Freising, Germany
Tel. 49-8165-77346
Fax. 49-8165-77512

TAIWAN
JIE DONG CO., LTD.
7F, 112, Chung Hsiao East Road,
Section 1, Taipei, Taiwan 10023 (R.O.C.)
Tel. 886-2-2395-2978
Fax. 886-2-2322-4655

For NMR & Mass Spectrometer Products
Widetron Technologies Corp.
No.8-2., No.77, Sec.2, Zhonghua E Rd.,
East Dist., Tainan City 701, Taiwan (R.O.C.)
Tel. 886-6-289-1943
Fax. 886-6-289-1743

(For Mass Spectrometer Products)
TechMax Technical Co., Ltd.
5F., No.11, Wuquan 2nd Rd., Wugu Dist.,
New Taipei City 248, Taiwan (R.O.C.)
Tel. 886-2-8990-1779
Fax. 886-2-8990-2559

For Semiconductor Products:
JEOL TAIWAN SEMICONDUCTORS LTD.
2F-2, No. 192, Dongguang Rd.
East Dist., Hsinchu City 30069,
Taiwan (R.O.C.)
Tel. 886-3-571-5656
Fax. 886-3-571-5151

THAILAND
BECTHAI BANGKOK EQUIPMENT & CHEMICAL CO., Ltd.
300 Phaholyothin Rd. Phayathai, Bangkok 10400,
Thailand
Tel. 66-2-615-2929
Fax. 66-2-615-2350/2351

JEOL ASEAN TECHNICAL CENTER (JATC)
MTEC building room 533
114 Moo9, Thailand Science Park
Paholyothin Rd., Klong 1, Klong Luang,
Pathumthani 12120
THAILAND
Tel. 66-2-564-7738
Fax. 66-2-564-7739

THE NETHERLANDS
JEOL (EUROPE) B.V.
Lireweg 4, NL-2153 PH Nieuw-Vennep,
The Netherlands
Tel. 31-252-623500
Fax. 31-252-623501

TURKEY
Tekser A.S.
Kartal Cad. No: 55/3 Inonu Wah.,
Atasehir 34755, Istanbul, Turkey
Tel. 90-216-5736470
Fax. 90-216-5736475

USA
JEOL USA, INC.
11 Dearborn Road, Peabody, MA 01960, U.S.A.
Tel. 1-978-535-5900
Fax. 1-978-536-2205/2206

JEOL USA, INC. WEST OFFICE
5653 Stoneridge Drive Suite #110
Pleasanton, CA 94588, U.S.A.
Tel. 1-925-737-1740
Fax. 1-925-737-1749

VENEZUELA
GOMSA Service and Supply C.A.
Urbanizacion Montalban III
- Residencias Don Andres - Piso 7 - Apartamento 74
Avenida 3, entre calles 7 y 6
Montalban, Caracas, Venezuela
Tel. 58-212-443-4342
Fax. 58-212-443-4342

VIETNAM
TECHNICAL MATERIALS AND RESOURCES
IMPORT-EXPORT JOINT STOCK COMPANY(REXCO)
Hanoi Branch
SALES & SERVICE
155-157 Lang Ha Street, Dong Da District, Hanoi, Vietnam
Tel. +84 (43) 562 0516
Fax. +84 (43) 853 2511